A TUNABLE MICROCAVITY FOR SEMICONDUCTOR QUANTUM DOTS

Russell James Barbour, M.Phys (Hons)

Submitted for the degree of Doctor of Philosophy

Heriot-Watt University

School of Engineering and Physical Sciences

July 2009

Abstract

Semiconductor optical microcavities that combine high Q-factors with a small mode volume play a vital role in modifying the interaction between light and matter. Several interesting phenomena arise when an emitter is introduced into such a cavity. These include enhancement or suppression of the spontaneous emission rate (weak coupling) and normal mode splitting (strong coupling). In order to fully exploit the high Q and low mode volume of current microcavities, it is crucial for the emitter to be resonant with the cavity mode. Furthermore the emitter must be located at the exact antinode of the cavity electric field. Wavelength tuning in semiconductor monolithic microcavities is challenging and is traditionally achieved by altering the temperature or using the Stark shift to alter the emitter's wavelength. Spatially matching the emitter to the electric field antinode in monolithic cavities is even more challenging.

The work in this thesis addresses these challenges. The realisation of a miniaturised, fully tunable Fabry-Pérot type microcavity for semiconductor quantum dot experiments is presented. The cavity has a high Q-factor and low mode volume. The cavity wavelength is tuned by altering the air gap between the mirrors to vary the cavity length. This allows a much broader tuning range than is possible using monolithic cavities. In this work the cavity modes are characterised using a fixed wavelength laser technique and varying the cavity length. A high finesse is obtained by using a miniaturised concave mirror which laterally confines the optical mode.

Unprecedented in situ control over a single InAs/GaAs quantum dot within the cavity mode is demonstrated at 4 K. The Purcell effect is demonstrated for a single quantum dot, spatially positioned at the exact antinode of the electric field. The cavity beam waist at the dot layer is experimentally measured and shown to be in good agreement with the theoretical value. The cavity mode volume is calculated from the measured beam waist. The effect of weakly coupling a single dot to the cavity transverse modes is also investigated.

Photoluminesence data from a high dot density sample within the cavity is presented. An anti-crossing behaviour between an ensemble of dots and the cavity mode is demonstrated.

Finally, a dot dependent Fano effect in the absorption lineshapes in a charge-tunable sample is presented. A subtle interaction with an electronic continuum is revealed. The Fano effect is shown to become more pronounced with increasing excitation power.

Acknowledgements

I would like to thank my supervisor Prof. Richard Warburton for all his help and support during my PhD.

Thanks also to the everyone in the Nano-optics group at Heriot-Watt, in particular Paul Dalgarno for all his invaluable support and enthusiasm.

Finally, I would like to thank Robert L Barbour for his diligent proof reading of this thesis.

Contents

1 Background **1**

1.1 Introduction . . . 1
1.2 Quantum dots . . . 1
1.2.1 Epitaxial growth of self-assembled quantum dots . . . 1
1.2.2 Carrier confinement . . . 2
1.3 Electronic properties of quantum dots . . . 3
1.3.1 Radiative lifetime and oscillator strength . . . 3
1.4 Weak coupling (Purcell effect) . . . 4
1.4.1 Free space spontanteous emission rate . . . 4
1.4.2 Single-mode microcavity: Spontaneous emission rate . . . 5
1.5 Strong coupling . . . 6
1.5.1 Ensemble of atoms in the strong coupling regime . . . 7
1.6 Semiconductor microcavities . . . 7
1.6.1 Distributed Bragg reflectors . . . 7
1.6.2 Q-factor and finesse . . . 9
1.6.3 Micropillars . . . 10
1.6.4 Photonic crystals . . . 11
1.6.5 Microdisks . . . 12
1.6.6 Half symmetric Fabry-Pérot style resonators . . . 13
1.7 Thesis motivation . . . 14
1.8 Summary . . . 14

2 Methodology **15**

2.1 Introduction . . . 15
2.2 Photoluminescence . . . 15
2.2.1 Confocal microscope . . . 17
2.2.2 Microscope head alignment . . . 17
2.2.3 Spectrometer and charge-coupled device . . . 18
2.3 Time-Resolved Photoluminescence . . . 19
2.3.1 Introduction . . . 19

2.3.2 Time correlated single photon counting . . . 19
2.3.3 Pulsed laser . . . 20
2.3.4 Single photon avalanche photodiode . . . 20
2.3.5 Fits to lifetime data . . . 20
2.4 Photon correlation measurements . . . 21
2.4.1 Hanbury Brown-Twiss interferometer . . . 22
2.5 Wafer design and sample preparation . . . 24
2.6 Sample preparation . . . 26
2.6.1 Etching a mesa . . . 26
2.7 Single quantum dot absorption spectroscopy . . . 27
2.7.1 Charge-tunable sample . . . 29

3 A fully tunable microcavity 31
3.1 Introduction . . . 31
3.2 Cavity design . . . 32
3.2.1 DBRs . . . 32
3.2.2 Penetration lengths . . . 34
3.2.3 Cavity electric field and tuning curves . . . 35
3.3 Simulated cavity tuning plots . . . 37
3.4 Device realisation and experimental set-up . . . 38
3.5 Scanner calibration . . . 41
3.6 A length-tunable planar microcavity . . . 42
3.6.1 Planar cavity finesse and losses . . . 45
3.7 Curved mirror cavity . . . 46
3.7.1 Introduction . . . 46
3.7.2 Half symmetric cavity . . . 46
3.8 A microscopic concave mirror . . . 49
3.8.1 Laser ablation . . . 49
3.8.2 Atomic force microscope measurements . . . 51
3.9 Half symmetric cavity characterisation . . . 53
3.9.1 Low temperature test . . . 56
3.9.2 High finesse cavity . . . 57
3.10 Summary . . . 59

4 Quantum dots in a tunable microcavity 61
4.1 Cavity characterisation with PL at 77 K . . . 61
4.1.1 Q versus cavity length . . . 63
4.1.2 PL transverse mode spacings . . . 65
4.2 Quantum dots in a tunable cavity at 4 K . . . 66

4.3 Single quantum dot in a tunable cavity 69
4.3.1 Purcell effect : CW power dependence of the exciton 72
4.3.2 Correlation measurements 73
4.3.3 Long time-scale antibunching 74
4.4 Purcell Effect : time-resolved measurements 75
4.4.1 Spectral matching 76
4.4.2 Spatial matching 80
4.5 Calculating the mode volume 83
4.5.1 Cavity length 83
4.5.2 Cavity mode volume 83
4.6 Coupling transverse modes to a single dot 85
4.6.1 Radiative lifetime alterations 87
4.6.2 Calculated electric field profiles 88
4.7 Ensemble dot strong coupling: evidence 89
4.7.1 Curved mirror cavity 90
4.7.2 Fitting to the anti-crossing 92
4.7.3 Planar cavity 94
4.8 Summary 96

5 The nonlinear Fano effect 98
5.1 Linear regime: Fano lineshapes 99
5.2 Fitting the data 100
5.3 Nonlinear regime: lineshape evolution with power 102
5.4 Nonlinear Fano effect: model and assumptions 104
5.5 Carbon doping 108
5.6 Summary 109

6 Conclusions and future work 110

Publication list

Journal publications

M. Kroner, A. O. Govorov, S. Remi, B. Biedermann, S. Seidl, A. Badolato, P. M. Petroff, W. Zhang, R. J. Barbour, B. D. Gerardot, R. J. Warburton and K. Karrai. The nonlinear Fano effect. *Nature* **451**, 311 (2008).

A. Curran, R. J. Barbour, J. K. Morrod, K. A. Prior, A. K. Kar and R. J. Warburton. ZnSe hybrid microcavities fabricated using a MgS release layer, Strong and weak exciton-photon coupling. *J. Korean Phys. Soc.* **53**, 3007 (2008).

R. J. Barbour, A. Curran, P. A. Dalgarno, B. D. Gerardot, N. Stoltz, P. M. Petroff and R. J. Warburton. A fully tunable microcavity. In preparation for publication.

B. D. Gerardot, R. J. Barbour, D. Brunner, P. A. Dalgarno, N. Stoltz, A. Badolato, P. M. Petroff and R. J. Warburton. Characterizing positively charged excitons in a single quantum dot. In preparation for publication.

Conference presentations

R. J. Barbour, B. D. Gerardot, P. A. Dalgarno, D. Brunner, M. Kroner, K. Karrai, N. Stoltz, A. Badolato, P. M. Petroff, A. Govorov and R. J. Warburton. Fano resonances in the laser spectroscopy of a single quantum dot. *Compound Semiconductors UK*, Sheffield (2007).

R. J. Barbour, A. Curran, P. A. Dalgarno, B. D. Gerardot and R. J. Warburton. A fully tunable microcavity for cavity QED experiments. *Photon08*, Edinburgh (2008).

R. J. Barbour, A. Curran, P. A. Dalgarno, K. Nowak and R. J. Warburton. A fully tunable microcavity for semiconductor quantum electrodynamics experiments. *Invited seminar NIST Boulder*, Colorado (2009).

Chapter 1

Background

1.1 Introduction

The field of cavity quantum electrodynamics (CQED) has grown at a rapid rate since the early 1990s. In 1946 E. M. Purcell proposed that the presence of a microcavity with a small mode volume and high quality factor (Q) could alter an emitter's spontaneous emission rate. Experiments during the 1980s by Haroche and Klepner [1] confirmed that the spontaneous emission rate of an emitter was modified when embedded in a low volume, low loss (high Q) microcavity. Due to their narrow linewidths at 4 K and easy integration into heterostructures, semiconductor quantum dots are ideally suited for studying cavity quantum electrodynamics.

1.2 Quantum dots

1.2.1 Epitaxial growth of self-assembled quantum dots

A semiconductor quantum dot (QD) is a nanoscale structure which confines optical carriers in three dimensions [2]. One method for growing quantum dots is called Stranski-Krastinow growth [3]. An example involves growing monolayers of InAs on top of a GaAs matrix using molecular beam epitaxy (MBE). After 2.5 monolayers have been deposited, the built-in lattice mismatch causes dislocations forming strain-induced islands which are typically ≈20 nm in size (fig 1.1). These islands are known as quantum dots, and have a typical density of 1-100 dots/μm^2. Although this self-assembly process produces high quality quantum dots, it introduces experimental challenges when growing self-assembled dots in a monolithic microcavity structure - it is very difficult to grow a dot in a precise position in the cavity. This random spatial positioning leads to a spatial mismatch between the dot and the cavity mode's electric

field maximum. Furthermore, due to a 10% fluctuation in dot size and shape [4], the emission wavelength of individual dots range from ≈ 900-960 nm in the self-assembled InGaAs system. Therefore for a fixed cavity resonance there is likely to be a built-in spectral detuning between the dot and the cavity mode.

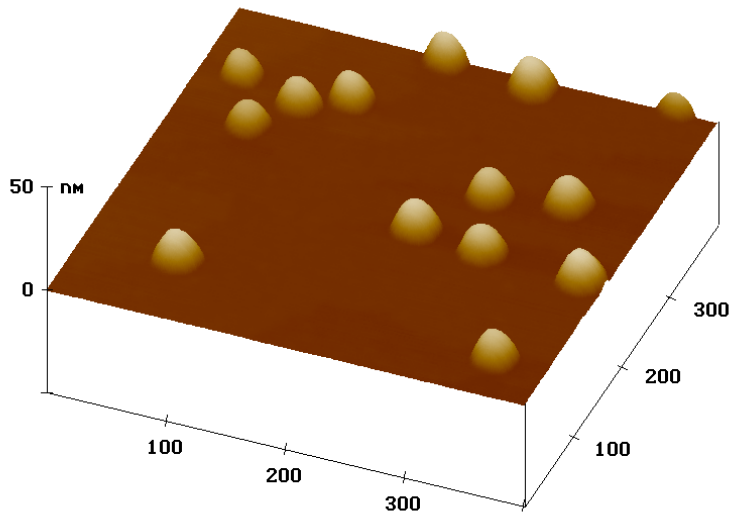

Figure 1.1: An atomic force microscopy (AFM) scan of InAs self-assembled quantum dots. Image taken by Axel Lorke. The dimensions are in nanometres.

1.2.2 Carrier confinement

Reducing the dimensions of a direct band gap semiconductor leads to quantisation of the continuum. Carrier confinement occurs in quantum dots because the confining region (physical size) is of the order of the electron and hole de Broglie wavelengths. The confinement alters the electronic density of states (DOS). The DOS in a bulk semiconductor increases monotonically as the energy in the band is increased, figure 1.2 (a). Bulk semiconductors therefore offer limited control over the optical properties and they must rely on doping effects to achieve a degree of control over the electrical properties by introducing an excess of carriers.

InGaAs quantum dots confine the optical carriers in all three dimensions and the modified DOS is shown schematically in figure 1.2 (b). The idealised DOS for a 0D (e.g. a quantum dot) structure is a set of discrete delta functions; it is these that lead to quantised energy levels in the QD [5]. In practice these lines are not delta

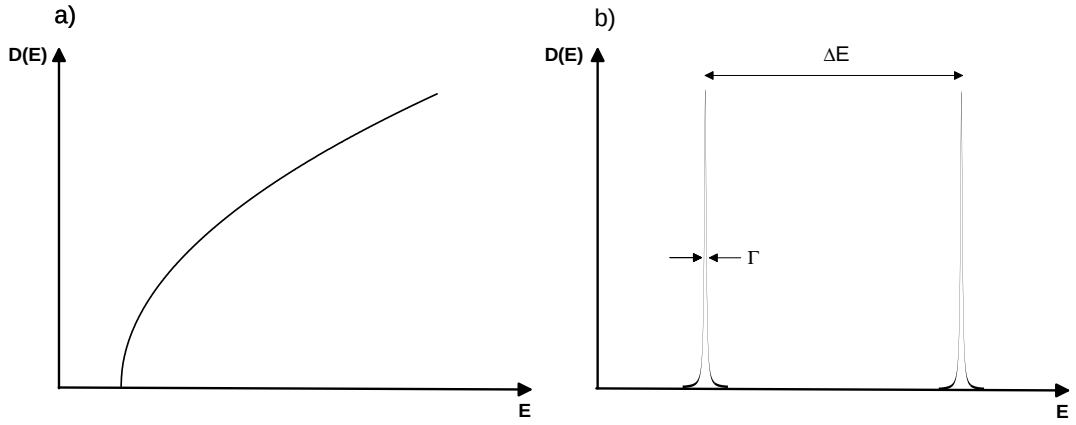

Figure 1.2: The electronic density of states for a) bulk semiconductor and b) quantum dots. The bulk DOS increases monotonically while the quantum dots DOS forms discrete lines.

functions, they have a Lorentzian lineshape with a finite width, $\Gamma \approx 5$ meV at room temperature and about 1 μeV at 4 K [6]. For InGaAs self-assembled quantum dots, the energy separation of the bound states, ΔE, is tens of meV. A quantum dot consists of many millions of atoms, however its optical properties resemble those of a single atom due to the confinement.

1.3 Electronic properties of quantum dots

1.3.1 Radiative lifetime and oscillator strength

A semiconductor quantum dot has a photoluminescence (PL) spectrum which consists of a set of discrete lines, corresponding to the various exciton transitions. The typical radiative lifetime of an InAs self-assembled quantum dot in GaAs is $\approx$ 1 ns [7]. Absorption measurements at 4 K indicate that the homogenous optical linewidth of a single InAs QD exciton is typically $\approx$1-3 μeV [6], close to the limit imposed by the radiative lifetime. A lifetime of 1 ns is equivalent to an optical linewidth of 0.7 μeV. The PL emission from a single quantum dot also displays a high degree of antibunching [8]. The oscillator strength, f_{osc}, is given by [9],

$$f_{osc} = \frac{2m_0\omega_e}{\hbar}\left(\frac{\mu_{12}}{e}\right)^2 \tag{1.1}$$

where m_0 is the free electron mass, ω_e is the angular frequency of the transition, μ_{12} is the optical dipole moment, $\hbar$ is Planck's constant and e is the charge of an electron. The spontaneous emission rate $(1/\tau)$ in free space is related to the oscillator strength by [9],

$$\frac{1}{\tau} = \frac{2n\pi e^2 f_{osc}}{3\lambda^2\epsilon_0 c m_0} \tag{1.2}$$

where τ is the radiative lifetime, n is the refractive index, λ is the wavelength and ϵ_0 is the permittivity of free space. The oscillator strength for a transition in a single dot is very large ($f_{osc} \approx 10$) [10] compared to single atomic transitions emitting at the same wavelength ($f_{osc} \approx 1$) [11].

1.4 Weak coupling (Purcell effect)

An enhancement of the spontaneous emission rate of an emitter in a microcavity is known as the Purcell effect [12] (weak coupling regime). The effect is due to the fact that an emitter's spontaneous emission rate depends in part on its environment. The Purcell effect has been observed in ensembles of dots [13], as well as single quantum dots in microcavities [14, 15, 16, 17, 18]. The Purcell effect can lead to an increased collection efficiency by funnelling emitted photons into the cavity mode. This is key to the efficient operation of single photon sources [14, 19, 20, 21, 22] and low threshold quantum dot lasers [23, 24].

1.4.1 Free space spontanteous emission rate

The spontaneous emission (SE) rate of an emitter in free space is given by Fermi's golden rule [25],

$$SE = \frac{2\pi}{\hbar^2}|\langle d.E\rangle|^2\rho(\omega) \tag{1.3}$$

where $|\langle d.E\rangle|^2$ is the probability that there will be transition, d is the dipole moment operator and E is the electric dipole operator. $\rho(\omega)$ is the available photon density of states (DOS). The photon DOS in free space is given by [25],

$$\rho_{free}(\omega) = \frac{V_{eff}\omega_e^2}{\pi^2 c^3} \tag{1.4}$$

where ω_e is the emitter frequency and V_{eff} is the effective volume that the emissive atom can emit into, which in free space can be considered to be very large. It can be shown that $|\langle d.E \rangle|^2$ can be written as [25],

$$|\langle d.E \rangle|^2 = \frac{\mu_{12}^2 \hbar \omega_e}{6\epsilon_0 \, V_{eff}} \tag{1.5}$$

Hence on substituting into Fermi's golden rule,

$$SE_{free} \equiv \frac{1}{\tau_{rad}} = \frac{\mu_{12}^2 {\omega_e}^3}{3\pi\epsilon_0 \hbar c^3} \tag{1.6}$$

where τ_{rad} is the radiative lifetime of the emitter. In free space the SE rate is proportional to the cube of the emission frequency.

1.4.2 Single-mode microcavity: Spontaneous emission rate

The SE rate from a single emitter coupled to a single optical mode in a microcavity is altered from its free space value due to the presence of the cavity. The cavity acts to enhance or suppress the photon DOS and therefore the SE rate of the emitter is not a fixed value, but depends on the emitter's environment. The photon DOS in a single mode cavity has a Lorentzian distribution, centered at frequency ω_c with a linewidth, $\Delta\omega_c$, given by [25]:

$$\rho_c(\omega_e) = \frac{2}{\pi \Delta\omega_c} \frac{{\Delta\omega_c}^2}{4(\omega_e - \omega_c)^2 + {\Delta\omega_c}^2} \tag{1.7}$$

The electric dipole matrix element for the emitter in the cavity can be written in a similar fashion to that in free space and by substituting (1.7) and (1.5) into Fermi's golden rule and utilising Q $= \omega_c / \Delta\omega_c$,

$$SE_{cav} = \frac{2\mu_{12}^2}{\hbar\epsilon_0} \frac{Q}{V_{eff}} \frac{{\Delta\omega_c}^2}{4(\omega_e - \omega_c)^2 + {\Delta\omega_c}^2} \tag{1.8}$$

The Purcell factor, F_p is the ratio of the emitter's SE rate in the cavity (1.8) to its SE rate in free space (1.6),

$$F_p = \frac{SE_{cav}}{SE_{free}} = \frac{\tau_{free}}{\tau_c} = \frac{3Q}{4\pi^2 V_{eff}} \left(\frac{\lambda}{n_{eff}} \right)^3 \frac{{\Delta\omega_c}^2}{4(\omega_e - \omega_c)^2 + {\Delta\omega_c}^2} \tag{1.9}$$

where n_{eff} is the effective refractive index of the cavity. When $\omega_c = \omega_e$ (i.e. when the cavity is tuned exactly into resonance with the emitter) the final term reduces to unity, thus maximising F_p.

$$F_p = \frac{3Q}{4\pi^2 V_{eff}} \left(\frac{\lambda}{n_{eff}} \right)^3 \tag{1.10}$$

Eqn 1.10 illustrates the need for high Q, low volume cavities to achieve a maximum Purcell effect. However this analysis only holds true for the weak coupling regime and also assumes that $\Delta\omega_e < \Delta\omega_c$. If the homogenous linewidth of the emitter is considerably bigger than the cavity linewidth then the Purcell effect is diminished [13]. The broad spectra of bulk semiconductors and quantum wells therefore hinders the observation of the Purcell effect, as their broad linewidths put a limit on the maximum useful cavity Q. Quantum dots with their narrow linewidths ($\approx$1 μeV) allow the use of cavities with very high Q-factors, which is a major benefit for observing a large Purcell effect.

1.5 Strong coupling

The weak coupling regime exists in an emitter/cavity system when the decay rates of the excited state and the cavity are both larger than the emitter-field coupling rate. In the weak coupling regime the emitted photon escapes the cavity before it can be re-absorbed by the emitter: the spontaneous emission process is irreversible in the weak coupling regime. If the cavity reflectivity is high enough so that an emitted photon remains in the cavity long enough to be re-absorbed by the emitter, then strong coupling is achieved. A signature of strong coupling is a splitting in the optical spectra when the cavity is resonant with the emitter. This splitting is called the vacuum Rabi splitting.

An anti-crossing is observed between the exciton and cavity mode with the spontaneous emission mechanism becoming a reversible process [26]. The strongly coupled system can be described by a generic coupled two-level model [27]. The magnitude of the Rabi splitting can be calculated using the coupled oscillator model [27],

$$\begin{vmatrix} E_c - E & \hbar V \\ \hbar V & E_x - E \end{vmatrix} = 0 \tag{1.11}$$

where E_c is the energy of the cavity mode, E_x is the exciton energy and $\hbar$V is the coupling between the exciton and the photon. Solving eqn 1.11 gives two solutions,

$$E_+ = \frac{1}{2}(E_c + E_x) + \frac{1}{2}\sqrt{(E_c - E_x) + 4 \mid \hbar V \mid^2}, \tag{1.12}$$

$$E_{-} = \frac{1}{2}(E_c + E_x) - \frac{1}{2}\sqrt{(E_c - E_x) + 4 \mid \hbar V \mid^2}. \tag{1.13}$$

In the weak coupling regime, the cavity and exciton lines cross at resonance ($E_c = E_x$). However, in the strong coupling regime the lines anti-cross. It can be shown that the observable Rabi splitting is given by [27],

$$\hbar\Omega = 2\sqrt{(\hbar V)^2 - \frac{1}{4}(\gamma_c - \gamma_x)^2}. \tag{1.14}$$

The observed Rabi splitting, $\hbar\Omega$ depends on the difference between cavity mode line width, γ_c and the exciton line width γ_x, with the maximum splitting when $\gamma_c = \gamma_x$. A key point is that the observed Rabi splitting scales with $1/\sqrt{V_{eff}}$, unlike the Purcell factor which scales with $1/V_{eff}$. Strong coupling was first observed in the solid state in 1992 in quantum well microcavities [28]. However it was not until 2004 that the first instance of strong coupling with a single quantum dot was reported [29]. Quantum dots are ideal candidates for exploring the strong coupling regime, due to their high oscillator strengths and the very small mode volume that is possible in solid state microcavities. The Rabi splitting of a single quantum dot exciton line, resonant with a high Q microcavity can be as large as 100 μeV [30], nearly two orders of magnitude larger than that of a cold atom trapped in a cavity [31].

1.5.1 Ensemble of atoms in the strong coupling regime

Recently strong coupling with a single atom in a microcavity has been demonstrated [31, 32, 33, 34]. The observed Rabi splitting is increased by a factor of $\sqrt{N}$ when N atoms are interacting with the cavity mode.

1.6 Semiconductor microcavities

A Fabry-Pérot optical cavity comprises two mirrors, separated by a small distance, L_{eff}. A Fabry-Pérot cavity has a resonant wavelength given by $\lambda_c = 2n_{eff}L_{eff}/m$, where m is the longitudinal mode index. If $L_{eff} \approx \lambda$, then the cavity is considered a microcavity.

1.6.1 Distributed Bragg reflectors

The mirrors used in microcavity technology are called Distributed Bragg Reflectors (DBRs) and are composed of multiple layers of alternating high and low refractive

index materials, such as TiO_2 ($n_H = 2.25$) and SiO_2 ($n_L = 1.45$). Each layer has a physical thickness of $\lambda_{sb}/4n$, where λ_{sb} is the optimal wavelength which the DBR is designed to reflect. Light is partially reflected from every layer boundary and light in a certain spectral region (the stopband) constructively interferes. This interference allows very high reflectivities ($R > 99.9\%$) to be achieved, which is very difficult with standard metallic mirrors ($R < 98\%$). A DBR also has significantly less absorption than a metallic mirror [35]. The DBR's reflectivity is a function of the refractive indices of the materials used and the total number N of dielectric pairs in the structure [36],

$$R = \left(\frac{1 - \frac{n_b}{n_a}(\frac{n_L}{n_H})^{2N}}{1 + \frac{n_b}{n_a}(\frac{n_L}{n_H})^{2N}} \right)^2, \tag{1.15}$$

where n_a and n_b are the refractive indices of the external media, n_H and n_L are refractive indices of the dielectric materials and N is the number of dielectric pairs.

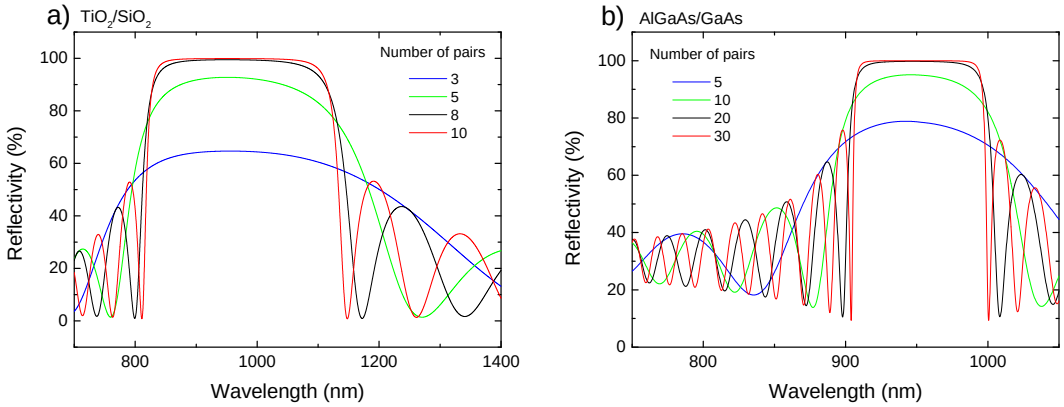

Figure 1.3: The number of pairs in the structure determines the reflectivity and width of the stopband. The semiconductor mirror requires more pairs to achieve the same reflectivity as the dielectric mirror. a) The simulated reflectivity of a dielectric DBR. The materials TiO_2 ($n_H = 2.25$) and SiO_2 ($n_L = 1.45$) are used in the simulation. The stopband is centred at 950 nm. b) Simulated reflectivity of a semiconductor DBR. The materials are AlGaAs ($n_L = 3.004$) and GaAs ($n_H = 3.5$).

The spectral width of the stopband is a function of the difference in the two refractive indices n_H and n_L [36]. The stopband width is calculated using [36],

$$\Delta_{sb} = \frac{2\lambda_{sb}\Delta n}{\pi n_{eff}}, \tag{1.16}$$

where the effective refractive index, $n_{eff} = 2(\frac{1}{n_H} + \frac{1}{n_L})^{-1}$.

Figure 1.3 compares the calculated reflectivity (equation 1.15) spectrum of a semiconductor and dielectric DBR. A dielectric DBR (a) requires fewer pairs to obtain a similar reflectivity to an equivalent semiconductor DBR (b), due to the larger difference in the two refractive indices in the case of the dielectric. A dielectric mirror composed of 10 pairs of TiO_2 (n = 2.25) and SiO_2 (n = 1.45) has a stopband width of about 300 nm, whilst the equivalent semiconductor mirror with 30 pairs of AlGaAs/GaAs will have a stopband of only about 100 nm (a factor of 3 narrower). The maximum reflectivity R is calculated to be 99.9% for the 10 pairs dielectric mirror and 99.99% for the 30 pairs semiconductor mirror.

There is significant penetration of the photons into DBRs, with the penetration length given by,

$$L_{DBR} = \frac{\lambda}{2n_{eff}} \frac{n_H n_L}{n_H - n_L}. \tag{1.17}$$

The effective cavity length, $L_{eff} = L_c + 2L_{DBR}$ is a combination of the length of the cavity region L_c and the penetration into the mirrors.

1.6.2 Q-factor and finesse

The quality factor (Q-factor) of a resonant optical cavity is a measure of how well the cavity confines photons. It can be shown that the lifetime of a photon τ_c (the time before a photon leaks out through one of the cavity mirrors) in a cavity depends on the reflectivity of the mirrors and also the cavity length [25],

$$\tau_c = \frac{n_{eff} L_{eff}}{c(1 - R_1 R_2)}, \tag{1.18}$$

where R_1 and R_2 are the mirror reflectivities, n_{eff} is the cavity refractive index and L_{eff} is the effective cavity length. The cavity Q-factor can be shown to be [25],

$$Q = \frac{2\pi n_{eff} L_{eff}}{\lambda(1 - R_1 R_2)} = \frac{2\pi c}{\lambda} \tau_c, \tag{1.19}$$

where λ is the emission wavelength of the cavity.

The cavity finesse, F, is a useful figure of merit for a microcavity. The finesse is defined as the free spectral range (FSR) divided by the band width of the cavity resonance. In theory the finesse depends only on the reflectivity of the mirrors. In the limit of large F (good cavity approximation), the finesse of a cavity can be used to calculate the reflectivity of the mirrors using [25],

$$F = \frac{\pi(R_1 R_2)^{1/4}}{1 - \sqrt{R_1 R_2}}. \tag{1.20}$$

The cavity finesse is related to the Q by [25],

$$Q = \frac{n_{eff} L_{eff} F}{\lambda} = \frac{\lambda}{\Delta\lambda}. \tag{1.21}$$

1.6.3 Micropillars

Micropillar cavities are MBE grown structures which are etched into free standing pillars of a few microns in diameter. Typically a λ layer of GaAs is grown between two semiconductor DBRs with a layer of InAs self-assembled QDs grown in the centre of the GaAs cavity layer. The DBRs provide longitudinal confinement of the optical mode, with the sidewall/air interface providing a degree of lateral confinement of the photons by total internal reflection. Lateral confinement reduces the mode volume, allowing a stronger interaction between the cavity mode and the dot. The Q-factor in a micropillar is predominantly limited by scattering from the sidewalls [37]. It has been shown that larger diameter pillars demonstrate higher Q-factors [37]. Below a certain critical pillar diameter (≈ 3 μm) sidewall scattering lowers the Q, indicating a lower photon lifetime for smaller pillars. However, it has been extensively reported that the Purcell effect is greater for smaller pillars (d ≈ 1 μm) despite the reduction of Q [13]. This is due to the smaller mode volume over-compensating for the lower Q [13].

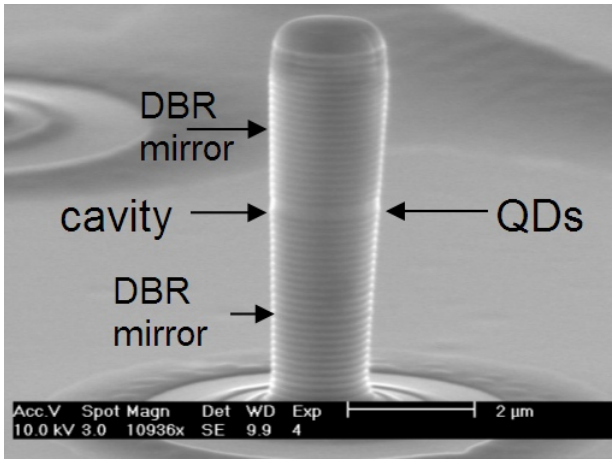

Figure 1.4: Scanning electron micrograph image of a micropillar. Figure taken from reference [38].

Figure 1.4 shows a scanning electron micrograph (SEM) of a micropillar. The Purcell effect has been observed for single dots in micropillar cavities, with Purcell

factors of up to 60 reported [39, 40]. The strong coupling regime was also achieved in a micropillar cavity for the first time in 2004 by Reithmaier et al. [29].

Micropillar: spectral tuning

The monolithic nature of the pillar cavity limits the resonant wavelength to the design wavelength - usually around 950 nm. The resonant wavelength is determined by the optical length of the cavity region. However fine tuning the cavity resonance to a single quantum dot is often achieved by varying the temperature of the system. The quantum dot excitons have a relatively high temperature dependence, whilst the cavity mode is less reactive to temperature change. The temperature is often varied by 20 - 40 K in order to locate the resonance. Increasing the temperature homogeneously broadens the neutral exciton's linewidth by as much as 2 μeV/K [41], however fine tuning the dot's wavelength using small temperature changes is a useful tuning method.

Tuning a quantum dot exciton into resonance with the cavity mode has also been achieved by utilising an electric field-induced Stark shift [40, 42]. This method reduces the need to alter the temperature. However, the method is limited to very small changes in emission wavelength ($\approx$ 3 nm) and involves some difficult fabrication.

Micropillar: quantum dot spatial positioning

A dot will only interact optimally with a pillar if it is placed at the antinode of the electric field. In a symmetrical pillar, the antinode is located at the very centre in the xy plane. However, currently there are no methods available to position a single quantum dot in the pillar, either during the growth phase or in situ. In order to have the best chance of finding a quantum dot which is matched spatially to a pillar, dozens of pillars are etched in large arrays and each pillar is systematically searched to find the dot which demonstrates the highest Purcell effect. This is a time consuming and inefficient process.

1.6.4 Photonic crystals

Photonic Crystals (PCs) are dielectric or semiconductor structures which have a periodic modulation of the refractive index in the plane. Bragg diffraction allows the propagation of a discrete set of modes whilst forbidding others, giving rise to a spectral region in which photons cannot propagate, known as the photonic band gap (PBG). Periodic modulation of the refractive index is achieved by etching a series of holes in the structure. Maintaining exact periodicity and fabricating the array of holes on a

small enough scale (comparable to the wavelength of the light) is very challenging. Figure 1.5 shows a photonic crystal cavity. There are two main types of photonic crystal microcavity [43], S1 (square array) or L3 (triangular array).

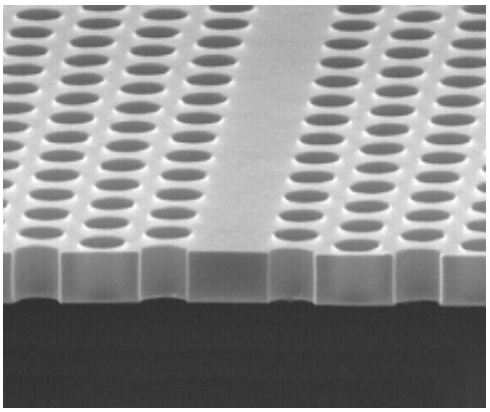

Figure 1.5: An SEM image of an GaAs L3 photonic crystal microcavity. The periodicity of the structure is about 1 μm. The image was taken from reference [44].

Photonic crystal microcavities demonstrate small mode volumes ($V_{eff} = 0.3(\lambda/\mathrm{n})^3$) and very large Q-factors (Q > 20,000). Both the strong [30] and weak coupling [45] regimes have been achieved with a single quantum dot embedded in a photonic crystal cavity. However, similar to micropillar cavities, the PC cavity has very limited spectral and spatial tuning ability, reducing the advantages of the high Q and low mode volume. Badolato et al. were able to spatially position a quantum dot in the photonic crystal by marking the location of single quantum dots with a matrix of gold markers and fabricating a cavity around a particular dot, using SEM and photolithography techniques [46]. Badolato et al. also successfully positioned a single dot to within 25 nm of the electric field maxima in the photonic crystal [46]. Badolato et al. [46] approached the tunability issues in photonic crystal cavities by developing a technique which tunes the *cavity* mode into spectral resonance with the dot using a digital etching technique [45]. The photonic crystal is etched in citric acid, enlarging the holes in the crystal. This modifies the cavity, tuning the cavity wavelength in steps of $\approx$ 3 nm per etching cycle. Fine tuning was accomplished by temperature tuning the dot. Nitrogen deposition can also be used to spectrally tune the cavity mode [47].

1.6.5 Microdisks

Microdisks are semiconductor disks, typically a few microns in diameter and less than a micron thick. Microdisks confine light by total internal reflection, supporting

whispering gallery modes (WGMs) around the edge of the disk. A semiconductor microdisk, such as the one pictured in figure 1.6, can show a Q-factor of 12,000 and 17,000 for a disk diameter of 1.8 μm [48] and 4.5 μm [24] respectively. Q is limited by sidewall morphology [24], similar to micropillars. Large disks have a relatively large mode volume compared to PC cavities. The Purcell effect from single quantum dots embedded in microdisk cavities has been observed [18] . However, microdisks suffer from poor collection efficiency and it is very difficult to match spatially the dot to the electric field maximum of the WGM. Despite these experimental challenges, strong coupling has been achieved with a single quantum dot in a microdisk cavity [49].

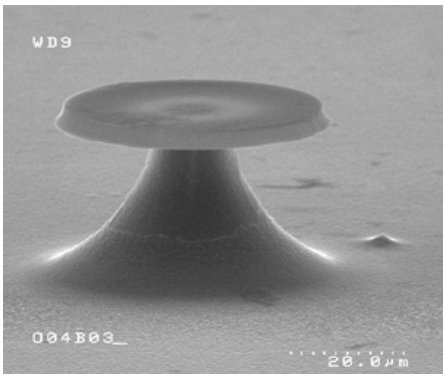

Figure 1.6: An SEM image of a semiconductor microdisk. The image was taken from reference [50].

1.6.6 Half symmetric Fabry-Pérot style resonators

Fabry-Pérot style microcavities utilising an air gap to allow atoms to pass through the cavity have been used for years in atomic optics [51]. In macroscopic Fabry-Pérot style cavities, a concave mirror is used to confine the light in the lateral plane to decrease losses. This has been achieved with some success in microcavities [33]. However new techniques have had to be developed to manufacture spherical mirrors with a suitable radius of curvature, $R \leq 100$ μm. Two techniques have been successfully realised for this process. The first method, successfully used by Cui et al. (2006) [52], has been to trap a micron-sized air bubble in molten glass and then to cut the bubble open once the glass has cooled, exposing a smooth spherical surface for subsequent coating. A finesse of several hundred has been demonstrated using this approach, thought to be limited by physical vibrations of the mirrors broadening the cavity mode. However only very long cavity lengths have been realised by this method ($L_{eff} > 60$ μm), and no significant interaction with a single quantum dot has been demonstrated. A second method has been developed by Prakash et al. [53], which utilises glass spheres as templates for electrochemical growth of reflective metal around them. Etching the templating spheres leaves spherical mirrors with radii of curvature as small as 100 nm.

However this approach does not allow very high Q-factors due to the relatively low reflectivity of the metallic coating ($\approx 95\%$). Typically Q = 300 for a cavity length of 10 μm.

1.7 Thesis motivation

The primary advantages of monolithic microcavity structures has been that quantum dots are in a solid-state system and cannot move around spatially as atoms do. However the major disadvantage faced by monolithic microcavities to date, is the difficulty of ensuring spatial and spectral overlap of the dot and the cavity modes. Precise design and fabrication is required to achieve this in monolithic cavity structures with some degree of success. This thesis presents an elegant solution that addresses these disadvantages. Chapter 3 details the development of the tunable cavity technology, whilst chapter 4 presents experimental evidence of the Purcell effect from a single dot in the cavity.

1.8 Summary

Quantum dots are nanometer sized emitters which confine electrons and holes. Quantum dots exhibit nearly lifetime limited optical linewidths at 4 K. Their narrow linewidths and high oscillator strength make them ideal candidates for cavity QED experiments. Several cavity systems exist (micropillar, photonic crystal and microdisk) which have demonstrated strong and weak coupling with a single quantum dot. However although these microcavity systems demonstrate high Qs and low mode volume they involve complicated fabrication steps and pose many experimental challenges such as the spatial and spectral matching of a point source emitter to the cavity mode maximum. These challenges arise due to the monolithic nature of solid state cavities, combined with the random size and spatial location of self-assembled quantum dots in such cavities.

Chapter 2

Methodology

2.1 Introduction

This chapter introduces the experimental methods that were used to perform the single quantum dot photoluminescence (PL) experiments, including time-resolved measurements. The confocal microscope set-up described in this chapter is crucial to the experimental work presented in later chapters and it has been a fundamental tool in the Nano-Optics group at Heriot-Watt for several years [54]. The quantum dot DBR sample used to perform the cavity-dot coupling experiments covered in chapters 3-5 is also described in this chapter. Finally, a charge-tunable structure and single dot absorption technique is described.

2.2 Photoluminescence

Quantum dot PL involves producing carriers in the continuum states of the sample by exciting with a laser. The carriers then undergo fast relaxation to form one of the lowest energy configurations in the dot. Finally the electron hole pairs recombine to emit a single photon. At low temperature, the observed spectra for such a process is typically a set of narrow lines at different energies corresponding to the different transition energies of the quantum dots. The ability to isolate a single quantum dot requires a microscope with high spatial resolution, high throughput and high stability for low temperature operation. This section describes the experimental set-up used to measure the PL from a single dot at 4 K.

The set-up for single quantum dot photoluminescence measurements is shown in Figure 2.1. This experimental set-up can be divided into four main sections. Section A in figure 2.1 includes the excitation laser, coupling fibre and collimating lens. The

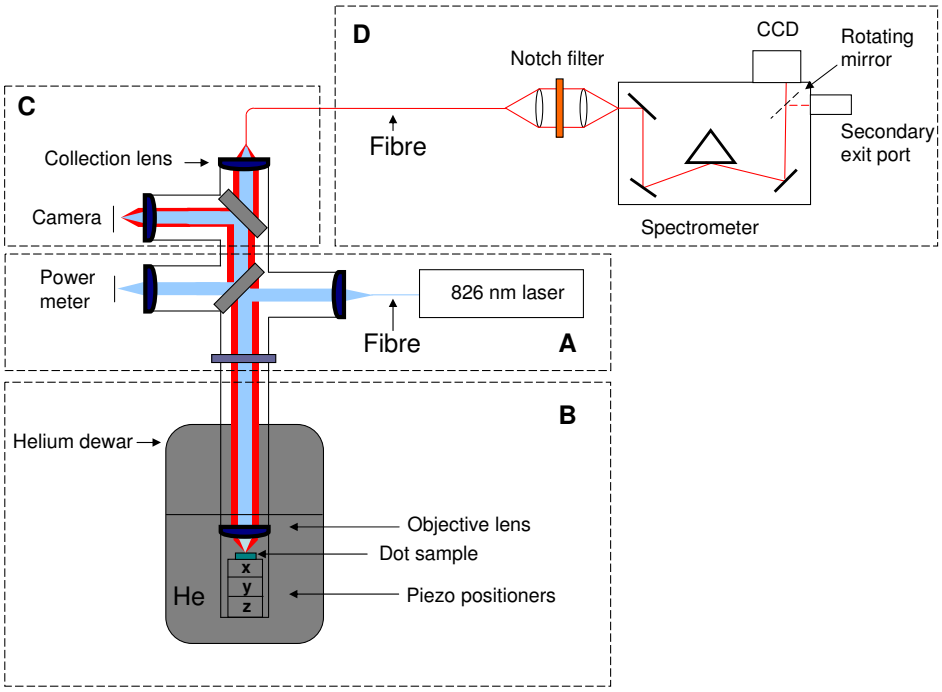

Figure 2.1: A schematic diagram of the photoluminescence experimental set-up. A) The excitation laser, lower beam splitter (grey) and power meter. B) The helium dewar (dark grey), dot sample (green) and the Attocube piezo positioners. C) The collection arm of the microscope head, upper beam splitter (grey) and camera for alignment. D) Collection fibre (red), spectrometer coupling optics, and the spectrometer with liquid nitrogen cooled CCD.

sample is excited with a 40 mW continuous wave (CW) single mode laser diode with a wavelength, $\lambda = 826$ nm. The laser light is coupled into a 4 m long 850 nm single mode optical fibre and is then collimated at the microscope head with an aspheric lens (Geltech C230TM-B), which is anti-reflection (AR) coated to ensure maximum throughput at the excitation wavelength. The collimated beam (light blue) is then incident on the glass beamsplitter in the microscope head which allows 92% to be transmitted through and onto the Thorlabs power meter whilst 4% is reflected from the first surface of the beam splitter, down to the objective lens and the sample. Section B in figure 2.1 includes the objective lens (Geltech C230TM-B) with a numerical aperture (NA) of 0.55 which is used to focus the incident light to a theoretically diffraction limited spot size of 800 nm at the sample surface. The sample is mounted on the top of a piezo positioning stack (Attocube ANPxyz100) which allows precise low temperature positioning of the sample relative to the focal point of the excitation beam, in all three dimensions. The sample and piezo positioning stack are mounted on the end of a 1.2 m long microscope assembly, constructed from Thorlabs cage plates and rods. The microscope allows the objective lens, sample and positioners to be

mounted in a 1.2 m long thin-walled stainless steel tube. The tube is then evacuated to a pressure of 10^{-5} mbar and filled with helium exchange gas to a pressure of 30 mbar. This process prevents moisture from the air condensing and freezing on the piezo positioners as the tube is cooled down. The whole assembly is then pre-cooled in liquid nitrogen which lowers the temperature to 77 K, then lowered into a liquid helium dewar which further reduces the temperature to 4 K.

2.2.1 Confocal microscope

The PL emission from a single quantum dot is collected via the objective lens. Isolating a single dot is possible due to the system's confocal arrangement - the microscope only collects the rays which come from a small area in the vicinity of the focus. The single mode collection fibre (core diameter ≈ 5 μm) acts as a pinhole, rejecting any rays with an origin outside the focus. This spatial resolution is diffraction limited, determined primarily by the NA of the objective lens (0.55). The design is highly stable with negligible drift, allowing a single quantum dot to be studied over several weeks.

Around 84% of the PL collected by the objective lens is coupled into a 950 nm single mode optical fibre. The remaining 16% is lost due to 8% being reflected back down the microscope from the lower of the two beamsplitters and 8% by the upper beamsplitter (4% is directed to the alignment camera), Figure 2.2 (a).

2.2.2 Microscope head alignment

The PL from a single quantum dot is typically very weak, therefore careful alignment of the excitation and collection arms is crucial. This is especially important when using the time correlated techniques described in section 2.3: a factor of two reduction in the collected PL intensity increases the required integration time by a factor of four for correlation measurements. Firstly, the excitation arm is removed from the head and the 826 nm beam is centred (using an xy translation stage) so that it passes directly through the centre of the collimation lens. The beam is then collimated over the length of the laboratory (10 m). This is repeated with the collection arm, using in this case a continuous wave 950 nm laser for alignment purposes. A tilt stage at the base of the microscope head allows the 950 nm collimated laser beam to be centred directly down the 1.2 m microscope. Two Thorlab pinholes temporarily placed in the microscope aid this alignment procedure. The sample is then moved to the focus of the objective lens with the aid of the imaging camera in the head. The camera is also used to ensure that the focussed spot is symmetrical and is not clipping the side of

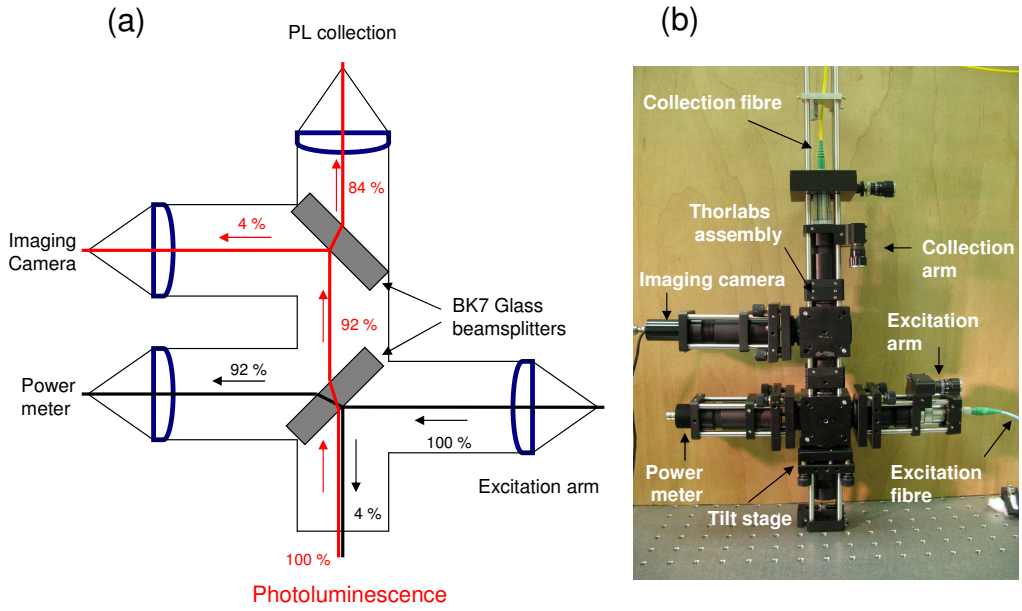

Figure 2.2: a) A schematic diagram of the microscope head showing the path of the excitation laser (black) and PL collection (red), and b) a photograph of the head that shows the outer housing and tilt stages used for alignment.

the objective lens. Finally the excitation arm is aligned in the same way and the laser spots from the two independent arms are overlapped using the imaging camera.

2.2.3 Spectrometer and charge-coupled device

The PL collection fibre is coupled into a dispersive grating spectrometer (Figure 2.1, section D). A holographic notch filter in the coupling optics filters out the excitation laser. The filter has a very narrow spectral bandwidth with a full width at half maximum (FWHM) of 20 nm. Without this filter the scattered light in the spectrometer from the excitation laser would dominate the spectrum, obscuring the relatively weak dot PL signal. The PL is dispersed by a blazed grating which has 1200 lines/mm. The spectrometers path length is 0.5 m. This gives a spectral resolution of 70 μeV. The PL is collected on a liquid nitrogen-cooled silicon charge-coupled device (CCD).

The CCD chip has an array of 1340 x 100 pixels, each pixel is 20 μm x 20 μm. The temperature of the CCD is held at -100 °C, therefore the dark count is negligible and the system's background is defined by read-out noise which is around 90 counts per pixel. The quantum efficiency of the camera at 950 nm is 30%.

The secondary exit port can be accessed via a rotating mirror which is flipped to redirect the beam, sending the light to a single photon avalanche photodiode (SPAD) for time-resolved measurements.

2.3 Time-Resolved Photoluminescence

2.3.1 Introduction

Time-resolved photoluminescence (TRPL) experiments measure the decay rate of a exciton in a single quantum dot. At low temperatures below 30 K the decay rate is dominated by radiative decay [55]. The radiative lifetime, τ_{rad}, is typically around 1 ns at 4 K [7]. The dot's lifetime provides crucial information about the intrinsic properties of the dot, such as oscillator strength and its free space spontaneous emission rate. This section also introduces the techniques which were used to demonstrate the Purcell effect in chapter 4.

2.3.2 Time correlated single photon counting

Time correlated single photon counting (TCSPC) is a well established technique for studying the temporal properties of atoms, molecules and semiconductors [56]. TCSPC measures the time delay between exciting the sample and detecting an emitted photon. This is accomplished by sending a laser pulse to excite the sample whilst simultaneously starting an electronic timer. The PL signal is collected and filtered by the spectrometer grating (resolution $\approx$ 70 μeV) thus ensuring only light emitted from a small spectral window is detected. The light is then directed to a single photon avalanche photodiode (SPAD) which sends an electrical pulse to the timing electronics, stopping the counter. The process is repeated millions of times and a histogram of the events is produced. This process relies on the ability to detect single photons and the use of extremely precise, fast and accurate timing electronics. A schematic diagram of the process is shown in Figure 2.3.

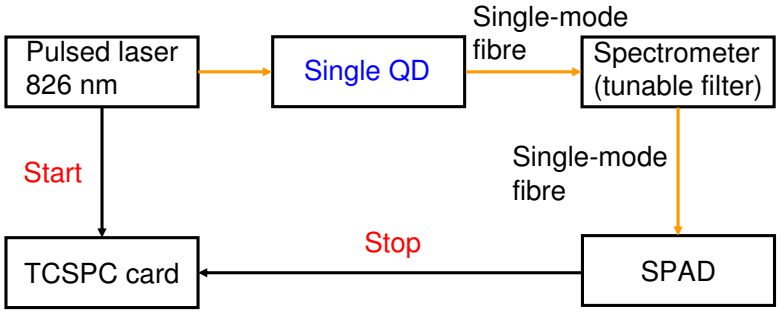

Figure 2.3: A schematic of the TCSPC experiment.

2.3.3 Pulsed laser

The single quantum dot was excited with an electrically pulsed 826 nm laser diode from PicoQuant. The driver can pulse the diode at repetition rates up to 80 MHz with a sub 100 ps pulse duration. Pulse to pulse jitter is 2-3 ps. Approximately 40% of the laser light is coupled into the excitation arm and then 4% reflected down to the sample, ensuring the excitation power at the sample is below 1 μW (average power).

2.3.4 Single photon avalanche photodiode

The SPAD used in this work to record the stop counts is made by PerkinElmer Optoelectronics. It has a dark count rate of 70 cs^{-1}, an instrumental response of 400 ps and a quantum efficiency of 25% at 950 nm. The SPAD is electrically cooled and is operated at many tens of volts above its breakdown voltage [57]. A fibre connector at the front of the SPAD enables easy integration into a fibre-based system. When the SPAD detects a photon, it sends an electrical pulse to the timing electronics. To avoid possibly damaging the SPAD, the count rate was kept below 1 MHz.

2.3.5 Fits to lifetime data

The measurement of the radiative lifetime requires treatment of the detector's response, due to $\tau_{rad} \geq \tau_{response}$. Fitting curves to the data is accomplished with the

software that runs the timing electronics. The software from Edinburgh Analytical Instruments utilises the well known mathematical technique of convolution to obtain accurate fits to the data. The accuracy of the fits relies on recording the instrumental response for the experimental set-up [56]. The instrumental response was recorded daily and for several different laser settings during the experiments described in this work, to ensure accurate fits. Residuals to the fit, the difference between the fit and the raw data, are also generated by the software. An example of a good fit to lifetime data and the corresponding residual is shown in Figure 2.4. The fit indicates that the decay is mono-exponential and that the radiative lifetime is 0.85 ns. The residual has a featureless offset, fluctuating around zero, indicating that a good fit has been achieved. The data was taken at low excitation power (0.18 μW/μm^2) to ensure a good fit. At high excitation powers the convolution fits to a single exponential decay deteriorate due to an increased probability that the dot will capture multiple excitons giving rise to multi-exciton cascade process, causing the decay curves to saturate [58, 59]. As a consequence, all the lifetime measurements presented in this thesis were taken at low average power density ($\leq$0.2 μW/μm^2).

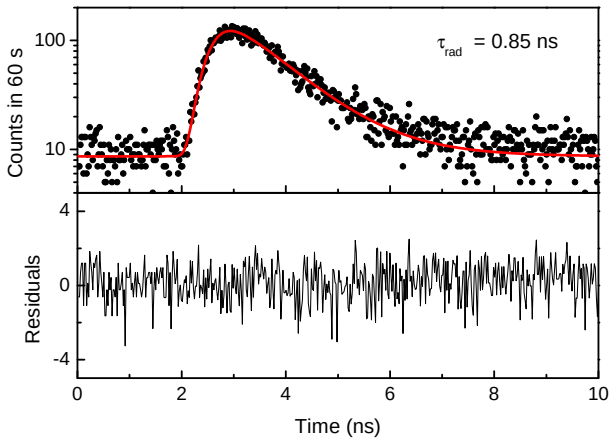

Figure 2.4: An example of lifetime data from a single quantum dot exciton (wafer 61004C) at 4 K. The corresponding convolution fit (red) indicates a lifetime of 0.85 ns. The bottom graph shows the residuals between the data and the fit.

2.4 Photon correlation measurements

In quantum dot experiments it is often important to ensure that only a single isolated quantum dot is contributing to the observed spectra. The most reliable way to ensure this is by measuring the photoluminescence and determining whether the emission is

antibunched, bunched or coherent. A single dot at 4 K emits antibunched light [8], whilst more than one dot does not. This section introduces the intensity interferometer used to measure the second order correlation function, $g^{(2)}(\tau)$, of a single quantum dot's emission.

2.4.1 Hanbury Brown-Twiss interferometer

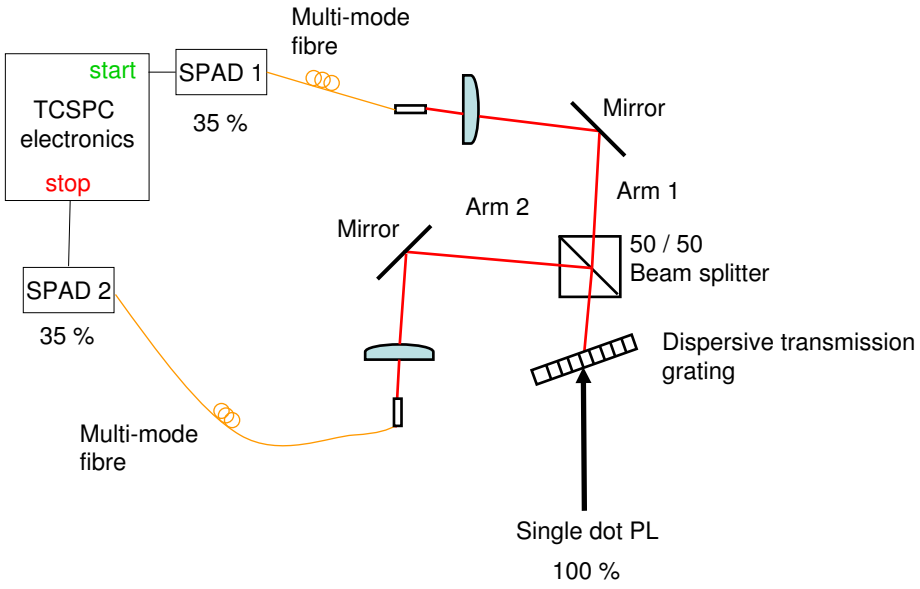

Figure 2.5: A Schematic diagram of the custom-built Hanbury Brown-Twiss interferometer. The PL is transmitted through a grating and is divided by a 50/50 beam splitter. The grating and the 2 rotating mirrors allow each arm to be independently spectrally tuned. The SPAD in arm 1 acts as a start signal and the SPAD in arm two as a stop signal.

Photon correlation measurements are performed with a Hanbury Brown and Twiss (HBT) interferometer. The concept behind the HBT is that the coherence properties of light can be determined by measuring the intensity of a beam of light on two detectors and by examining the correlation between the intensity of the two signals. In 1956 Hanbury Brown and Twiss used this technique to produce a new type of stellar interferometer [60]. Photon antibunching from a single atom was first demonstrated in 1977 by Kimble et al. using an HBT [61].

The HBT set-up for photon correlation experiments is shown in Figure 2.5. It was custom-built by a fellow PhD student (D. Brunner). The PL emission is collected

as described in section 2.2, the emission is then incident on a dispersive transmission grating. The transmission grating splits the beam spectrally. A rotating mirror in each arm is used to select the required wavelength between 900 nm and 1000 nm with a resolution of 350 μeV. Each arm is tuned to the PL emission wavelength using a broad band white light source at the input and observing the collected light on the spectrometer. A beam splitter then splits the PL emission (red line), 50% to arm 1 and 50% to arm 2. Both arms contain an identical SPAD (timing jitter $\approx$ 400 ps), with arm 1 providing the start pulse and arm 2 providing the stop pulse.

Typically the HBT has a 70% throughput, corresponding to 35% of the input signal incident on each SPAD. The time delay, τ, between the two signals is recorded and rendered into a histogram which provides a good approximation to the second order correlation function, $g^2(\tau)$. For pulsed excitation the $g^2(\tau)$ plot consists of a series of peaks, separated by delays between the pulses. Figure 2.6 shows a correlation measurement of PL emission from a single quantum dot exciton. In this case there is a significant reduction in counts at $\tau = 0$, indicating that the light is antibunched.

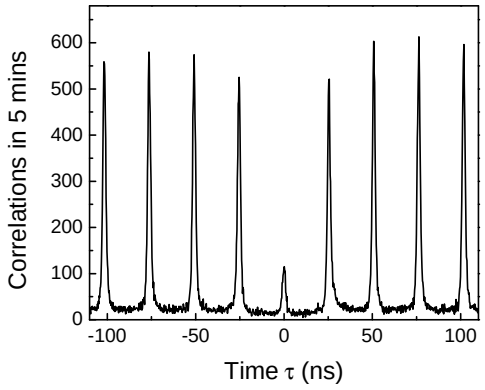

Figure 2.6: The measured correlation function, $g^2(0)$ for a single quantum dot exciton (wafer 61004C) under 40 MHz pulsed laser excitation. The excitation power was 0.1 $\mu W/\mu m^2$.

A perfect single photon source would have $g^2(0) = 0$. However, if $g^2(0) < 1$ then the light is antibunched and if $g^2(0) \leq 0.5$, then the emitter is a single photon source. The required integration time for a particular histogram is inversely proportional to the product of the two SPAD count rates. A cavity can therefore dramatically reduce the integration time required to build up a histogram, by increasing the PL collection efficiency.

2.5 Wafer design and sample preparation

This section describes the semiconductor DBR quantum dot sample used in the experiments in chapters 3 and 4. The wafer (no. 61004C) design consists of a lambda layer of self-assembled quantum dots on top of a DBR. This provides the bottom mirror and dots for the cavity experiments described in chapters 3 and 4. The wafer was grown by N. Stoltz in Santa Barbara, California on a 2 inch GaAs wafer. A schematic representation of the wafer structure is shown in Figure 2.7.

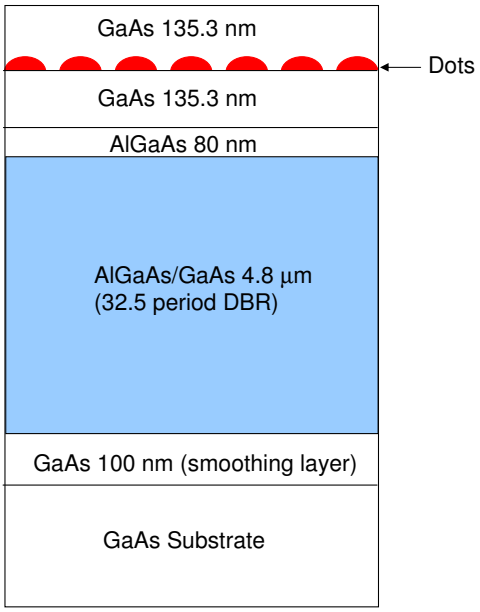

Figure 2.7: Schematic diagram (not to scale) of the semiconductor heterostructure (wafer 61004C).

A 100 nm smoothing layer is grown on top of the GaAs substrate. A 32.5 period DBR is then grown on top of the smoothing layer. This comprises 64 alternating quarter wavelength layers (at 950 nm) of undoped AlGaAs/GaAs with refractive indices at low temperature of 3.009 and 3.54 respectively [62]. An extra layer of AlGaAs is then grown, to ensure compatibility with the top dielectric mirror which completes the cavity (see chapter 3). The small amount of gallium which is added in the AlGaAs layers helps reduce the rate of AlAs oxidation, prolonging the life of the sample [63]. The maximum reflectivity of the 32.5 period DBR is R = 99.999%,

calculated from equation 1.15 [36]. Finally a lambda layer of GaAs is grown on the top of the DBR structure, with a layer of InAs self-assembled quantum dots in the centre.

The dots emit between 900 nm and 960 nm. The dot density decreases linearly across the wafer (due to an uneven InAs distribution). This allows samples of variable dot densities to be cleaved from the wafer as required. Figure 2.8 shows the PL emission from a high dot density sample in free space at (a) 77 K and (b) 4 K. A quantum dot's emission energy depends on its size, with larger dots emitting at a lower energy. Despite the small collection spot size, the microscope collects PL emission from thousands of different dots on a high density sample, therefore there is a distribution of dot sizes all contributing to the PL spectra in Figure 2.8 (a). The resulting broad band PL emission at 77 K has two peaks indicating a bimodal dot distribution. The PL peak centred at 930 nm (FWHM $\approx$ 20-30 nm) is useful for cavity characterisation (chapter 3) as it acts as an intense, internal broad band light source in the cavity.

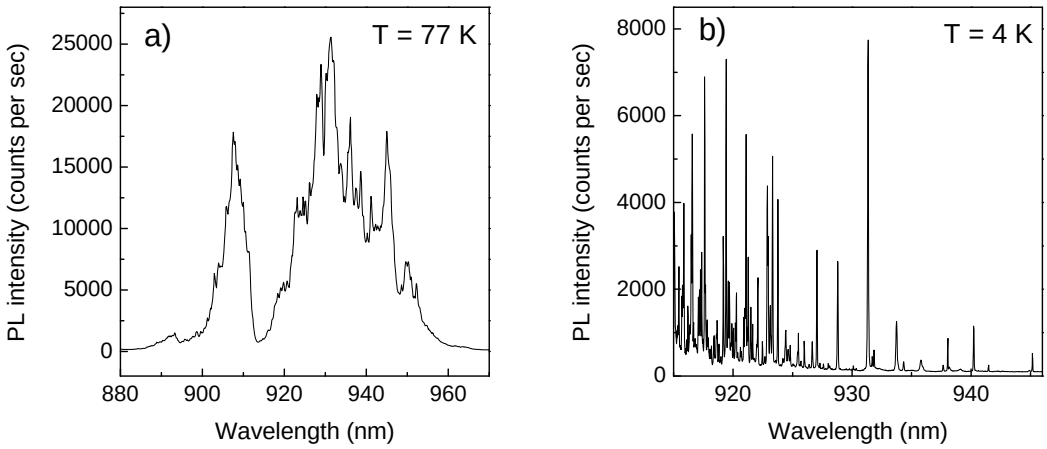

Figure 2.8: PL from a high density part of the wafer (61004C) a) from an ensemble of dots at 77 K a bimodal distribution is observed and b) spectrally isolated single dots can be seen between 930 and 950 nm at 4 K.

The same sample can be used to perform single quantum dot/cavity experiments at 4 K, despite the high dot density ($\approx 10^{10}$ dots/cm^2). Due to the inhomogeneous broadening, a single dot can be spectrally isolated at higher wavelengths (930-950 nm range) at the tail end of the high density array, Figure 2.8 (b).

2.6 Sample preparation

The 2 inch wafer (61004C) must be cleaved into much smaller sample pieces to enable incorporation in the experimental apparatus. The small sample pieces must be thoroughly cleaned to ensure the surface is free from any dust or contamination. This step was crucial in preventing any particles being trapped between the semiconductor mirror and the external top mirror, whilst fabricating cavities. The wafer was spin coated with photoresist to protect the surface from dust. It was then cleaved along the major crystal axes to form samples of approximately, 3 mm x 3 mm. The samples were meticulously cleaned in acetone and then rinsed in IPA to wash off the protective photoresist coating and remove any dust from the cleaving process.

2.6.1 Etching a mesa

In the cavity experiments described here, dust between the cavity mirrors is a major concern. Minimising the cavity volume means minimising the gap between the top and bottom mirrors. A single particle of dust between the mirrors will increase the minimum cavity length, which is undesirable. To reduce the chance of dust particles on the surface of either mirror interfering with the cavity, it would be preferable to work with samples with much smaller surface areas than 3 mm^2. However smaller sample sizes are difficult to produce, more difficult to handle and to mount in the cavity housing. Using standard lithography techniques, a simple solution was to etch a small mesa of diameter 500 μm into the surface of the cleaned sample.

This was done as follows. Firstly, a small area of photoresist was dabbed onto the sample surface, using a single fibre from a paintbrush. The photoresist on the sample's surface forms a roughly circular profile, with a meniscus cross section. Typically a diameter of around 500 μm is easily achieved without the need for a photolithography mask. The sample is then carefully placed in an oven and left for an hour at 80°C to allow the photoresist to harden. The sample is then etched in a solution of sulphuric acid (H_2SO_4), hydrogen peroxide (H_2O_2) and water in a ratio of $1 : 8 : 200$ for 35 mins. This process etches the GaAs and the DBR to a depth of ≈ 5 μm forming a mesa structure (Figure 2.9). The small surface area presented by the mesa reduces the chance of any dust in the cavity, thus ensuring the gap between top and bottom mirrors can be completely closed. Any dust around the base of the mesa must be larger than 5 μm to interfere with the top mirror, otherwise it is insignificant to the cavity operation. Although the mesa helps to minimise the cavity air gap, it is not in itself a complete solution and is no substitute for thorough cleaning of both mirrors in a dust free environment.

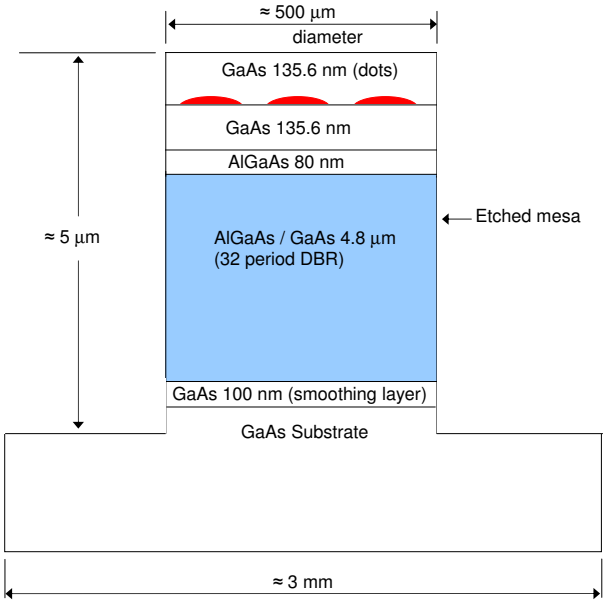

Figure 2.9: Schematic diagram of an etched sample. The DBR has been completely etched, leaving a free standing pillar with a diameter of 500 μm.

2.7 Single quantum dot absorption spectroscopy

PL spectroscopy is commonly used to probe the optical transitions of quantum dot excitons. However whilst it is useful for characterising the energy levels and charged states in a dot, the relaxation process reduces coherence. Laser spectroscopy measures the differential transmission dip in the absorption spectrum of a single quantum dot as a function of laser detuning. This provides information on the true optical line shape and linewidth [6, 9, 64]. The key concept is the detection of a subtle interference effect from mixing the laser signal with the weak quantum dot signal (homodyne detection). The detector measures the interference effect which is evident as a dip in the transmission signal.

The technique utilises a narrow linewidth laser ($\approx$ 1 MHz) to excite resonantly a transition. A detector (Thorlabs FDS 100) placed underneath the sample collects the transmitted laser light. A transmission spectrum was obtained by using the Stark shift to sweep the dot exciton transition energy through the probing laser energy which was kept fixed. At the same time a small square-wave modulation at a frequency of 100 Hz and amplitude of 0.06 V was superimposed onto the gate voltage. The ac part of the signal was demodulated using the lock-in (which measures the signal in a small bandwidth). This technique ensures that a differential transmission signal is only obtained when an exciton is resonant with the laser.

The experiment is non-trivial due to the small magnitude of the change in the

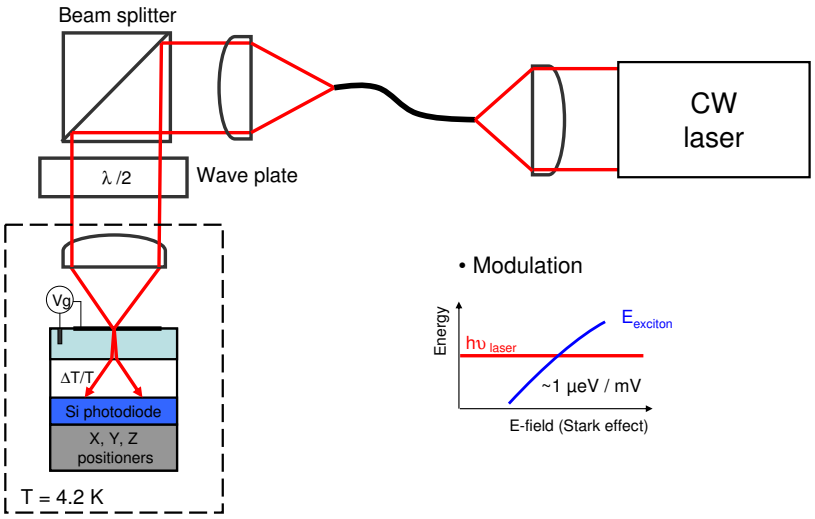

Figure 2.10: Schematic of the laser spectroscopy experimental set-up.

optical signal. A current amplifier (Femto DLPCA-200) was used to amplify the signal, which was sent to a lock-in amplifier to measure the differential transmission signal. Figure 2.10 shows the experimental set-up used to perform the spectroscopy experiment. The narrow band laser was tuned to the resonance of a single quantum dot (identified in PL), the laser light was linearly polarised using a $\lambda/2$ wave plate to maximise contrast. The maximum contrast for a neutral exciton (X^0) in an n-doped sample with a solid immersion lens (SIL) on the sample surface is $\approx 6\%$ [65]. However, a contrast of 1 % is more typical from n-doped samples and p-type gives only about 0.1 %.

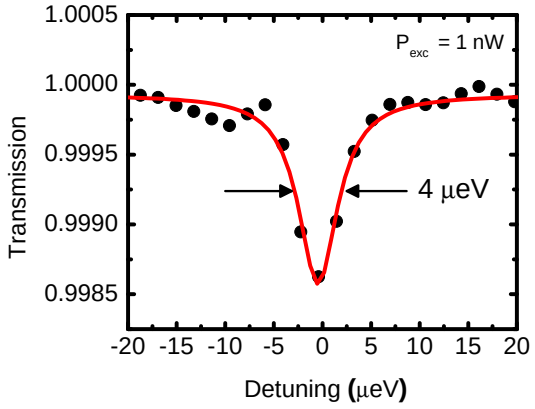

Figure 2.11: Transmission of an X^{1+} exciton (carbon doped) by Stark-shift modulation of the dot absorption. The red line is a Lorentzian fit.

A typical spectrum obtained in this way is shown in figure 2.11.

2.7.1 Charge-tunable sample

The quantum dot samples used in the absorption experiments are charge-tunable [66], effectively metal insulator semiconductor field-effect transistor (MISFET) devices. The sample structure allows control of the quantum dot energy via the Stark shift. A schematic of the sample structure is shown in figure 2.12 (a). The sample can be either n-doped or p-doped (p type is described here). The back contact region contains highly p-doped GaAs creating a reservoir of holes. It is separated from the quantum dot layer by a 25 nm thick tunnel barrier. The superlattice consists of layers of AlAs/GaAs and electrically isolates the back contact from the top gate. The NiCr gate is semi-transparent (only a few nm thick) and is evaporated on the top of the sample and acts as a Schottky gate. The device is essentially a capacitor structure, which allows a voltage to be applied between the NiCr gate and the back contact.

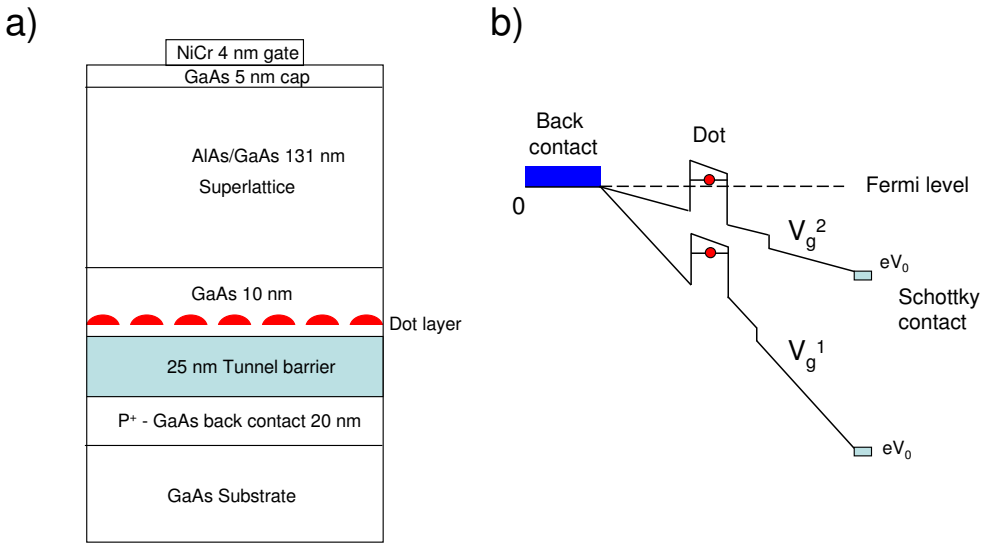

Figure 2.12: a) MBE grown heterostructure, containing InAs quantum dots in a charge-tunable device (sample MVC12-2). b) The lever arm effect, showing the applied bias, V_g^2, pulls the dot's valence s-shell level below the Fermi level.

Figure 2.12 (b) shows the lever arm principle used to charge the quantum dot with single holes. The principle is to vary the the dot energies relative to the constant

Fermi level by applying a voltage over the sample to shift the dot energies. When the first quantised level in the dot becomes resonant with the Fermi level, a hole is free to tunnel from the back contact into the dot. This allows the charge-tunable structure to charge single dots with single holes. The Coulomb blockade is crucial to this. Because the dots are small, the Coulomb force between carriers in the dots is large, preventing a second hole from entering the dot at the same gate voltage.

Chapter 3

A fully tunable microcavity

3.1 Introduction

This chapter describes the development of a new type of fully tunable microcavity. In Chapter 1 the three main types of existing state of the art microcavities were reviewed. The ultimate goal for a new cavity technology would be to combine the advantages of these existing devices, without any of their drawbacks. Such a device would ideally possess qualities including:

1) High Q-factor and low mode volume
2) Continuous wavelength tunability
3) Broad wavelength tuning range
4) Continuous spatial tunability
5) Operation at cryogenic temperatures

The technology developed in this work has these qualities. The key concept was to scale down a typical Fabry-Pérot cavity to microscopic dimensions, whilst maintaining tunability and a high Q-factor. A sketch of the cavity design is shown in figure 3.1. The top half of the cavity consists of a dielectric coated curved mirror, which is fixed in place. The curved mirror could confine the cavity mode laterally, minimising losses due to beam walk-off. This would allow a high Q and a low mode volume to be obtained.
The bottom half of the cavity is the semiconductor heterostructure discussed in chapter 2, section 2.5 (bottom DBR plus a λ layer of quantum dots). The semiconductor mirror could be brought to 1-2 μm from the top mirror by means of a piezo positioning system. A very small cavity (a few optical wavelengths) could be formed in this way, with the air gap and a z piezo positioner allowing the cavity resonance to be tuned by moving the bottom mirror in the z direction with respect to the fixed top mirror. This would enable a large tuning range with picometre control over the cavity length.

The cavity must be stable in the z direction to ensure that acoustic noise does not alter the cavity length by vibrating the mirrors. This was not easy to achieve due to the non-monolithic nature of the design.
Spatial tunability is achieved using an xy piezo positioner to move the bottom mirror with respect to the top one, allowing in situ spatial matching of an emitter to the cavity mode antinode.
Laser light can be coupled into the cavity via the confocal microscope set-up described in chapter 2. The reflected signal from the cavity can be collected by the microscope and the cavity transmission can be measured by a detector placed under the bottom mirror.

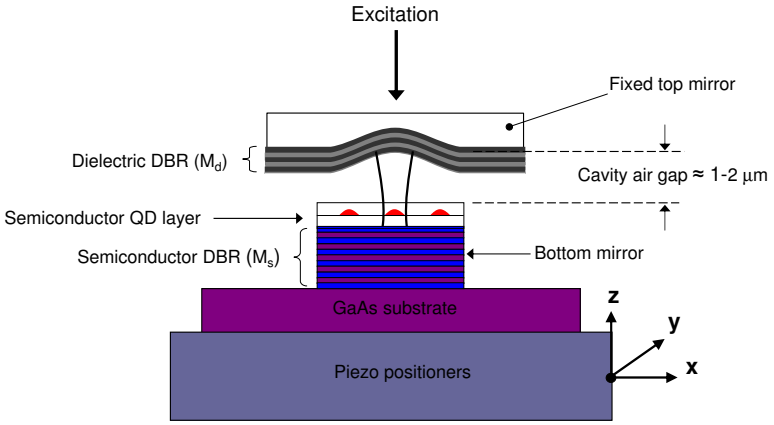

Figure 3.1: Tunable microcavity concept. The cavity mode is confined laterally by a miniature concave mirror. The two mirrors have a small adjustable air gap between them. The bottom mirror can be displaced in three dimensions relative to the top mirror by two piezo positioning stages.

3.2 Cavity design

3.2.1 DBRs

The two different DBRs used in this work are summarised in table 3.1. M_d and M_s denote the dielectric coated DBR and the semiconductor DBR respectively.

The two mirrors have different reflectivities and stop band widths, due to their specific materials and number of pairs. The width of the stop band, $\Delta\lambda_{sb}$ depends on the

	M_d	M_s
$\lambda_c(nm)$	950	950
materials	TiO_2/SiO_2	GaAs/AlGaAs
no. of pairs	10	32
R %	99.75 %	99.99 %
$\Delta\lambda_{sb}$ (nm)	275.04	92.92
n_H	2.25	3.5
n_L	1.45	3.004
n_{eff}	1.76	3.23
$L_{DBR}(physical)$	0.55 μm	1.56 μm
$L_{DBR}(optical)$	0.968 μm	5.03 μm

Table 3.1: A summary of the theoretically expected values for the parameters of the mirrors used in the cavity experiments. λ_c is the centre of the stopband.

difference in the refractive indices of the two materials, Δn, given by equation 1.16 (chapter 1).

It is clear that the larger the refractive index difference between the constituent materials within a DBR, the fewer pairs needed to obtain a target reflectivity and stop band width. Dielectric mirrors consist of two materials with larger refractive index differences and therefore require typically 2 - 3 times fewer pairs than a semiconductor DBR with a comparable maximum reflectivity.

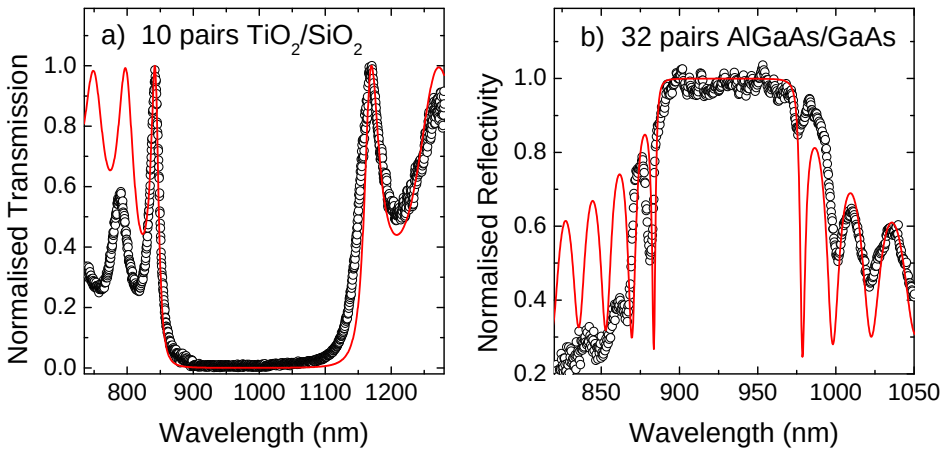

Figure 3.2: a) The normalised transmission spectrum for M_d measured at 300 K using a broad band white light source. b) The normalised reflection spectrum for M_s, measured at 77 K. The red lines indicate the simulated stop band spectrum (assuming λ independent refractive indices) for each plot, with a centre wavelength of 950 nm.

Figure 3.2 a) shows the measured transmission spectrum of M_d and b) the mea-

sured reflection spectrum of M_s. A white light broad band source was used to illuminate the mirrors and the spectra are corrected for the wavelength dependence of the source. Neither plot indicates an absolute reflectivity or transmission percentage, only the spectral properties of the DBRs. The red lines indicate the simulated spectra for each mirror, given the layer thicknesses and design wavelength. The measured stop band width of M_d is nearly a factor of 3 greater than M_s, which agrees well with the simulations. The observed oscillating side bands in the M_s spectrum deviate from the simulation due to the effect of the GaAs band gap at 1.507 eV (824.9 nm) at 77 K. The simulation neglects the effect of the band gap on the calculated spectrum.

3.2.2 Penetration lengths

When light is incident on a DBR, the reflected wave front will experience a time delay τ due to the DBR's distributed nature. This time delay can be interpreted as an apparent penetration into the mirror. The effect can be understood by considering a fixed-phase mirror which is a small distance, L_{DBR} away from a fixed reference plane, which denotes the surface of the equivalent DBR structure, see figure 3.3.

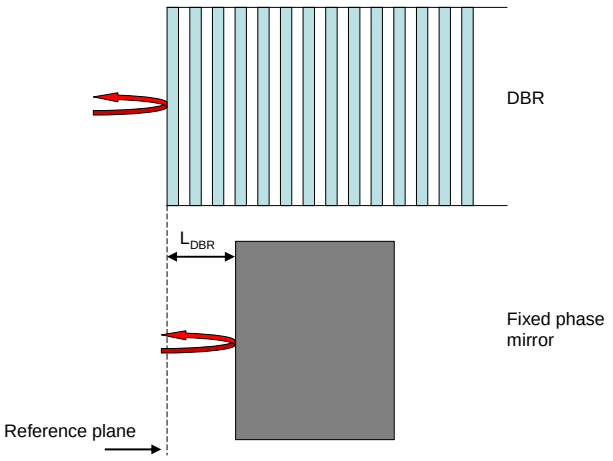

Figure 3.3: The concept of penetration depth into a DBR, by considering the equivalent situation of a fixed phase mirror placed a distance, L_{DBR}, from the reference plane.

$$L_{DBR} = \frac{c\tau}{2n_e} \tag{3.1}$$

where n_e is the external refractive index (in air $n_e = 1$) and the reflection delay, τ is given by :

$$\tau = \frac{\lambda_c}{2c}\frac{n_L n_H}{n_H - n_L}. \tag{3.2}$$

By substituting equation 3.2 into equation 3.1 it can be shown that,

$$L_{DBR} = \frac{\lambda_c}{4n_e}\frac{n_L n_H}{n_H - n_L} \tag{3.3}$$

The physical penetration into both mirrors in the tunable cavity can be calculated using equation 3.3. The dieletric mirror, M_d, therefore has $L_{DBR} = 0.55$ μm and the semiconductor mirror, M_s has $L_{DBR} = 1.56$ μm. Therefore the cavity length in the tunable cavity is not the air gap alone, but also includes the penetration into both mirrors. Combining the mirror penetration depths, the semiconductor layer and the air gap, a more realistic expression for the *effective* cavity length, L_{eff}, is obtained:

$$L_{eff} = L_{Md} + L_{air} + L_c + L_{Ms}, \tag{3.4}$$

where L_{Md} and L_{Ms} are the penetration lengths into the dielectric and semiconductor mirror, respectively, L_{air} is the length of the air gap and L_c is the length of the active semiconductor cavity layer.

3.2.3 Cavity electric field and tuning curves

The properties of the DBRs discussed above play a major role in the optical properties of the tunable microcavity. The tunable air gap and the incorporation of a dielectric top mirror makes the whole picture substantially more complicated than monolithic devices. The most crucial requirement is that the electric field antinode lies not in the air gap but at the location of the quantum dot layer. In this section a model of the tunable cavity is simulated, to illustrate the effect that the cavity mirror configuration has on the electric field at the dot layer.

The simulations rely on the standard transfer matrix method [67], to calculate the transmission, reflection and, for a fixed wavelength, the electric field profile in a particular cavity configuration. The notation used here is L (H) for the Lower (Higher) refractive index material facing the cavity region i.e the last layer coated on the dielectric mirror and the last layer grown before the GaAs dot region on the semiconductor mirror. Starting from the top dielectric mirror, the tunable cavity layer sequence can be written as L-A-S-L if both the DBRs finish on the low refractive index material, where A is the air gap and S the semiconductor cavity layer.

Figure 3.4 shows the different mirror configurations and corresponding simulated electric field profiles. For each simulation the dielectric mirror is on the left, followed

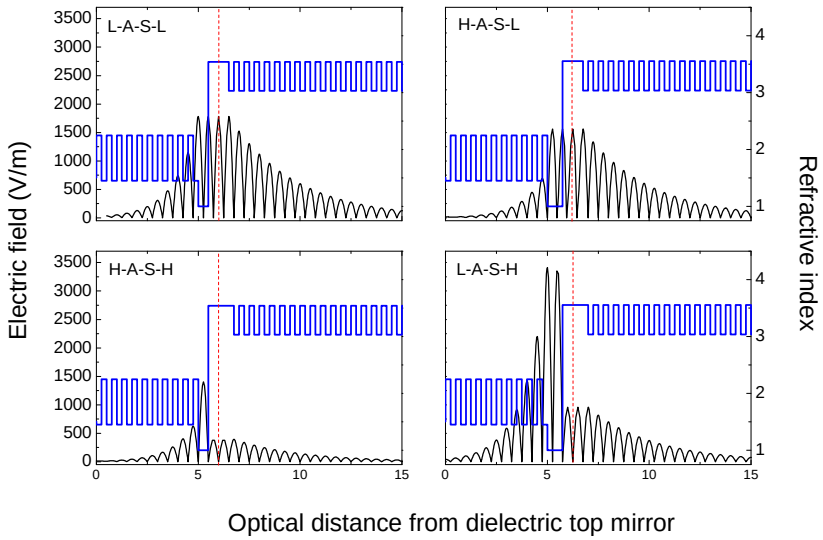

Figure 3.4: Electric field distributions for various cavity configurations. The L (H) stands for the lower (higher) refractive index material facing the cavity. A and S represent the air and semiconductor dot layers respectively. The dielectric mirror (10 pairs of TiO_2/SiO_2) is on the left, followed by a $\frac{\lambda}{2}$ air gap, a λ layer of dots (dotted red line) and finally the semiconductor mirror (32 pairs of AlGaAs/GaAs) on the right. The refractive index profile (blue line) is also shown superimposed on the electric field profiles.

by the air gap, the GaAs cavity layer with the dots in the centre and then finally the semiconductor DBR on the right. The simulations assume an input light intensity of 1 W/m^2 incident on the cavity on the dielectric mirror, with absorption ignored for simplicity. The refractive index profile of each cavity configuration is also shown superimposed on the electric field profiles in figure 3.4 (blue).

The refractive indices used in the simulation are summarised in table 3.1. An air gap of $\lambda/2$ is assumed for each mirror configuration, where the cavity is designed for emission at 950 nm. An electric field antinode must lie exactly on the quantum dot layer (red dotted line) in order for the cavity to interact strongly with the quantum dots. This criterion puts a constraint on the mirror configurations which can be used, limiting the choice to either the L-A-S-L (figure 3.4, top left) or H-A-S-L (figure 3.4, top right). The electric field intensity is maximised for the L-A-S-L configuration and while H-A-S-L does have a standing wave antinode over the dot layer, the amplitude of the electric field is slightly lower than the L-A-S-L configuration. H-A-S-H and L-A-S-H configurations are not suitable because they have a node over the dot layer (figure 3.4, bottom row).

3.3 Simulated cavity tuning plots

The relation between the change in cavity air gap thickness, Δz and the corresponding change in cavity wavelength, $\Delta\lambda$ depends on the top and bottom mirror configuration and the semiconductor layer thickness. Figure 3.5 shows the simulated tuning curves for the tunable cavity, with the same four mirror configurations considered in figure 3.4. The plots clearly show that the relation between Δz and $\Delta\lambda$ is nonlinear. It can be seen that the lowest gradient curves are obtained for the L-A-S-L and H-A-S-L configurations (figure 3.5, top row). The shallow gradient is ideal for minimising the influence that noise (small vibrations in the vertical direction) has on the emission wavelength. In these configurations, the bottom mirror must be displaced by a greater distance to achieve a similar tuning range as the H-A-S-H and L-A-S-H configurations, but the protection against acoustic noise more than compensates for this. This is particularly important when considering a cavity designed for high Q-factors (such as the one realised in section 3.9.2), as noise can detrimentally broaden the mode linewidth. In the case of the tunable cavity described here, the tuning range is not affected by the lower gradient curves because the bottom mirror can be moved over relatively large distances (3 mm).

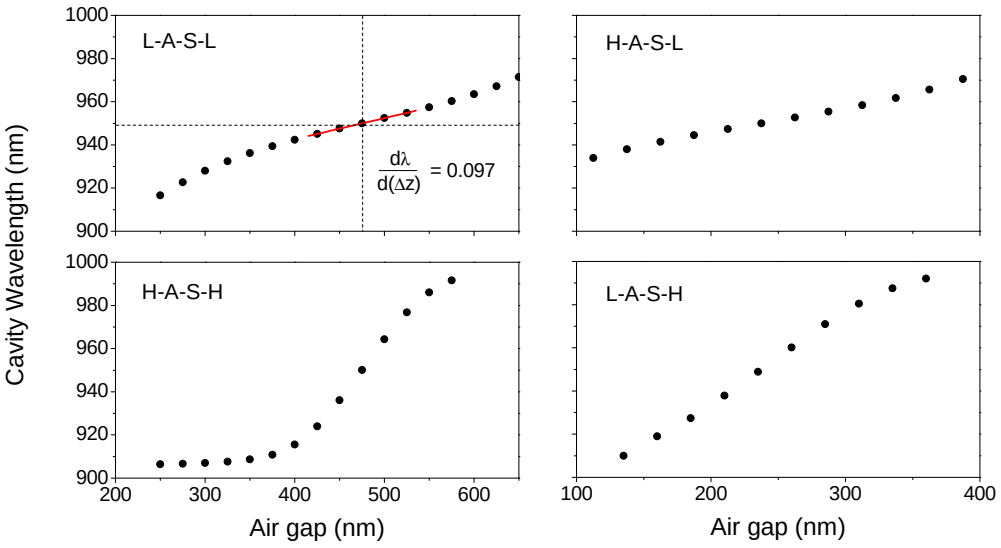

Figure 3.5: The simulated tuning curves (cavity resonant wavelength versus air gap) for the same cavity mirror configurations as figure 3.4. The DBR stopband for both mirrors is centered at 950 nm.

The L-A-S-L approach therefore offers the best combination of electric field antinode position and a large tuning range that minimises the cavity's susceptibility to

noise.

3.4 Device realisation and experimental set-up

The desirable qualities discussed in section 3.1 require a mechanical arrangement which has a rigid housing to limit the effect of noise. A piezo positioner alters the cavity length in the vertical direction (z) to tune the cavity wavelength. A scanning piezo unit positions the bottom mirror in the xy plane, providing spatial tunability. The experimental set-up for a fully tunable microcavity is shown in figure 3.6. The apparatus consists of an assembly of piezo motors supplied by Attocube Ltd of Germany, inside a rigid housing. The compact nature of these piezo positioners was a key factor in allowing sufficient space to incorporate a solid housing around the positioners, vital to protecting the cavity against vibrations. The base unit comprises three ANPxyz100 piezo motors designated XYZ positioners in the figure. The cavity unit includes one ANSxy50 (xy scanner) and one ANPz30 positioner designated xy piezo and z piezo respectively.

The housing which supports the piezo positioners and cavity is made from titanium.

Base

The cavity unit is mounted on a base of the larger XYZ positioners, which can move the entire cavity unit in all three dimensions with respect to the focus (Figure 3.6). Each of these positioners has a travel of 6 mm, thus providing macro control of the cavity unit location in X, Y and Z directions.

Cavity unit

Isolating the cavity from mechanical noise was a key consideration during the design of the cavity housing. Being a non-monolithic device, the cavity mirrors might suffer from noise-induced relative longitudinal movements. Any longitudinal vibration would result in an undesirable change in cavity wavelength. Mechanical noise typically occurs at low frequencies around 100 Hz. To ensure minimal response to mechanical noise, the cavity was designed to have a high resonant frequency $\geq$ 10 kHz by making the housing as rigid as possible. The xy scanner and z positioner have calculated resonant frequencies of 10 kHz and 30 kHz (calculated by Attocube), therefore they should not respond to low frequency noise. The xy piezo is a scanner type positioner. A voltage of up to 70 V can be applied at 300 K and up to 150 V at 4 K. The scanner

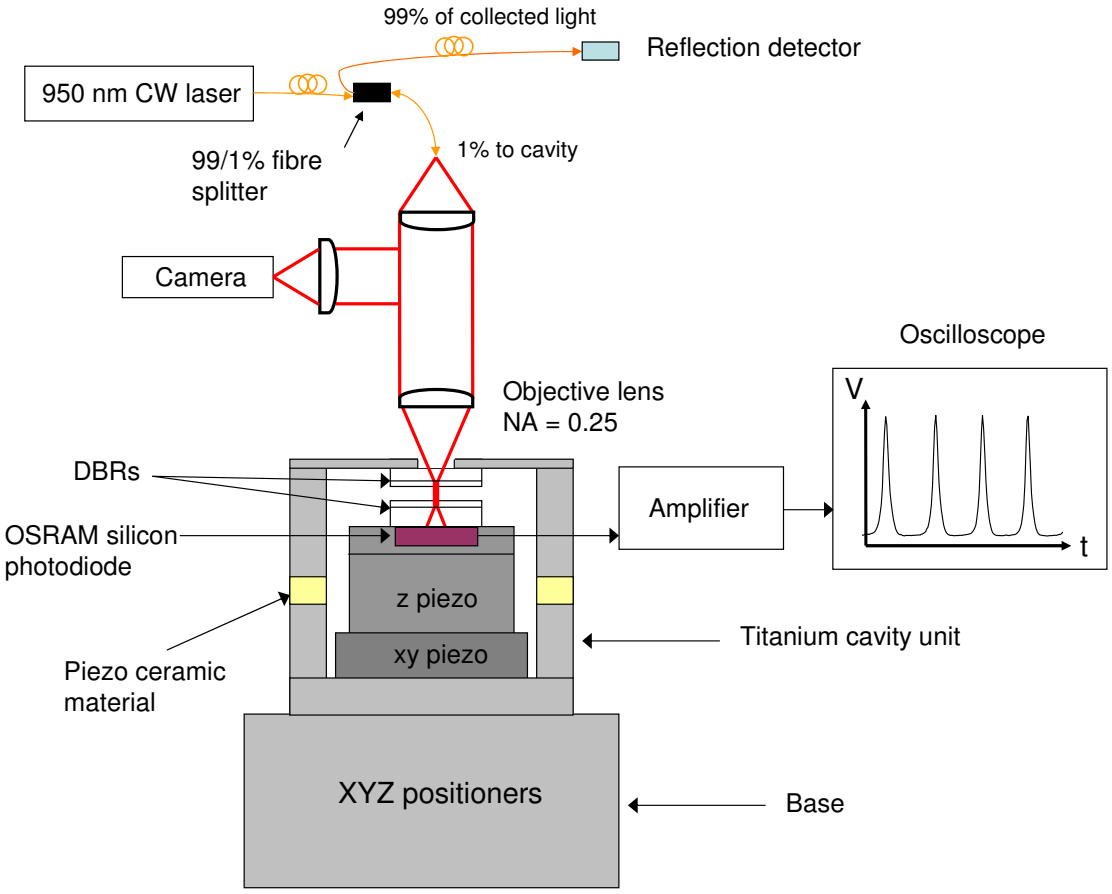

Figure 3.6: Schematic of the experimental set-up for cavity transmission or reflectivity experiments. The cavity is probed using the confocal microscope described in chapter 2. The cavity is positioned relative to the objective lens using an XYZ piezo positioning system. The cavity signal can be recorded either in transmission on a photodiode or in reflection on a photodiode via a 99/1% Font Canada fibre splitter. The z piezo which controls the cavity air gap can be adjusted in nm steps or swept with picometre resolution over 4.5 μm at 300 K and 700 nm at 4 K. By applying a triangular voltage signal to the piezo, the cavity length can be dithered to observe the modes in real time.

has a maximum fine positioning range of 20 $\times$ 20 μm at 300 K and 12 $\times$ 12 μm at 4 K. Subnanometre resolution can be achieved thus providing precise location in the xy plane.

The z piezo positioner operates in two modes and provides the extremely accurate positioning required for cavity length control. The z piezo is the smallest piezo positioner Attocube currently manufacture and it is extremely compact and stable. It is securely screwed to the top plate of the xy piezo positioner, forming a compact stack capable of moving a mirror placed on top, in all three dimensions with unprecedented precision. The piezos and mirrors are fixed inside the titantium housing, which min-

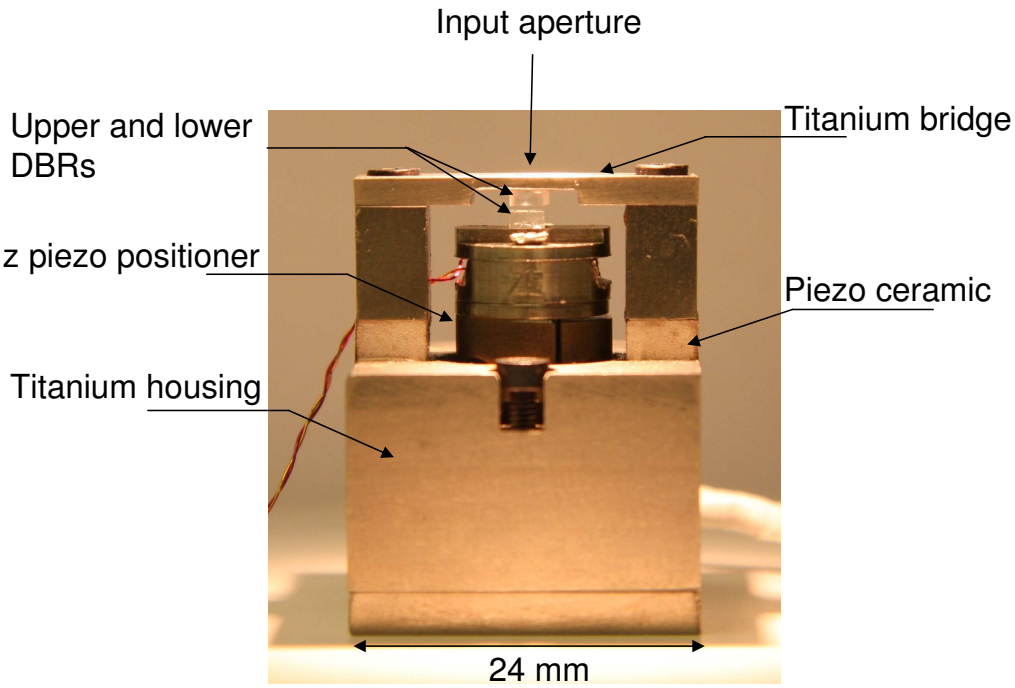

Figure 3.7: A photograph of the tunable cavity unit. The top of the z piezo positioner is visible, with the wires from mounted transmission detector and cavity mirrors. The xy scanner is hidden within the titantium housing.

imises any relative movement between the two mirrors from vibrations. The resulting system is both compact and stable and can be incorporated into the existing confocal microscope system described in chapter 2. The photograph in figure 3.7 shows the actual cavity unit.

The same microscope arrangement used for free space PL collection (described in chapter 2) is used to probe the cavity. The bottom mirror is glued to a titantium disk which screws directly onto the top of the z piezo positioner which alters the cavity length, and has a hole in the centre to allow transmitted light to be collected on the OSRAM silicon photodiode (active area of 2.65 mm x 2.65 mm) for transmission experiments.

The piezo positioners are also made from titanium, therefore when the cavity is cooled to cryogenic temperature, there should be very little difference in thermal contraction between the motors and the housing, thus minimising the chance of the cavity air gap changing significantly during cool down. To ensure that this is the case, two pieces of piezo ceramic material of exactly the same thickness and type used in the z piezo positioner and xy piezo positioner are included in the housing.

Cavity length control

The z piezo positioner used to vary the cavity length was chosen for its extremely small size and large range of travel with picometre stepsize capability. The positioner can be operated in two modes. Stepping mode allows for 3 mm of course travel, and according to the manufacturer the minimum step size possible in this mode is 25 nm at 300 K and 5 nm at 4 K. Applying $0 - 150\ V_{dc}$ (using the Attocube ANC200 piezo scan controller) across the piezo operates it in scanning mode for fine positioning. The range of travel is much reduced, typically only 4.5 μm at 300 K and 0.7 μm at 4 K. Scanning mode does however allow for very precise positioning (picometre resolution) and this allows exact spectral tuning of the cavity resonance. The incorporation of this precision positioner is a key factor in the experimental work which follows (chapter 4).

3.5 Scanner calibration

One axis of the ANSxy50 was calibrated at 4 K by John O'Connor (PhD student) to verify the manufacturer's estimate that 12.5 V applied to the piezo lengthens it by 1 μm. The test was conducted using a superconducting detector [68], mounted on top of the ANSxy50. The nanowire is arranged in parallel lines such that each section is 1 μm from its neighbours on either side. A diffraction limited laser spot size of 444.36 nm at a wavelength of 470 nm was focussed on to the first strand of the nanowire. A voltage of 120 V was applied to the Y scanner axis in steps of 0.6 V, with the superconducting detector registering counts when the laser spot was incident on a strand of the nanowire.

Figure 3.8 (a) shows the recorded detector counts per second as a function of applied voltage to the y scanner axis. The peaks indicate the spot was exactly on the centre of a strand superconducting nanowire. The drop in detector signal around 100 V is attributed to a damaged wire. The strands are known to be separated by 1 μm, therefore the voltage-length characteristics of the axis can be extracted from the data in figure 3.8 (a). Figure 3.8 (b) shows the peak values from (a) plotted as a function of the voltage applied to the piezo. The red line is the linear behaviour from the manufacturer's datasheet. At low voltages (0 - 50 V) the piezo behaves linearly, following the predicted behaviour well. However at higher voltages (60 - 120 V) the piezo behaviour appears to be slightly non-linear, with less voltage required to move the same distance. This non-linear behaviour is significant, however its effect on the data reported here was minimised by operating the piezo at voltages under 70 V.

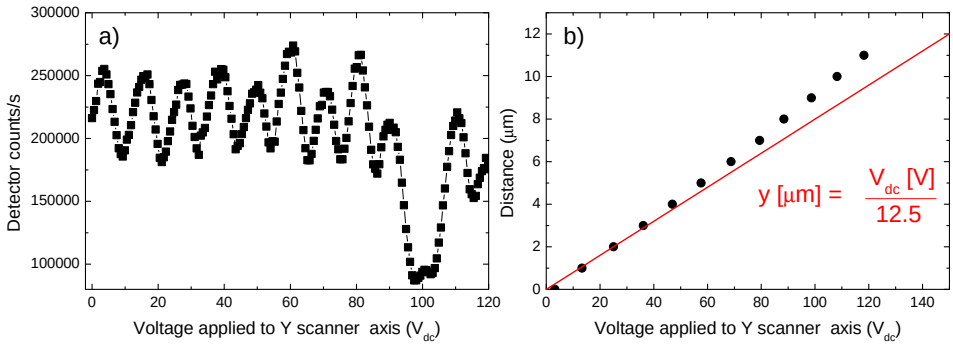

Figure 3.8: a) Counts on the superconducting detector at 4 K versus applied voltage to the Y axis of the ANSxy50. Counts register on the detector as the 444.36 nm laser spot is incident on a nanowire. b) A calibration plot of the Y axis of the ANSxy50 scanner. The data points are extracted from the peaks on the detector in (a). The red line is the theoretical voltage-distance characteristics from the manufacturer's datasheet.

3.6 A length-tunable planar microcavity

A fixed wavelength transmission experiment was performed to characterise a planar cavity in terms of finesse. Establishing a simpler planar microcavity allowed the construction techniques to be perfected without the added complications of a curved top mirror. A schematic of the planar cavity is shown in figure 3.9.

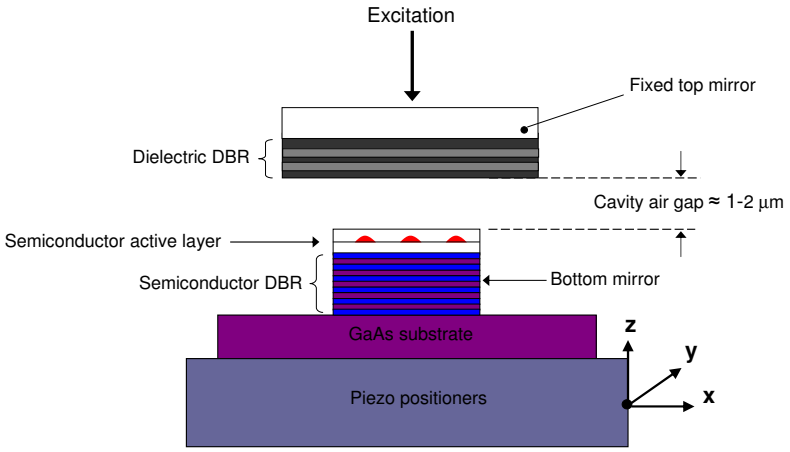

Figure 3.9: The planar microcavity with top mirror M_d and bottom mirror M_s.

A high degree of mirror parallelism is crucial to achieving the smallest possible cavity length. In a planar cavity it is also vital to limit the beam from 'walking out' of the cavity and introducing large losses. A procedure was developed for minimising any skew between the top and bottom mirrors. Firstly, the bottom semiconductor mirror was rigourously cleaned using the procedure described in chapter 2, section 2.6. The mirror was then glued in place on the titantium sample holder using Oxford GE varnish and left to allow the varnish to dry fully. The top dielectric mirror was then cleaned in a similar fashion and laid to rest on top of the bottom mirror, with the dielectric coated surface in contact with the semiconductor surface. A small amount of varnish was placed on the cavity bridge above the back of the top mirror. The z piezo positioner which controls the cavity length was pushed up until the back of the top mirror is touching the varnish. The cavity was left to dry in this position. A schematic of this procedure can be seen in figure 3.10.

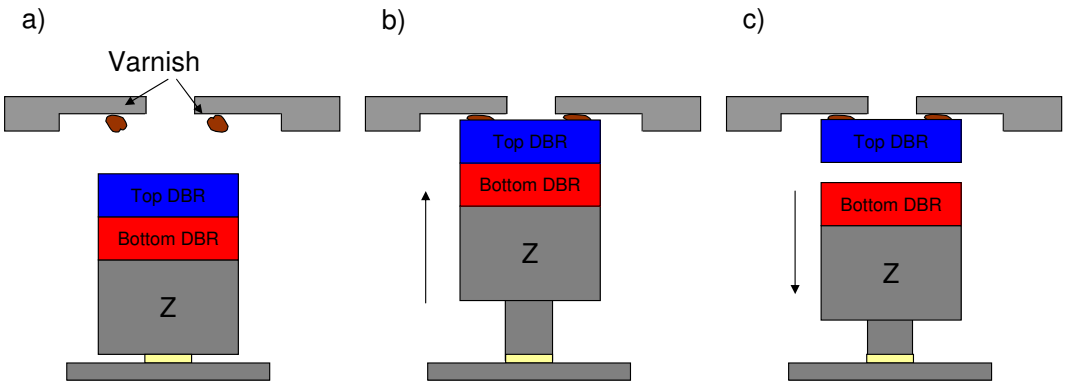

Figure 3.10: A schematic diagram showing the mirror mounting procedure. a) A small amount of Oxford GE varnish was applied to the upper mirror holder. The top DBR was placed on top of the bottom DBR. b) The cavity piezo positioner was extended, pushing the top mirror upwards into the varnish. The cavity was left to dry for 2 hrs in this position. c) The finished cavity.

Once this procedure has been performed, the minimum cavity air gap is limited only by any contaminants such as dust particles that become trapped between the two mirrors. Therefore it is crucial that the utmost care is taken to ensure the mirrors

remain clean. The cavity air gap is at its absolute minimum and is increased by pulling down the z piezo positioner just a few nanometers until the desired cavity length is achieved.

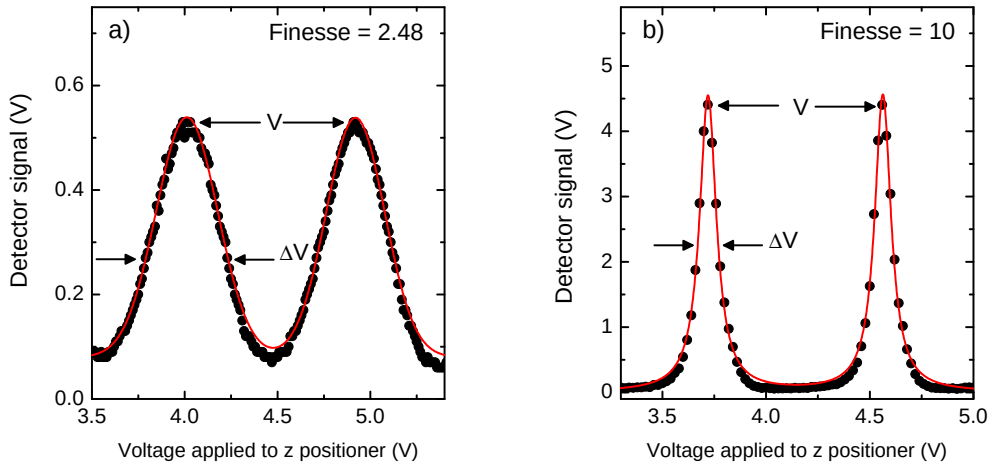

Figure 3.11: a) Cavity modes from a planar/planar cavity without utilising the parallelism technique, F = 2.48 (red line is a fit using the Fabry-Pérot cavity equation). b) The finesse increased to 10 when the parallelism technique was employed (red line is two Lorentzian fits). The cavity was probed with a 950 nm laser at 300 K.

The planar cavity finesse was measured by focusing a 950 nm CW laser onto the back of the top dielectric mirror (R = 99.8%) and applying a voltage to the z piezo positioner to alter the cavity length. The voltage applied to the positioner was modulated by a voltage signal generator, allowing a 10 V peak to peak triangular waveform at a frequency of 20 Hz to be applied to dither the cavity length over a small distance, ΔL = 300 nm. The cavity signal was recorded in transmission utilising a detector below the bottom semiconductor mirror and in reflection utilising a Font Canada 99/1% fibre splitter. For transmission measurements, 100% of the coupled laser light was directed to the cavity to maximise the signal to noise ratio. In reflection only 1% was directed to the cavity, allowing 99% of the reflected signal to be collected (via the fibre splitter) by the detector. The signal from the detector was then amplified and displayed on one channel of an oscilloscope. This technique allowed the cavity modes to be viewed in real time, allowing the optics to be aligned to maximise the cavity mode's intensity. Once the cavity was aligned with the dithering technique, the finesse was measured by recording the cavity transmission signal as a function of the voltage applied to the z piezo positioner.

Figure 3.11 shows the transmission signal versus the cavity piezo voltage for two

different planar microcavities. Both cavities have a minimal air gap and use identical mirrors (M_d and M_s). The cavity length is inversely proportional to the applied voltage. Both cavities' transmission spectra show two adjacent longitudinal modes. The data in (a) is fitted using the equation for a Fabry-Pérot cavity [36]. The data in (b) has 2 fully resolvable peaks and is fitted with Lorentzian lineshapes (red lines). The two modes in (a) are much broader than in (b) due to a lack of parallelism between the mirrors. Cavity (a) has not been subject to the mirror parallelism technique, whilst cavity (b) formation included the parallelism technique. The equation for a Fabry-Pérot cavity [36] is used to fit the data in figure 3.11 (a). The fit uses the value of the finesse F as a free parameter and the best fit is obtained using F = 2.48. The finesse in figure 3.11 (b) has increased to 10, due to a better degree of parallelism between the mirrors. The fixed wavelength transmission technique gives no indication of absolute cavity length, therefore an optical microscope was used to examine the cavity air gap, which was found to be smaller than the resolution of the microscope, giving an estimate of $L_{air} < 10$ μm.

3.6.1 Planar cavity finesse and losses

The z piezo positioner allows the cavity length to be scanned to observe several adjacent longitudinal modes at room temperature. A planar cavity was established and the cavity length decreased by about 2.4 μm by applying 80 V to the z piezo positioner in steps of 0.25 V and recording the cavity transmission on the detector. Figure 3.12 shows the transmission signal from the cavity as a function of the voltage applied to the z piezo positioner. The data shows six adjacent cavity modes with a similar finesse to that shown in figure 3.11 (b).

The maximum reflectivity of M_d is calculated to be R = 99.95% at 950 nm. However this neglects absorption and scattering losses in the mirror. The coating company (O. I. B. Jena GmbH) estimates that the combined scattering and absorption losses could be as high as 2000 ppm, which lowers the actual maximum mirror reflectivity to R = 99.75%. The bottom mirror, M_s, has an estimated minimum reflectivity of R = 99.99%. Using equation 1.20, the calculated maximum finesse (limited by the mirror reflectivities) for such a cavity is, $F = 1568$.

The finesse measured experimentally from the planar cavity formed with these mirrors is in the range $10 < F < 30$. This large discrepancy is due to the lack of parallelism between the two mirrors. However even with perfectly parallel mirrors the finesse is limited by diffraction.

An alternative microcavity design has been developed to maximise the finesse and minimise the mode volume to allow the interaction of the optical cavity mode with a

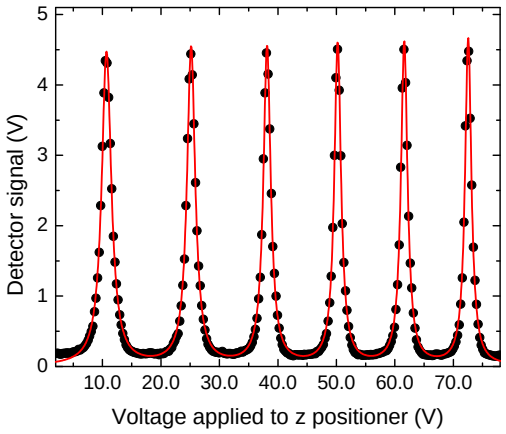

Figure 3.12: Transmission spectra for a planar-planar cavity geometry, demonstrating a large tuning range. The cavity was probed with a 950 nm laser at 300 K. The cavity length changes by $\lambda/2$ between adjacent modes.

single quantum dot, whilst maintaining tunability. This is the subject of the following section.

3.7 Curved mirror cavity

3.7.1 Introduction

In section 3.6.1 the finesse of a planar/planar microcavity was shown to be much less than the theoretically predicted value. The dominant loss mechanism for poorly aligned mirrors is beam walk-off. For well aligned mirrors the maximum finesse reaches a fundamental limit, dictated by diffraction and not the mirror reflectivity. However, even for well aligned mirrors the lack of lateral confinement of the optical mode in the xy plane allows the mode to expand. The mode volume in the planar cavity is therefore too large for the cavity to realistically be considered for quantum dot/cavity experiments, even if a high finesse is achieved. An elegant solution is to confine the beam laterally by utilising a half symmetric cavity design. The curved mirror eliminates beam walk-off by directing any escaping beams back in towards the centre.

3.7.2 Half symmetric cavity

Standard Gaussian beam theory in resonators predicts that in a half symmetric cavity a minimum beam waist ω_0 occurs at the planar mirror, with the beam diameter

increasing monotonically towards the curved mirror, figure 3.13. The maximum beam waist ω_1 occurs at the curved mirror. Both ω_0 and ω_1 are 1/e values.

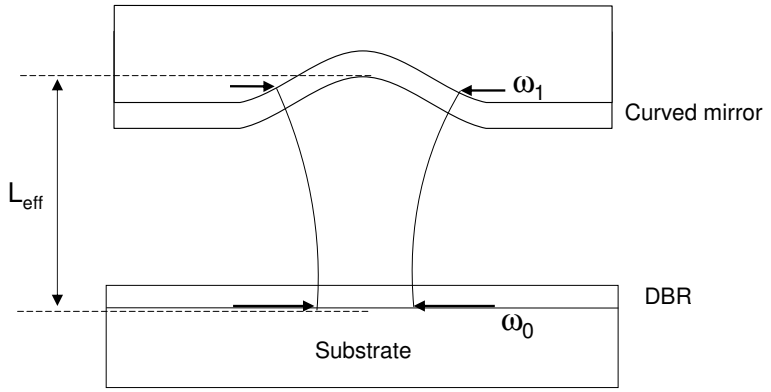

Figure 3.13: A schematic diagram of the half symmetric cavity. The Gaussian beam in the cavity is shown, indicating the beam beam waists at the curved (ω_1) and planar mirror (ω_0).

The beam waists at the mirrors depend on the effective cavity length, L_{eff} and the radius of curvature of the top mirror, R. The beam waists are defined [36],

$$\omega_1 = \left(\frac{\lambda R}{\pi}\right)^{\frac{1}{2}} \left(\frac{R}{L_{eff}} - 1\right)^{-\frac{1}{4}} \tag{3.5}$$

$$\omega_0 = \left(\frac{\lambda}{\pi}\right)^{\frac{1}{2}} (L_{eff}R - L_{eff}^2)^{\frac{1}{4}} \tag{3.6}$$

where ω_1 is the beam waist at the curved mirror, ω_0 the beam waist on the planar mirror and R is the radius of curvature of the curved mirror. It is worth noting that ω_0 increases as $R^{\frac{1}{4}}$ and therefore even a relatively large mirror curvature does not cause a large detrimental effect in maintaining a small mode volume. Figure 3.14 shows the simulated beam waists versus cavity length, for a curved mirror with a radius of curvature R of 100 μm. Figure 3.14 shows that for short cavity lengths (L $\leq$ 10 μm) there is negligible divergence of the beam over the cavity length ($\omega_0 \approx \omega_1$). Both beam waists increase monotonically with increasing cavity length, when L = R the curved mirror beam waist expands rapidly as the cavity becomes unstable. The cavity will only be stable if:

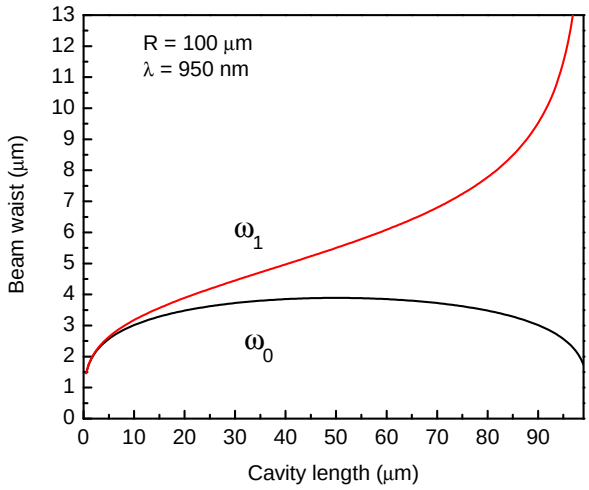

Figure 3.14: Fundamental Gaussian mode beam waist at the curved mirror (red) and the planar mirror (black) versus cavity length.

$$0 \leq g_1 g_2 \leq 1 \tag{3.7}$$

where the cavity stability parameters g_1 and g_2 are given by

$$g_1 = g \equiv 1 - \frac{L}{R_1} \quad , \quad g_2 \equiv 1 - \frac{L}{R_2} = 1, \tag{3.8}$$

where R_1 is the radius of curvature of the curved mirror and R_2 is the curvature of the planar mirror, therefore $R_2 \to \infty$ here.

The stability diagram for optical resonators is shown in figure 3.15. The diagram classifies different cavity geometries in terms of g_1 and g_2. For a half symmetric cavity for very short cavities, the configuration is classified as almost planar ($g_1 \to 1$) because the beam waist is very small compared to the mirror's lateral dimensions.

Assuming a fixed radius of curvature, as the cavity length is increased the geometry gradually changes, eventually reaching the hemispherical case where the cavity length equals the mirror curvature ($g_1 = 0$, $g_2 = 1$). If the cavity length is increased any further then the cavity becomes unstable.

The eigenfrequencies for a resonator are given by:

$$\upsilon_{qmn} = \frac{c}{2n_{cav}L}\left(q + (m+n+1)\frac{\cos^{-1}(\pm\sqrt{g_1 g_2})}{\pi}\right) \tag{3.9}$$

where q is the longitudinal mode index,m and n are the transverse Gaussian mode

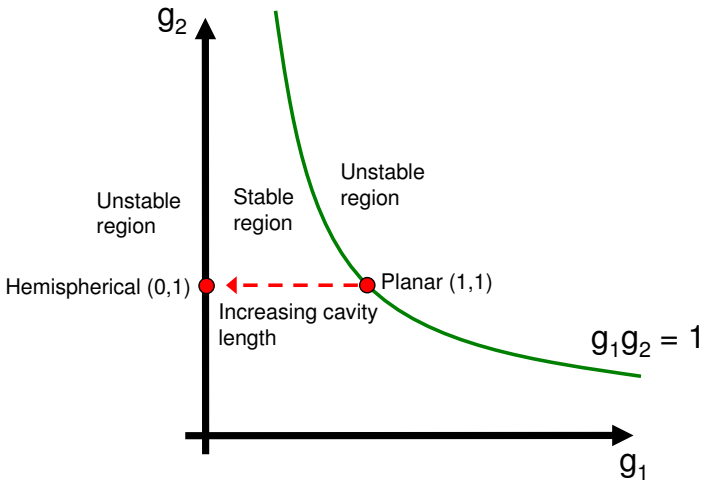

Figure 3.15: Resonator stability diagram showing the change in resonator type from planar cavity (i.e. $L \ll R$) to hemispherical ($L = R$), with increasing cavity length. If the cavity length is increased beyond $L = R$, the cavity becomes unstable.

indices and n_{cav} is the cavity refractive index. For the half symmetric cavity geometry in this work, $g_2 = 1$ due to the infinite curvature of the flat mirror. A set of transverse modes Δv_T is associated with each longitudinal mode in the cavity. The spacing between transverse modes for any given longitudinal mode is given by:

$$\Delta v_T = \frac{c}{2n_{cav}L}\frac{\cos^{-1}(\pm\sqrt{g_1})}{\pi}(\Delta m + \Delta n) \tag{3.10}$$

where Δm and Δn are the difference in mode indices between the fundamental mode and and transverse modes.

3.8 A microscopic concave mirror

High quality mirrors are produced by ablating an array of craters in a fused silica substrate which is then coated with a high reflectivity dielectric coating.

3.8.1 Laser ablation

The microscopic curved mirrors developed for the cavity experiments described here were fabricated by a process called laser ablation [69, 70]. Laser ablation is the controlled melting of a thin surface layer of a substrate using a CO_2 laser pulse. The

profile of the laser beam is transfered into the surface of the substrate. Fused silica is a good candidate for laser ablation by a CO_2 ($\lambda = 10.6$ μm) laser pulse due to strong absorption in silica in the 8-11 μm band. The penetration depth of the laser into a fused silica surface is about 30 μm [69], limiting the heating effect to a thin layer. During the ablation process the surface reaches a temperature of 1600 °C and a thin layer melts and evaporates. The remaining molten surface is mobile. Surface tension pulls the surface into a smooth, shallow Gaussian shaped crater before the silica cools.

A commercial company (Power Photonic Ltd) fabricated the ablated silica samples used as mirror templates in this work. The company used a CO_2 slab waveguide laser made by Lumonics (model 0630-920-00) to do the ablation. The laser has a high beam quality, $M^2 < 1.2$ and is capable of pulse repetition frequencies upto 10 kHz with a peak power per pulse of 100 W. The CO_2 laser pulses have an inherently triangular temporal profile and duration of 100 μs. The raw pulses from the laser are chopped using an acousto-optical modulator (AOM) to produce pulse durations that can be varied from 10-100 μs. The AOM also alters the temporal pulse shape from triangular to a quasi-square profile. The beam is focussed onto the sample using a lens of focal length 3.81 mm. The sample is mounted on an XY translation stage. A minimum spot size ($1/e^2$) of 45 μm at the sample surface is achieved.

An array of 11 × 15 craters was machined on the surface of a fused silica microscope slide. Fifteen craters were ablated by each of the 11 different laser pulse durations (66 - 100 μs) to form a 11×15 array of craters at 200 μm spacing. The spot size at the sample surface was varied from 45 μm - 100 μm by varying the position of the sample relative to the focal point. The irradiance at the surface of was kept constant at 0.3 MW cm^{-2}.

Figure 3.16 (a) shows an optical microscope image of a single crater. This crater was ablated using a $1/e^2$ spot size of 45 μm, axial fluence of 25 J cm^{-2} and a pulse duration of 70 μs. Figure 3.16 (b) shows the surface profile through the centre of a crater, fabricated using the same laser settings as in (a). The profile was obtained using a Dektak stylus surface profiler. The Dektak has a large range (several millimetres) and can therefore measure multiple craters in one long scan. The Dektak profile in figure 3.16 shows a typical Gaussian shaped crater which is 500 nm deep and has a $1/e^2$ value of 28.5 μm. The craters measured $1/e^2$ value is 63.33% of the ablating lasers $1/e^2$ value. The crater profile in figure 3.16 (b) was fitted close to the centre with the equation of a circle (red line). The radius of curvature was calculated from the best fit to be 120 μm. The radii of curvature were measured in the same way for 30 other craters on the sample. The values ranged from 80-150 μm, with the craters created with a 45 μm spot size having the smallest radii of curvature.

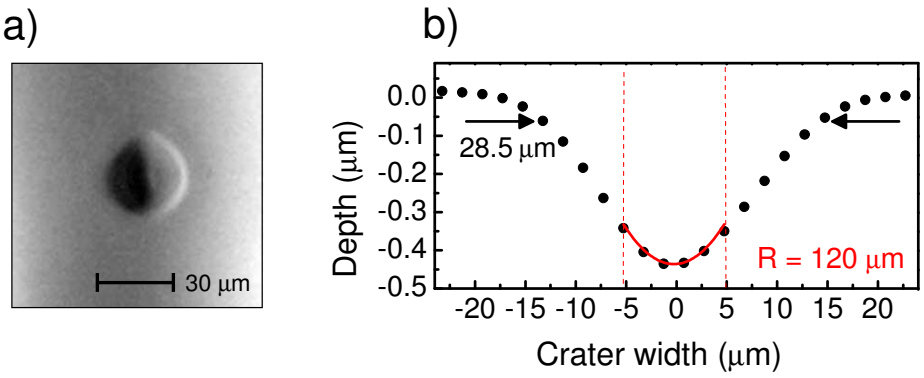

Figure 3.16: a) An optical microscope image of a laser ablated crater. b) A Surface profile measurement of the ultra-smooth, laser machined crater. The Gaussian profile has a $1/e^2$ value of 28.5 μm and is fitted (red line) at the centre (± 5 μm) with the equation of a circle, giving a radius of curvature, R = 120 μm.

3.8.2 Atomic force microscope measurements

The Dektak's resolution in the vertical direction is only about 10 nm, limiting its usefulness for measuring the crater's optical surface quality. A Digital Instruments (Dimension 3100) atomic force microscope (AFM) was used to examine the surface quality of the ablated craters before being optically coated. A smooth surface prior to coating is vital to obtain a high Q-factor microcavity. The AFM is ideal for measuring small surface areas with extremely high resolution. The AFM tip is scanned over 5 - 50 μm^2 areas in tapping mode and the AFM software can be used to perform a section analysis to extract such information as surface roughness, height change and feature size. Figure 3.17 (a) shows a section through the centre of a crater.

The area that an optical mode would occupy (indicated by the red lines) is the most important area in the crater; it is vital that it is smooth and symmetrical with a low surface roughness. Figure 3.17 (b) shows a much higher resolution section through the area at the centre of the crater, ± 1 μm either side of the crater centre. The AFM software determines a value for the root mean square surface roughness, R_{rms}, at the bottom of the crater by filtering the roughness profile from the raw profile and

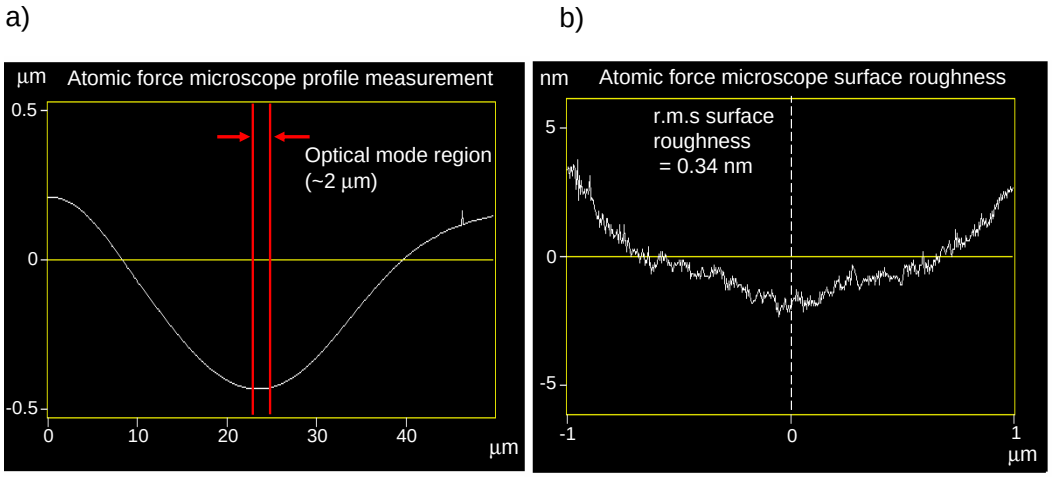

Figure 3.17: a) A crater profile measured using an AFM in tapping mode. The two red lines are spaced by 2 μm and indicate the region which an optical mode would occupy. b) A high resolution AFM scan of the area in (a) between the two red lines, showing the smooth surface on a nanometre scale.

evaluating,

$$R_{rms} = \sqrt{\frac{1}{n}\sum_{i=1}^{n}(y_i)^2} \tag{3.11}$$

where n is the number of data points in the roughness profile and y_i is the vertical distance from the mean line to the ith data point. The root mean square surface roughness value for the data in figure 3.17 (b) was calculated by the software to be, $R_{rms} = 0.34$ nm.

However none of the surface features in 3.17 (b) were reproducible in subsequent scans of the same area. This suggests that the measured surface roughness of 0.34 nm is actually just noise in the AFM. The actual surface roughness is therefore less then 0.34 nm.

3.9 Half symmetric cavity characterisation

To investigate the effect a curved mirror would have on the cavity finesse, an array of laser ablated craters were coated with 100 nm of silver using a thermal evaporation chamber. This opaque sample was used as the bottom mirror of the cavity, and the cavity completed with the planar dielectric coated mirror, M_d. A schematic of the configuration is shown in figure 3.18.

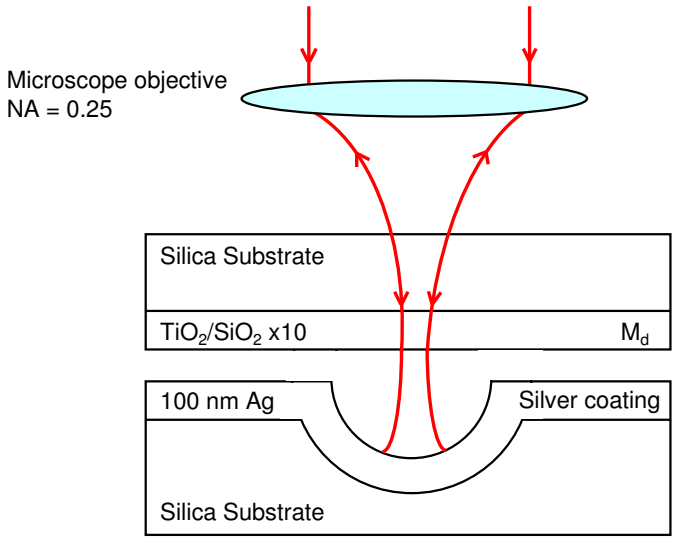

Figure 3.18: The half symmetric cavity. The curved silver coated mirror forms the bottom mirror of the cavity. A highly reflecting planar dielectric mirror (M_d) completes the cavity. The objective lens has an NA = 0.25 to match the focussed laser beam's waist to the cavity mode's beam waist at the planar mirror.

The cavity signal was measured in reflection using the Font Canada 2×2 fibre splitter. A microscope objective lens with an NA = 0.25 was used to focus the 950 nm laser beam into the cavity. This lens was chosen specifically to match the focussed input beam waist to the cavity mode diameter, as predicted by equation 3.6. The radius of curvature of the curved mirror was measured in section 3.8.1 to be 120 μm. At an effective cavity length of 10 μm the beam waist at the planar mirror is $\omega_0 =$ 2.9 μm. A diffraction limited beam waist from the chosen lens at 950 nm is 2.77 μm. Thus a reasonable match between cavity mode beam waist and the illuminating laser was obtained.

To probe the cavity, the laser spot was focussed onto the back of the dielectric coating. There is a large degree of tolerance in the vertical focal position for short cavity lengths, due to the depth of focus of the lens which is inversely proportional to its $(NA)^2$, more specifically:

$$\text{Depth of focus} = \frac{1.77\lambda}{(NA)^2} = 25\ \mu m, \tag{3.12}$$

therefore in the limit that the cavity air gap is less than 25 μm, the spot can be focussed either on the top or bottom mirror in the cavity.

Locating one of the curved mirrors and aligning the laser spot in its exact centre was very challenging. The dithering technique described in section 3.6 was used to monitor the reflected signal from the cavity (at room temperature) in real time on the oscilloscope. This technique proved essential for aligning the centre of the laser spot with the centre of a curved mirror. The process used for locating a curved mirror was initially to align on a planar cavity section (the coated areas between curved mirrors) using the dithering technique. The measured finesse from the planar cavity was 15. To locate a curved mirror, the entire cavity unit was translated in the xy plane with the XYZ piezo positioners, whilst monitoring the cavity reflection signal on the oscilloscope. As the laser spot was moved over the curved mirror, the cavity reflection signal showed a dramatic and continuous transformation from a broad single mode to a series of much narrower, more intense lines.

To scan across a curved mirror with the laser beam, the X piezo positioner was used to translate the cavity unit in 1 μm steps with respect to the focussed laser spot. The cavity reflection spectra versus change in cavity length, Δz was recorded at each X position. Figure 3.19 shows data taken at various detunings from the centre of the curved mirror in the X direction. Y was previously scanned in a similar fashion and positioned at the point (δy = 0) where the longitudinal mode was maximised (the centre of the curved mirror).

At a lateral detuning of $\delta x = 11$ μm from the centre of the crater (a) the observed reflection signal shows a planar cavity mode which has a slightly asymmetric profile. The finesse of the mode is 15. This is in good agreement with the previously measured finesse for the planar cavity (F = 10) discussed in section 3.6.1. The slight asymmetry in the mode may be due to the presence of the curved mirror. At a detuning, $\delta x = 5$ μm, the planar mode broadens and hints of narrower features are observed (b). The single mode splits dramatically into a family of much narrower modes at a lateral detuning, $\delta x = 4$ μm (c). The laser spot is close enough to the centre of the curved mirror for its curvature to alter the cavity spectrum by confining the beam laterally.

Cavity modes are labelled (red) from 0-4 in figure 3.19. Mode 0 is the longitudinal cavity mode and modes 1-3 are the associated transverse modes. As the spot is moved

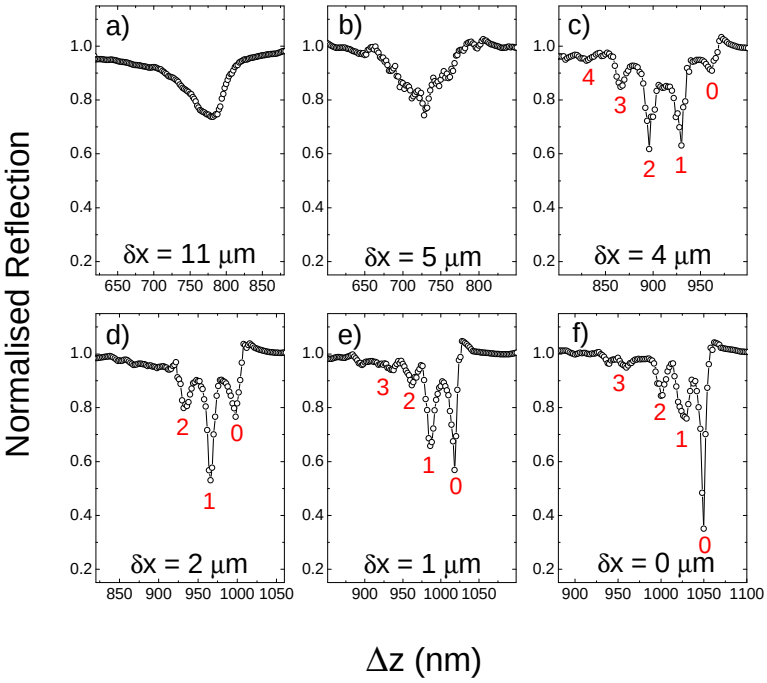

Figure 3.19: The reflection spectra from the silver/dielectric microcavity at room temperature. a) The cavity mode at the very edge of the curved mirror. The finesse is 15.
b) to f) Shows the evolution of the cavity mode spectrum from planar to curved. The finesse of the longitudinal cavity mode in (f) is 130.

closer to the centre of the curved mirror, the signal strength of the first transverse mode is maximised in Figure 3.19 (d) only a small lateral displacement (2 μm) from the crater centre. However the longitudinal mode has a stronger signal, closer to the centre (e). The mode spectrum (f) is characteristic of a fully aligned half symmetric cavity, the probing laser spot is in the centre of the curved mirror.

At the centre of the curved mirror the longitudinal mode has the narrowest linewidth and strongest signal. The finesse is 130 for the fundamental mode. The first transverse and second transverse modes have a finesse of 52 and 45 respectively. The reflectivity of an opaque silver coating at $\lambda = 950$ nm is typically 95-98% [71]. This value is much lower than the estimated reflectivity of M_d (99.7%), therefore the cavity finesse is dictated by the silver mirrors reflectivity. The reflectivity of the silver mirror required to give F = 130 is 96%, calculated from equation 1.20. This is within the expected reflectivity range [71].

3.9.1 Low temperature test

The next logical progression to realising a fully tunable microcavity for quantum dot experiments was to ensure that a curved mirror could be located and a cavity established at low temperature. The major difference when operating at 77 K compared to 300 K is that the cavity is completely enclosed in the microscope tube. The cavity air gap could no longer be examined with an optical microscope, as was possible at room temperature.

The cavity was cooled to 77 K using liquid nitrogen and the 952.1 nm laser spot was aligned with a curved mirror using the fixed wavelength dithering and scan method described earlier. The dithering alignment method worked as successfully at 77 K as it did at room temperature. The reflection spectrum from the cavity was recorded as a function of the voltage applied to piezo, figure 3.20 (a). The finesse of the longitudinal mode was measured to be 62. The z piezo positioner required a voltage 7 times greater at 77 K than at room temperature to move the equivalent distance.

The finesse of the cavity was also measured using a broad band source. The advantages of using a broad band source to characterise the cavity include direct measurement of the cavity spectral line width and free spectral range. Knowing the wavelength of two adjacent longitudinal cavity modes also allows the cavity length to be calculated using,

$$L = \frac{1}{2\Delta(1/\lambda)}, \tag{3.13}$$

where $\Delta(1/\lambda)$ is the change in wave number from one longitudinal mode to the next.

White light from a broad band source (Thorlabs OSL1) was focussed in to the same cavity as in figure 3.20. This ensured that the white light characterised the same cavity spectrum as the 952.1 nm laser. The reflected light was collected using the confocal microscope and the signal displayed on the spectrometer. Due to a very low signal from the cavity under white light reflection, each spectrum required a long integration time (several seconds) and background correction to compensate for the white light's spectral profile.

Figure 3.20 (b) shows the the white light reflection spectrum from the same cavity as characterised in (a). A longitudinal mode is shown at $\lambda = 952.1$ nm and three transverse modes are visible at lower wavelengths.

A comparison of the two plots in figure 3.20, shows that the same spectrum is obtained by scanning the cavity length and probing the cavity with a fixed wavelength laser or by using a white light source (to scan the wavelength) and keeping the

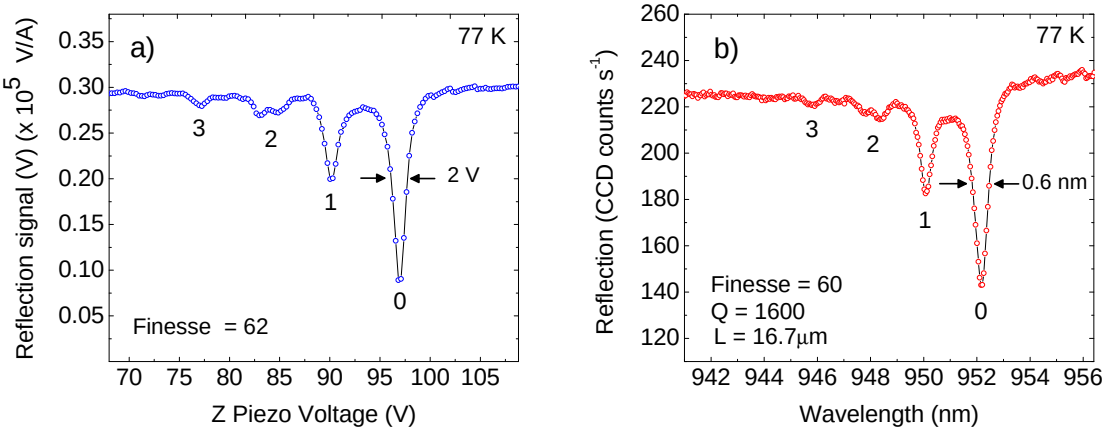

Figure 3.20: a) Fixed wavelength laser (λ = 952.1 nm) cavity reflection measurement and b) white light reflection from the same cavity. Both plots were taken at 77 K, from a silver/dielectric hybrid cavity of length 16.7 μm.

cavity length constant. The measured finesse is the same (F = 60) for both plots, regardless of how the cavity is probed. The FWHM of the longitudinal mode in (b) was determined to be $\delta\lambda$ = 0.66 nm by fitting a Lorentzian lineshape to the peak. The cavity Q was determined using,

$$Q = \frac{\lambda}{\delta\lambda} = 1442.4, \tag{3.14}$$

where λ and $\delta\lambda$ are the longitudinal mode wavelength and line width respectively.

The wavelength of the adjacent longitudinal mode was measured from the white light reflectivity spectrum at λ = 925.3 nm. The free spectral range was calculated to be 26.8 nm. The cavity length was calculated to be 16.7 μm using equation 3.13.

3.9.2 High finesse cavity

The ultimate goal was to obtain a much higher finesse than that achievable with the metal/dielectric cavity discussed in section 3.9, where the finesse is limited by the relatively low reflectivity of the metal mirror. In order to improve the cavity reflectivity the metal mirror was replaced with a dielectric coated curved mirror (coated with M_d). The other mirror was replaced by the semiconductor DBR (M_s). This cavity configuration is shown schematically in figure 3.21.

The use of a dielectric coating (M_d) on the curved mirror allowed it to be used as

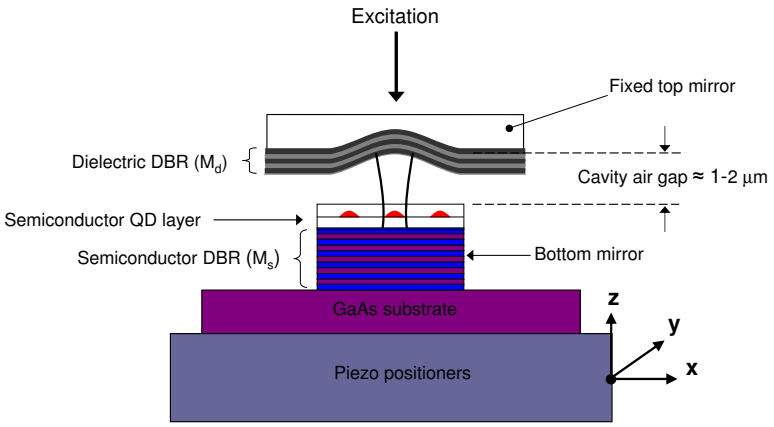

Figure 3.21: Half symmetric cavity schematic diagram. The curved mirror template was coated in the same coating from O.I.B (M_d) as the planar mirrors discussed earlier. The bottom mirror is the semiconductor mirror, M_s.

the top mirror of the cavity. This allowed greater flexibility as the cavity could now be probed in both transmission and reflection.
To characterise the cavity, the 950 nm laser was aligned with a curved mirror by dithering the z piezo positioner and moving the cavity unit in the x and y directions to maximise the transmission signal of the longitudinal mode (as in section 3.9).

Figure 3.22 shows the fixed wavelength transmission spectra versus cavity length. The figure shows two adjacent longitudinal modes and corresponding transverse modes. A cavity finesse of 1,500 for the longitudinal mode was measured at an effective cavity length of 9.7 μm (measured from the white light reflection spectra). Although the free spectral range can be determined using white light reflection, the cavity linewidth is so narrow that the spectrometer's 300 g/mm grating cannot fully resolve the mode's linewidth. The 1200 g/mm grating has a greater resolution (≈80 μeV), but the small cavity signal and interference effects in the spectrometer rendered measuring the cavity linewidth with the white light source impractical.

The finesse from a planar cavity formed with the mirrors M_d and M_s (discussed in section 3.6.1) was typically about 15. The longitudinal mode of the curved mirror cavity has a finesse of 1,500. This increase of two orders of magnitude is due to the curved mirror eliminating the losses from beam walk-off. The measured finesse (F = 1,500) compares well with the maximum finesse limited only by the reflectivity of the mirrors. The dielectric mirror has an estimated reflectivity of R = 99.75% and the

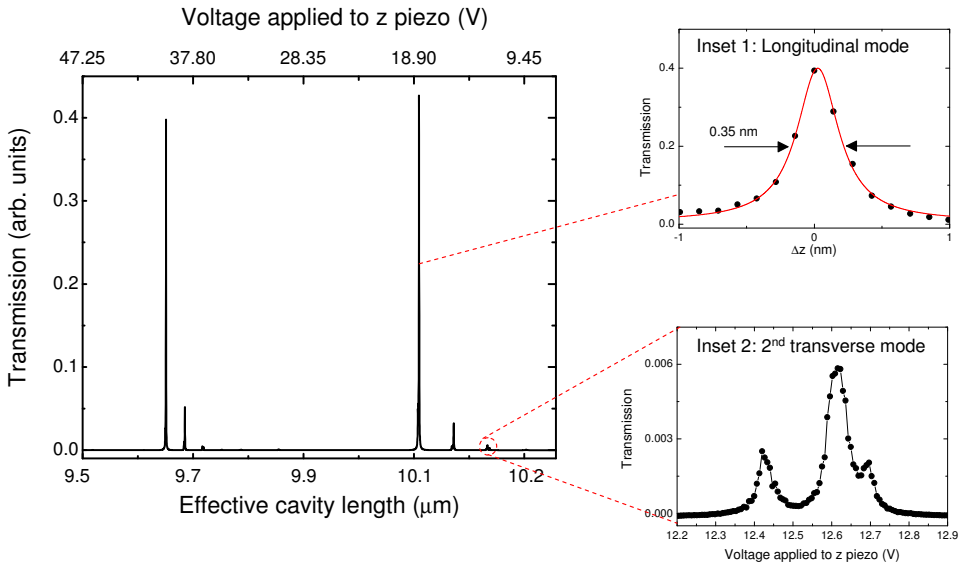

Figure 3.22: Fixed wavelength ($\lambda = 950$ nm) transmission versus cavity length for the half symmetric cavity at room temperature. The finesse is 1,500 at an effective cavity length of 9.7 μm. Inset 1 shows the line shape of the fundamental mode (red line is a Lorentzian fit). Inset 2 shows the second transverse mode, which comprises three peaks.

semiconductor mirror, R = 99.9%. These reflectivities give a calculated finesse F = $\pi\sqrt{R}/(1-R) \approx 1{,}586$.

The semiconductor DBR has a lambda layer of quantum dots as the final layer, however the cavity is characterised without exciting the quantum dots. Photoluminesence measurements from the quantum dots in the cavity in this geometry are detailed in chapter 4.

3.10 Summary

This chapter presented the realisation of a tunable microcavity. The technology had a high degree of wavelength tunability and was operational at cryogenic temperature. The use of a miniaturised concave mirror reduced diffraction losses and increased the finesse by about a factor of 100 compared to a planar microcavity. The formation of an ultra-smooth concave mirror by laser ablation was key in maximising the cavity's finesse. The atomically smooth silica surface provided the ideal template for the dielectric coating. The finesse of 1,500 measured from the half symmetric resonator

encouraged the exploitation of the tunable cavity, and the possibility of optimally coupling a single semiconductor quantum dot to the cavity mode. This is the subject of chapter 4.

Chapter 4

Quantum dots in a tunable microcavity

In chapter 3 a novel fully tunable microcavity was presented and the microcavity was characterised using a fixed wavelength laser and tuning the cavity length. This chapter demonstrates the exploitation of the tunable cavity, coupling the cavity mode to a single quantum dot at 4 K by positioning the dot at the exact antinode of the cavity's electric field.

4.1 Cavity characterisation with PL at 77 K

The length of the cavity was determined in chapter 3 by using a white light source to measure the free spectral range. A more elegant method to measure the cavity length and the cavity Q-factor is to utilise the PL emission from the InGaAs quantum dots embedded in the microcavity. In free space the quantum dots' PL emission is spectrally broad at 77 K due to inhomogeneous broadening from hundreds of dots of different sizes. Utilising the quantum dots' PL as an internal light source to characterise the cavity has a practical advantage over using an external white light source. The PL emission from the array of dots is very bright, giving high quality data within a short integration time. The high finesse cavity, discussed in chapter 3 section 3.9.2, was characterised using the quantum dots' PL emission. The bottom mirror of the cavity was the planar semiconductor mirror (sample 61004C, with the etched mesa discussed in chapter 2). The cavity was completed with a fused silica substrate containing an array of curved mirrors with a TiO_2/SiO_2 (10 pairs) dielectric coating (coating M_d is summarised in chapter 3, table 3.1).

To measure the cavity Q and the cavity length, the collection optics (described in chapter 2) were aligned with one of the microscopic curved mirrors, using the fixed

950 nm laser alignment technique discussed in chapter 3.

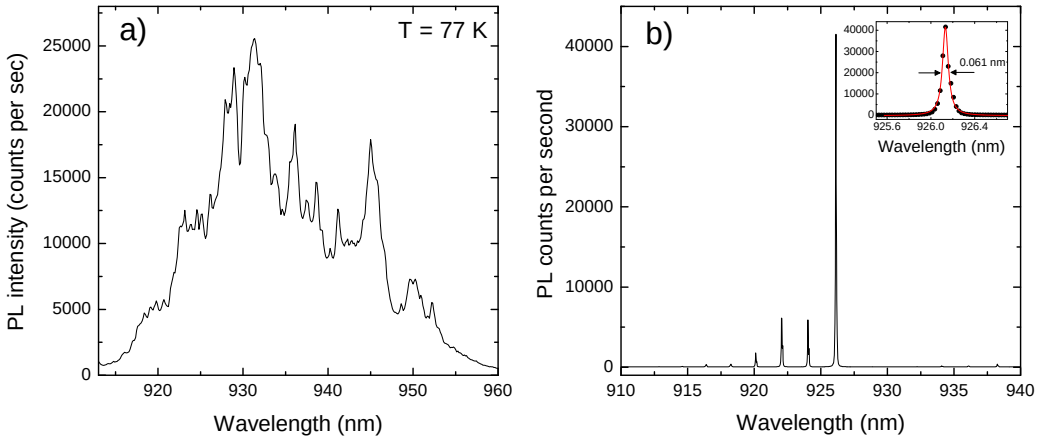

Figure 4.1: a) Free space PL from a dense quantum dot array in sample 61004C at 77 K. The dots were non-resonantly excited at $\lambda = 830$ nm with an excitation power density of 1 $\mu W/\mu m^2$. b) A curved mirror cavity mode and corresponding family of transverse modes, excited by the PL at $T = 77$ K from sample 61004C. The cavity length is $L_{eff} = 15.5$ μm and the cavity $Q = 15,500$. The PL is strongly suppressed at non-resonant wavelengths. The inset shows the longitudinal cavity mode fitted with a Lorentzian lineshape (red line). The measured linewidth is close to the spectrometer's resolution (0.04 nm).

The photoluminescence from an ensemble of dots in free space at 77 K is shown in Figure 4.1 (a). The excitation wavelength was 830 nm and a power density of 1 $\mu W/\mu m^2$. The broad band emission ($\Delta\lambda \approx 50$ nm) provides a convenient internal light source for characterising the tunable cavity. Figure 4.1(b) shows the PL at 77 K from the tunable cavity. The air gap length was adjusted using the z piezo positioner to ensure a strong fundamental cavity resonance at $\lambda = 926$ nm. The transverse modes of the cavity are also visible at lower wavelengths. An effective cavity length, $L_{eff} = 15.5$ μm was calculated from the free spectral range ($FSR = 28$ nm) using equation 3.13. The linewidth of the fundamental mode was determined by fitting the data with a Lorentzian lineshape (red line) with a FWHM = 0.061 nm. The FWHM was 0.06 nm, 0.066 nm and 0.064 nm for the first, second and third transverse modes respectively.

Using Q = $\lambda/\Delta\lambda$, the longitudinal cavity mode was calculated to give Q $\approx$ 15,500. The measured linewidth, Γ_{meas} is a convolution of the spectrometer linewidth, Γ_{spec} and the real linewidth, Γ_{real}. The measured linewidth is given by,

$$\Gamma^2_{meas} = \Gamma^2_{real} + \Gamma^2_{spec}. \tag{4.1}$$

This is a good approximation for Lorentzian lineshapes. All stated linewidths throughout this work have been corrected in this way.

4.1.1 Q versus cavity length

The Q-factor is a linear function of the cavity photon lifetime (chapter 1, equation 1.19), therefore, in principle a longer cavity confines photons for a longer time than a short cavity, leading to a higher measured Q. However in practice the cavity mode could experience large diffraction losses at larger mirror spacings. The beam waists on the two mirrors increase monotonically as the cavity length is increased, until the cavity length equals the radius of curvature of the concave mirror (this is discussed in chapter 3, section 3.7.2). This increase in beam waist could lead to the cavity Q being limited by the physical size of the curved mirror.

An experiment was devised to measure the Q-factor as a function of the cavity length. The mirrors used to form the cavity (used in section 4.1) were cleaned, to enable the minimum possible air gap to be obtained. The experiment was conducted at 77 K using the same set-up as in section 4.1. The cavity free spectral range and Q were measured from the cavity PL as described previously. The excitation power density was 1 $\mu W/\mu m^2$ at a wavelength of 830 nm. The cavity air gap was systematically increased in steps of ≈ 5 μm, by lowering the bottom mirror using the cavity z piezo positioner. The PL cavity spectra were recorded on the spectrometer (integration time = 1 second). At a cavity length of ≈ 30 μm, the cavity Q was too large to be accurately measured using the 1200g/mm grating in the spectrometer. In order to measure Q, the cavity mode spectrum was recorded using the fixed wavelength technique described in chapter 2. This technique gives a plot of cavity transmission signal versus piezo voltage and has a greater resolution than the spectrometer grating (discussed in chapter 3). A plot of applied voltage versus cavity emission wavelength using the PL was then used to convert the FWHM of the cavity mode in volts to wavelength. The two methods of recording the cavity spectrum were shown in chapter 3, section 3.9.1 to be equivalent.

Figure 4.2 shows the measured Q-factor at 77 K versus cavity length. The effective cavity length was determined by measuring the free spectral range in PL between the two adjacent longitudinal modes. The cavity lengths were calculated using equation 3.13.

A linewidth of $\Delta\lambda_c = 0.14$ nm and $\Delta\lambda_c = 0.017$ nm was measured for a cavity length of 4.75 μm and 45 μm respectively. Figure 4.2 shows that Q = 6,700 for the shortest possible cavity effective length (≈ 4.75 μm). The Q-factor rises linearly to Q = 55,000 as the cavity length is increased to $L_{eff} = 45$ μm.

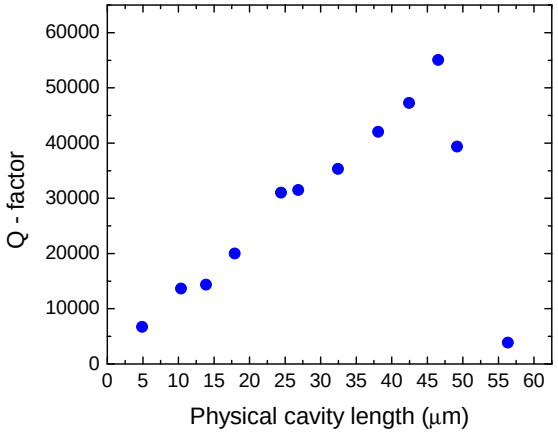

Figure 4.2: The measured Q-factor for various physical cavity lengths. The cavity length was determined by measuring the free spectral range. The modes were driven by an ensemble of non-resonantly excited InGaAs quantum dots at $T = 77$ K.

The data indicate that Q increases linearly with cavity length, reaching a maximum value at $L_{eff} = 45$ μm. Any further increase in cavity length results in an increased linewidth and a reduction in the measured Q. When $L_{eff} < 45$ μm the observed behaviour is consistent with the theory in chapter 3 (Q increases linearly with cavity length). When the cavity is at the hemispherical point ($2L_{eff} = $ R), any further increase in cavity length renders the cavity unstable, the beam waists at both mirrors increase and the Q decreases rapidly. At very long cavity lengths the beam waist is so large that the curved mirror no longer provides any lateral confinement and diffraction losses dominate. The observed behaviour is consistent with a curved mirror radius of curvature of R = 2L = 90 μm. This agrees well with the physically measured radius of curvature (R = 120 μm) using the surface profiler in chapter 3.

The larger Q at longer cavity lengths could be used to achieve the strong coupling regime with a single quantum dot, using relatively low reflecting mirrors. It is possible that at short cavity lengths a dot within the cavity is in the weak coupling regime due to the relatively low Q; and at longer cavity lengths the higher Q could push the system into the strong coupling regime. Achieving the strong coupling regime requires maximising the $Q/\sqrt{V}$ ratio (discussed in chapter 1). Longer cavities have been successfully used in atomic physics, where atom/cavity experiments have utilised high Q cavities with long cavity lengths (>20 μm) to couple to ensembles of atoms [72, 73] and more recently a single atom [31, 33, 74].

The cavity is operated with a minimum air gap ($L_{air} \approx 2$ μm) in the work within this chapter (unless stated otherwise). The smaller the cavity volume, the greater the modified photon density of states (chapter 1, equation 1.4) for a given cavity Q. Therefore for single dot Purcell experiments minimising the cavity length is crucial

to obtaining a maximal Purcell effect as the Q/V ratio is maximised at the shortest cavity length.

4.1.2 PL transverse mode spacings

In principle the separation of the fundamental mode and the first transverse mode depends on the cavity length and the radius of curvature (equation 3.10). For a fixed radius of curvature the transverse mode spacings depend only on the cavity length. Verifying the value of the radius of curvature experimentally is useful for calculating the size of the beam waist at the curved mirror. The radius of curvature can also be used to calculate the cavity length at which the maximum Q is obtained (as discussed in the previous section). Using the data collected from the experiment in the section 4.1.1, the wavelength separation (nm) between the first transverse mode and the fundamental mode was calculated and recorded as a function of cavity length. This procedure was repeated for the separation between the second transverse mode and the fundamental mode.

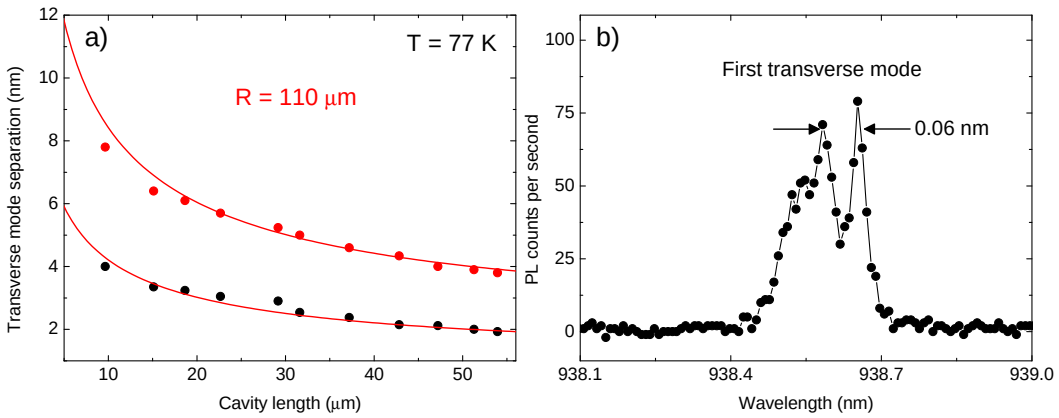

Figure 4.3: a) Measured separation of the first transverse mode (black data points) and second transverse mode (red data points) from the fundamental mode versus cavity length. The radius of curvature is a fitting parameter and the red line corresponds to R = 110 μm. b) The 0.06 nm splitting observed in the first transverse mode.

Figure 4.3 (a) shows the experimentally measured separation of the first and second transverse modes from the fundamental cavity mode. As expected from equation 3.10, the spacing between the transverse modes increases with decreasing cavity length. The red line is a fit to the data using equation 3.10. The top mirror's radius of curvature R is the fit parameter with a good fit obtained for R = 110 μm. This agrees well with

the surface profiler measurements for these mirrors (R = 120 μm) in chapter 3 and is also in good agreement with the value (R = 90 μm) from the previous section.

A small spectral splitting was observed in the first transverse mode for this cavity. The magnitude of the splitting was 0.06 nm, figure 4.3 (b). Only about 10% of all the curved mirror cavities characterised showed a splitting in the first transverse mode. This splitting could be due to a slightly asymmetric curved mirror.

4.2 Quantum dots in a tunable cavity at 4 K

At 4 K the quantum dots' optical linewidths are extremely narrow (close to lifetime limited), at just 1-2 μeV [6]. The use of such spectrally narrow emitters has been key to observing a large Purcell effect [16]. However such narrow linewidths place a high demand on the cavity, requiring a high cavity Q (Q = 10^6 for optimal coupling) to enable coupling with a single dot. A spectral map of the dots within the cavity would enable bright, isolated dots to be identified and the cavity/dot coupling to be studied.

The cavity was cooled to a temperature of 4 K in the liquid helium dewar. The collection spot was aligned close to the centre of a curved mirror using the techniques described in chapter 3. The dot sample was from the high density part of the wafer ($\approx 10^{10}$ dots cm^{-2}). The excitation pump density was 8 μW/μm^2. The cavity air gap was minimised, giving a minimum cavity length of 6.1 μm, calculated using the free spectral range (FSR = 48 nm). The free spectral range for this cavity configuration with no air gap was calculated to be 70 nm.

The PL from the cavity was collected using the confocal microscope (discussed in chapter 2). The cavity air gap was increased by $\approx$ 100 nm to tune the cavity mode spectrally to the low energy tail (λ = 950 nm) of the dense quantum dot array, thus allowing individual dot lines to be isolated. The cavity was systematically shortened by applying 0-70 V in steps of 70 mV to the z piezo positioner and the PL was recorded after each voltage step.

The PL emission from the tunable cavity as a function of cavity voltage at 4 K is shown in figure 4.4. The main diagram top axis shows the cavity length as calculated from the free spectral range and calibrated from the known piezo voltage characteristics (discussed in chapter 3). Various exciton PL lines can be seen as faint lines of constant energy, running horizontally across the plot. The intensity of the dot emission increases towards the point of intersection (zero detuning) with the longitudinal cavity mode (white areas). The longitudinal (0), first (1) and second (2) transverse modes are also shown in figure 4.4. The longitudinal mode (labelled 0) is

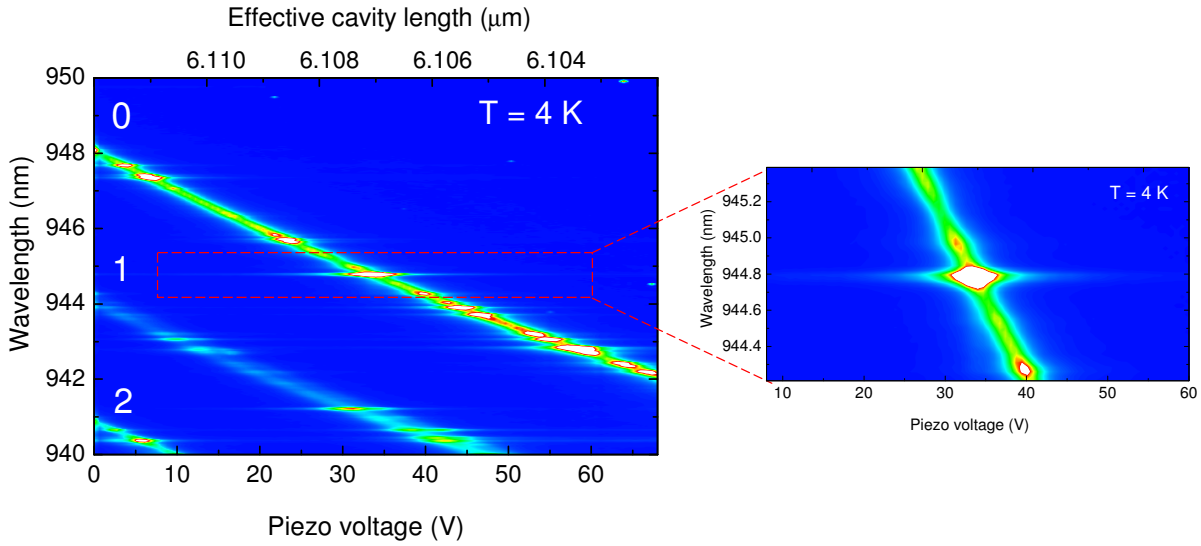

Figure 4.4: PL from sample 61004C within the cavity at 4 K versus piezo voltage. The excitation pump density is 8 μW/μm^2. Several quantum dots at different wavelengths are visible, weakly coupling to the cavity mode. White areas correspond to 30,000 counts on the detector and blue areas to 0 counts. The fundamental cavity mode (0) has been tuned to the low energy tail of the quantum dot array. The presence of the first and second transverse modes is also observed at lower wavelengths (labelled 1 and 2 respectively). The inset highlights a single crossing at $\lambda = 944.8$ nm.

the most prominent and is visible in figure 4.4 as a feature (green) starting at 948 nm and a piezo voltage of 0 V and running diagonally through the plot to 942 nm. The inset in figure 4.4 shows an enlarged view of the longitudinal mode crossing a single exciton at 944.8 nm. The data shown in figure 4.4 demonstrates that the tunable cavity can operate at 4 K and can be spectrally tuned to resonance with the quantum dots emitting within the cavity mode region. Figure 4.4 also shows that the cavity mode is continuously visible, even when it is not resonant with a quantum dot.

The presence of a broad band emission feeding the cavity mode has been reported in the majority of single quantum dot/cavity experiments in other types of microcavity including micropillars and photonic crystals [47]. This has been observed when there are no dots resonant with the cavity mode [47]. Although not fully understood, several mechanisms have been proposed to account for the background emission. One possibility is wetting layer-QD continuum transitions [30], another is multi-excitonic background emission from the quantum dots [47].

The tunable cavity can be used to investigate this effect by detuning the cavity more than 10 nm from any quantum dots and recording the spectra. A curved mirror cavity was constructed using the same mirrors as above, and cooled to 4 K. The dots within the cavity were excited at 830 nm with a pump density of 10 $\mu W/\mu m^2$. Using the PL, the fundamental cavity mode was tuned to $\lambda = 970.5$ nm. The minimum cavity length was calculated from the free spectral range to be 14.2 μm. The minimum cavity length was not as short as that obtained in the previous experiment. This was likely caused by contaminants between the mirrors, although the etched mesa sample was used to try and prevent this. The cavity length was decreased by applying 110 V to the z piezo positioner in steps of 0.01 V and the PL spectrum was recorded at each cavity length.

Figure 4.5 (a) shows a typical dot distribution at 4 K, from the PL spectra in free space from sample 61004C. There are very few or no dots emitting above $\lambda = 955$ nm in figure 4.5 (a). Figure 4.5 (b) shows a colour plot of the cavity PL wavelength versus cavity length at 4 K. At $\lambda = 970$ nm the cavity resonance is spectrally detuned by more than 10 nm from any quantum dots and yet a strong optical mode exists. It is clear from figure 4.5 (b) that the cavity mode is not coupling to any quantum dots, by comparing the plot to figure 4.4 which shows dot lines and areas of high intensity as the cavity couples to individual dots. This behaviour is not observed in 4.5 (b). The cavity mode intensity diminishes when it is tuned above 970 nm and is no longer visible at wavelengths above 980 nm.

The observation of a cavity mode in the 960−970 nm region, despite the lack of any quantum dot PL emission in that spectral region from sample 61004C indicates the presence of a broad background emission. It could be the case that the broad

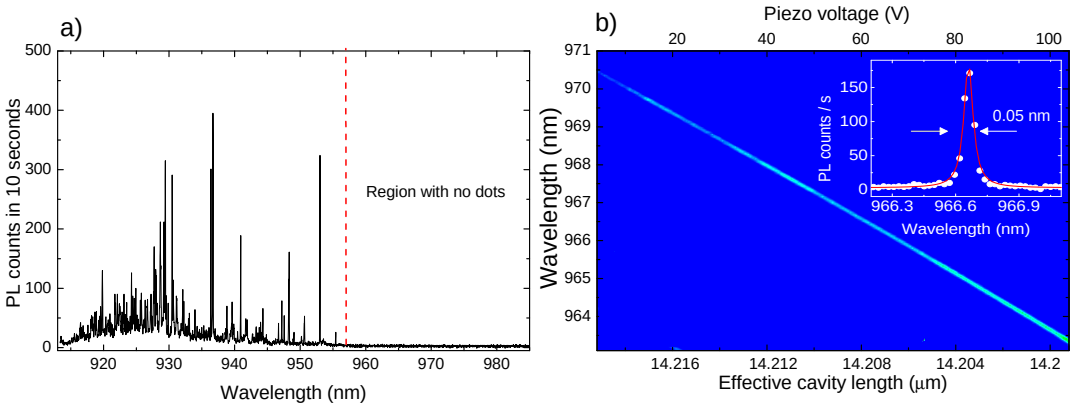

Figure 4.5: a) A typical spectrum at low excitation power (0.1 $\mu W/\mu m^2$), showing the spectral distribution of the quantum dots from the high dot density area of sample 61004C in free space at 4 K. There are no dots emitting above $\lambda = 955$ nm. b) A colour plot of the PL from the fundamental cavity mode at 4 K tuned from 971−963 nm. The cavity mode is detuned by 10 to 15 nm from any quantum dots in sample 61004C. The inset shows data from the contour plot, showing the cavity emission at $\lambda = 966.67$ nm. The sample was non-resonantly excited at 4 K with an excitation pump density of 10 $\mu W/\mu m^2$ at $\lambda = 830$ nm and the integration time for each spectrum was 10 seconds.

background emission in micropillar and photonic crystal microcavities arises due to defect states introduced during the etching process. The results in figure 4.5 are important because they appear to rule out the possibility of the etching process (used to fabricate micropillar and photonic crystal cavities but not the tunable cavity) being the source of the highly detuned emission.

The cavity Q is ≈ 20,000, measured by fitting a Lorentzian lineshape to the cavity mode at $\lambda = 966.67$ nm (inset, figure 4.5 (b)). This in good agreement with the Q measured at T = 77 K for a cavity length of 14.2 μm (figure 4.2).

4.3 Single quantum dot in a tunable cavity

It is desirable to isolate and study a single quantum dot within the cavity. Studying a single dot simplifies the cavity emission spectrum, allowing any contribution from other dots to be conclusively ruled out. Ruling out multiple dot effects is particularly important when studying the photon statistics from the resonant cavity emission. In particular, cavity enhanced single photon sources require a single quantum emitter resonant with the cavity mode.

To investigate the effect of the cavity mode on a single quantum dot, one dot at λ

= 946.85 nm was selected for its large spectral isolation from other dots and its strong PL signal. The cavity mode had a measured linewidth of $\Delta\lambda_c = 0.15$ nm which gave Q = 6,500.

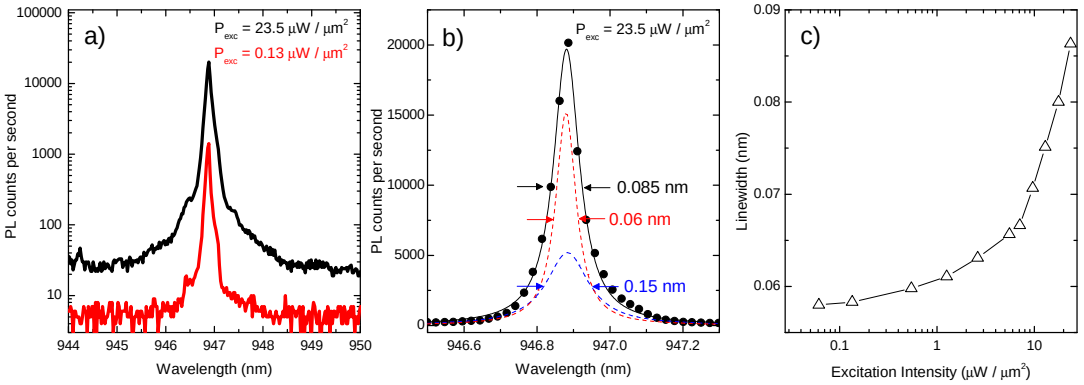

Figure 4.6: a) The cavity mode on resonance with an exciton at $T = 4$ K. At high excitation power (black curve) the background emission into the cavity mode is observed as a broadening at the peak's base. b) The PL peak with the cavity on resonance with the exciton (black data points) with an excitation power density of 23.5 μW/μm^2. The red and blue dotted lines represent the exciton and cavity mode respectively. c) The measured PL linewidth from Lorentzian fits of the exciton on resonance with the cavity as a function of excitation power density.

The cavity mode was tuned to exact resonance with the chosen dot and the resulting PL spectra examined under high and low excitation conditions, figure 4.6 (a). The data are shown on a log scale (y-axis) for clarity. At low excitation power (P_{exc} = 0.13 μW/μm^2) the narrow emission line of the quantum dot is clearly seen (red line). The linewidth in this case is 0.06 nm and is limited by the spectral resolution of the spectrometer grating. However under high excitation (P_{exc} = 23.5 μW/μm^2) the resonant linewidth increases to 0.85 nm (black line). The resonant spectra at high power (P_{exc} = 23.5 μW/μm^2) is shown on a linear scale in figure 4.6 (b) (black data points). It is fitted with a Lorentzian lineshape with a FWHM = 0.085 nm. Figure 4.6 (c) shows how the measured on-resonance linewidth depends on the excitation power. There is a clear increase in the measured linewidth with increasing excitation power.

The cavity mode appears to contribute more to the on-resonance signal at higher excitation power, indicating that the cavity mode intensity has a different power dependence than the exciton. The combined contribution of the cavity mode and exciton to the observed PL spectra is illustrated in 4.6 (b). The dashed red line is a Lorentzian with a linewidth of 0.06 nm, determined by fitting to the low power (P_{exc}

= 0.13 μW/μm^2) data in figure 4.6 (a). The dashed blue line represents the cavity mode, with a linewidth of 0.15 nm. The sum of the two Lorentzians fits the shape of the high power PL spectra in (a).

The exciton and cavity mode intensities can be compared by examining the intensity of each, whilst the cavity is spectrally detuned by +0.5 nm. To investigate the power dependence, the cavity was lengthened, tuning the cavity mode to 947.3 nm. The excitation power was increased from P_{exc} = 0.13 μW/μm^2 to P_{exc} = 23.5 μW/μm^2 and the +0.5 nm detuned cavity/exciton spectrum was recorded at each power. This was repeated for a cavity detuning of +0.25 nm.

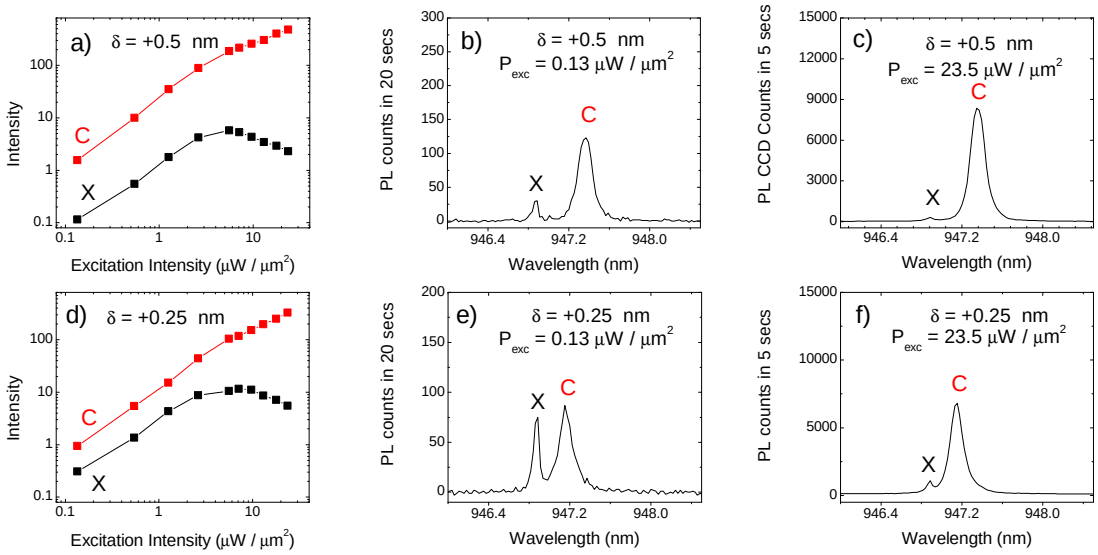

Figure 4.7: a) Excitation power dependence for the exciton (black) and the cavity mode (red) at 4 K using the same cavity as in figure 4.6. The cavity is detuned from the exciton, δ = +0.5 nm. b) and c) corresponding low and high excitation spectra respectively.
d) Excitation power dependence for the exciton (black) and the cavity mode (red) at δ = +0.25 nm. e) and f) corresponding low and high excitation spectra respectively.

Figure 4.7 (a) shows the integrated intensity (determined by a Lorentzian fit to the exciton and cavity mode). Figure 4.7(b) and(c) show the cavity mode (C) at δ = +0.5 nm from the exciton (X), the excitation power density is P_{exc} = 0.13 μW/μm^2 and P_{exc} = 23.5 μW/μm^2 respectively. The data show the relative intensity of the cavity mode compared to the exciton at a constant (+0.5 nm) detuning. Figure 4.7 d, e and f show corresponding data for a reduced cavity detuning of +0.25 nm. When the cavity mode is detuned by +0.5 nm, the exciton intensity increases linearly and saturates at $P_{exc} \approx$ 5.5 μW/μm^2 (determined from the maximum integrated intensity). The cavity mode intensity increases in a similar linear fashion, but does not saturate at

high power.

As the excitation power is increased above 5.5 $\mu W/\mu m^2$ the cavity mode becomes increasingly more intense than the exciton. The background states which emit into the cavity mode do not saturate below $P_{exc} = 23.5\ \mu W/\mu m^2$ allowing the mode to become increasingly intense with increasing excitation power. At $P_{exc} = 0.13\ \mu W/\mu m^2$ and a cavity detuning of +0.25 nm (figure 4.7 (e)), the relative exciton intensity (compared to the cavity mode) is increased by a factor of 5 over that shown in figure 4.7 (f) which shows the spectrum recorded at the same detuning but excited at $P_{exc} = 23.5\ \mu W/\mu m^2$ (figure 4.7 (f)). However the cavity mode intensity still dominates the spectra as the exciton saturates.

The results in figure 4.7 confirm the importance of performing the dot/cavity experiments at low excitation power to ensure the signal is comprised primarily of exciton emission without broad band emission from the cavity mode.

4.3.1 Purcell effect : CW power dependence of the exciton

A CW power dependence of the exciton at various cavity detunings can reveal clear signatures of the Purcell effect. In free space, an exciton's PL intensity increases linearly with excitation power and saturates at some higher power which corresponds to the pump rate required to completely populate the excited state. When the exciton is in free space it will saturate at much lower excitation powers than in a high Purcell factor cavity [75]. The quantum dot is less subject to excited state filling (due to an increased spontanteous emission rate) when it is on resonance with a high Q, low modal volume microcavity.

A CW power dependence was used to investigate the effect of detuning on the saturation point of the single dot discussed in section 4.3. The same dot and cavity discussed in the previous section were used; the cavity was tuned to exact resonance with the dot. The excitation power was varied from $P_{exc} = 0.13\ \mu W/\mu m^2$ to 23.5 $\mu W/\mu m^2$ and the PL from the cavity recorded at each power. This procedure was repeated with the cavity detuned from the dot by +0.2, +0.3 and +0.5 nm.

Figure 4.8 shows the measured exciton power dependence at various cavity detunings. All the slopes show a linear power dependence at low power and then saturate at various higher excitation powers. The slope in the linear region at low power is $m = 1.1$, indicating that the dot transition is a single exciton and not a biexciton [76], most probably the neutral exciton (X^0). An enhancement of the PL integrated intensity by a factor of ≈85 was found for the exciton at zero detuning compared to the exciton at +0.5 nm detuning. The cavity detuning also alters the saturation point, strong evidence of the Purcell effect. The cavity effect on the saturation of

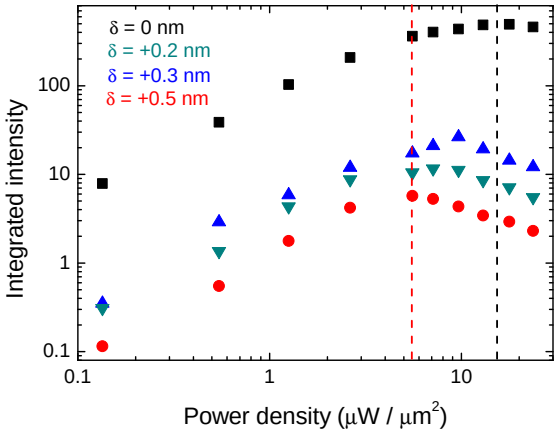

Figure 4.8: Excitation power dependence of the integrated intensity of the exciton within the tunable cavity at 4 different cavity detunings. At $\delta = +0.5$ nm the exciton saturates at $P_{exc} = 5.5\ \mu\text{W}/\mu m^2$ (red dashed line). At $\delta = 0$ nm the exciton saturates at a much higher excitation power density, $P_{exc} = 16\ \mu\text{W}/\mu m^2$ (black dashed line).

the PL can be seen in figure 4.8. When the cavity is +0.5 nm detuned from the exciton (red data points), the PL saturates at $P_{exc} = 5.5\ \mu\text{W}/\mu m^2$ (dashed red line). As the cavity/dot detuning is decreased (green and blue dots), the saturation point shifts to higher excitation power. When the cavity is tuned to resonance with the dot (black dots) the excitation power required to saturate the transition is a factor of 3 higher (dashed black line) than than the off-resonance case. Extracting the radiative lifetime, τ_{rad} using this approach is difficult and it is better to measure τ_{rad} directly.

A notable feature in figure 4.8 is that after saturation pump power is reached, the intensity saturates in each spectrum and then there is a noticeable decrease of intensity at increasing power. This can be attributed to the presence of higher excited states.

4.3.2 Correlation measurements

Photon correlation measurements were performed (using the HBT interferometer described in chapter 2), to confirm that only a single quantum dot was interacting with the cavity mode and that the emission from the cavity was dominated by the exciton. The cavity was tuned to exact spectral resonance with the quantum dot and excited with a pulsed laser at $\lambda = 830$ nm at a repetition rate of 40 MHz and a pulse duration of 80 ps.

Figure 4.9 shows two correlation measurements taken at different excitation powers. The diminished peak at time zero, $g^2(0)$, indicates anti-bunching, characteristic

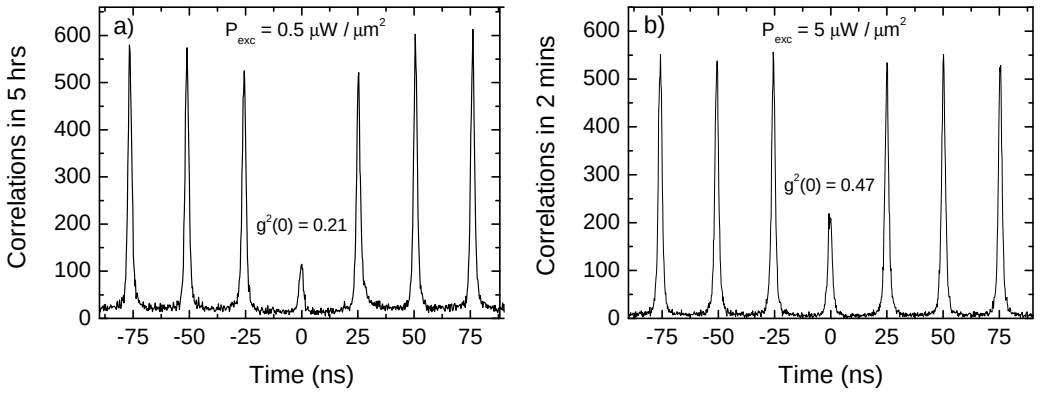

Figure 4.9: Photon correlation measurements on a single quantum dot resonant with the cavity. a) low excitation power density, $P_{exc} = 0.5\ \mu\text{W}/\mu m^2$ and b) high excitation power density, $P_{exc} = 5\ \mu\text{W}/\mu m^2$.

of a single quantum emitter. Figure 4.9 (a) shows the measured $g^2(0) = 0.21$ at a power density $P_{exc} = 0.5\ \mu\text{W}/\mu m^2$. A measured $g^2(0) < 0.5$ indicates that the system is an effective single photon source. At an increased power density $P_{exc} = 5\ \mu\text{W}/\mu m^2$ the second-order correlation function increases to 0.47 (Figure 4.9 (b)). This can be understood by considering that at high excitation power the number of electron-hole pairs occupying the dot is large. The increase in $g^2(0)$ is due to the increased probability that multiple photon emission per pulse will occur [8].

4.3.3 Long time-scale antibunching

Most dots showed similar correlation measurements to the data in figure 4.9. However about 10% of the 20 dots studied showed diminished correlations close to time zero, which slowly recovered within $\tau = 100$ ns. Curiously this effect was only seen at low power ($< 2\ \mu\text{W}/\mu m^2$). Figure 4.10 shows the effect at 3 different excitation powers (rep rate = 40 MHz). Figure 4.10 (a) shows a correlation measurement from a single dot resonantly coupled to the longitudinal cavity mode. The excitation power is $P_{exc} = 0.4\ \mu\text{W}/\mu m^2$ and the measured $g^2(0)$ is 0.2, demonstrating clear anti-bunching.

However the adjacent correlation peaks are slightly reduced close to time zero. This effect is less pronounced at an excitation power of $P_{exc} = 0.7\ \mu\text{W}/\mu m^2$ ($g^2(0) = 0.3$) (b) and is not visible in (c) with the correlation taken at $P_{exc} = 3.9\ \mu\text{W}/\mu m^2$ ($g^2(0) = 0.61$).

The anti-correlation between photons in consecutive pulses persists for nearly 100 ns. Santori et al. [8] measured a similar effect in micropillar cavities and in free

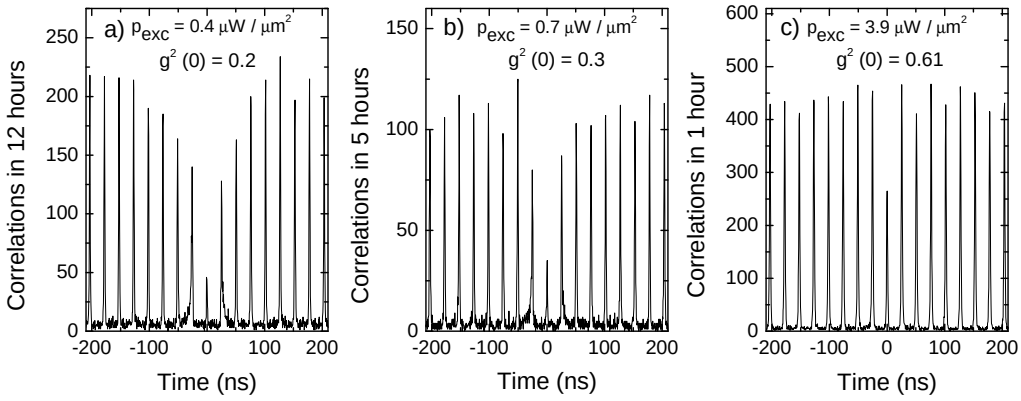

Figure 4.10: Correlation measurements performed on a dot resonant with the cavity mode. The dot is excited at 40 MHz repetition rate at $\lambda = 830$ nm. A pronounced reduction in the correlation of the peaks close to time zero is observed at low excitation power.

space, and attributed it to the presence of a second decay channel. Santori et al. proposed that the second decay channel could arise from long lived charged states or the presence of a dark exciton state. At low excitation power, the possibility exists that a laser pulse can excite the fundamental optical transition or alternatively excite an electron from the ground state to some third state (long lived charge state or dark exciton). If the electron ends up in the third state the dot cannot emit a photon until it relaxes back to the ground state. The recovery time of the correlation peaks is therefore related to the lifetime of the third state. At high excitation power Santori et al. show that the effect vanishes and attribute this to a pump power dependent mechanism which allows the fundamental optical transition to dominate the system. This is also observed in the data in figure 4.10. The similarity of the data in figure 4.10 to the data and model discussed by Santori et al. [8] leads to the conclusion that the effect seen here can most likely be attributed to the presence of a third state. Without a gate, it is however difficult to determine the nature of the long-lived state.

4.4 Purcell Effect : time-resolved measurements

Evidence of a single dot experiencing the Purcell effect was observed in the CW power dependence (figure 4.8). In this section TRPL measurements are presented indicating that the tunable cavity can influence the radiative lifetime of an exciton within the cavity. TRPL gives an immediate, unambiguous manifestation of the Purcell effect.

4.4.1 Spectral matching

The interaction between the single dot discussed in section 4.3 and the cavity mode at 4 K was investigated further. The cavity's air gap was minimised and calculated to be 2 μm using the free spectral range. This was the smallest air gap from any cavity measured in this work. The cavity length was tuned by applying 1 V to the cavity piezo in steps of 0.01 V. The dot was excited with $\lambda = 830$ nm CW excitation with a high excitation power density ($P_{exc} = 23\ \mu W/\mu m^2$) to ensure a good signal to noise ratio.

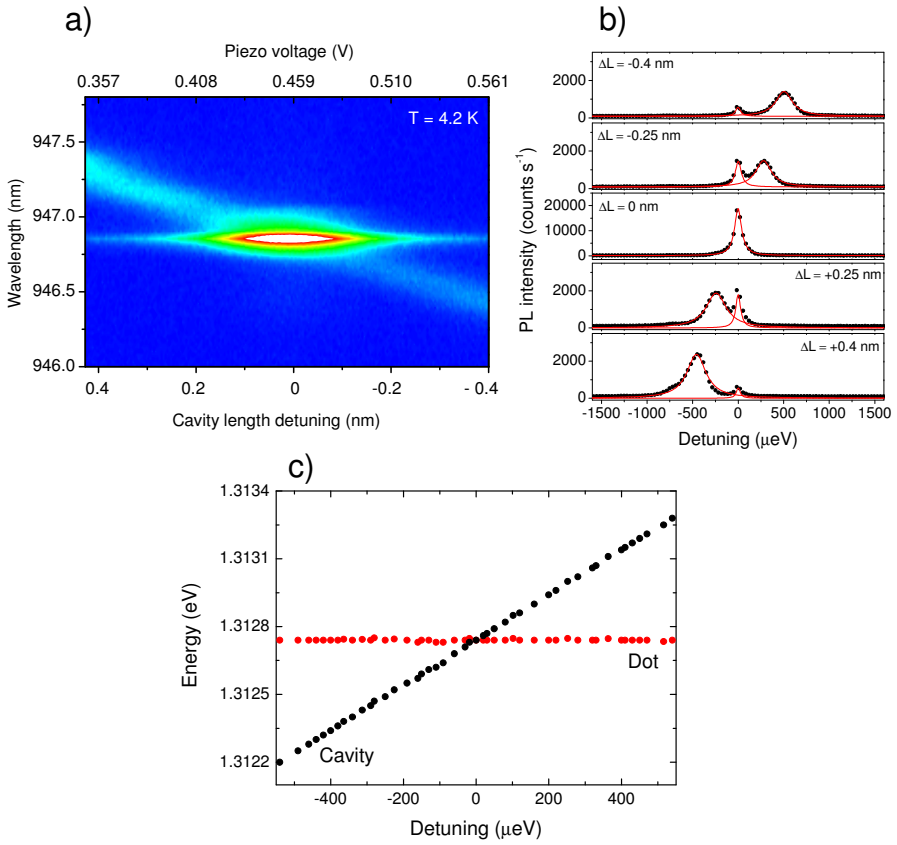

Figure 4.11: a) Colour plot showing the fundamental cavity mode, continuously tuned through resonance with a single QD exciton ($\lambda = 946.85$ nm) in sample 61004C at 4 K. The dot is excited with high CW excitation power density ($P_{exc} = 23\ \mu W/\mu m^2$). The white area in the graph corresponds to 20,000 counts on the detector and dark blue corresponds to 0 counts. The integration time for each spectrum was t = 0.5 s. b) Spectra showing the weakly coupled system at various cavity lengths, ΔL relative to the on-resonance effective cavity length ($L_{eff} = 4.75\ \mu$m). The spectra are fitted with Lorentzians (red lines) and the cavity Q-factor is 6,500. On resonance (middle curve) the PL peak intensity dramatically increases compared to the off-resonance case (top curve). c) The energy of the cavity mode and dot are plotted as a function of detuning, no anti-crossing is observed, indicating the system is in the weak coupling regime.

The spectra were recorded with an integration time of 1 second. The cavity Q was measured to be 6,500 by fitting a Lorentzian lineshape to the longitudinal mode to determine the linewidth ($\Delta\lambda_c = 0.15$ nm).

A colour plot of the recorded data is shown in figure 4.11(a). The scale on the x-axis is calculated from the manufacturer's datasheet for the piezo. The PL spectra at different cavity length detunings are shown in Figure 4.11 (b). The PL intensity on resonance is a factor of 10 greater than the intensity of the detuned cavity mode, Figure 4.11 (b). The cavity mode can be seen spectrally crossing the energy of the single dot as the cavity length is changed. Figure 4.11 (c) shows the cavity and dot PL energies plotted as a function of detuning. The cavity mode crosses through the dot energy with no observed anti-crossing, indicative of the weak coupling regime.

The radiative lifetime of the exciton resonant with the cavity at zero detuning (resonance) was measured using the photon counting techniques described in chapter 2. The excitation power density was low ($P_{exc} = 0.1\ \mu\text{W}/\mu m^2$) to ensure the transistion was not saturated.

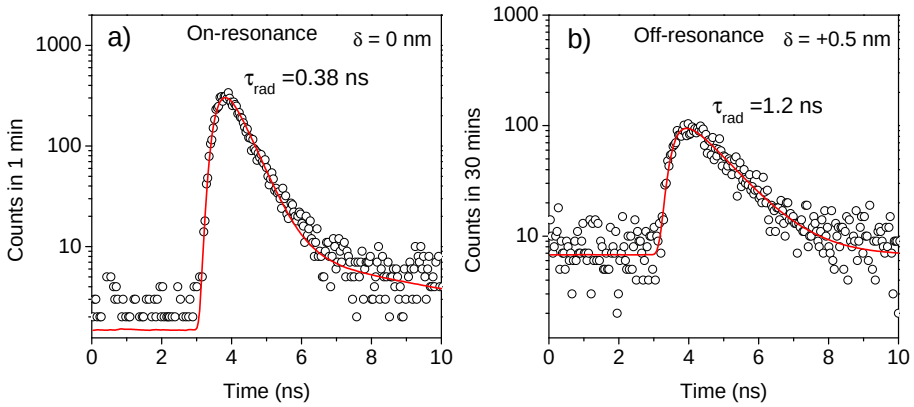

Figure 4.12: a) Time-resolved PL spectra obtained at T = 4 K from a single quantum dot in sample 61004C on exact resonance with the fundamental cavity mode (Q = 6,500). Excitation power density, $P_{exc} = 0.1\ \mu\text{W}/\mu m^2$. The red line is a bi-exponential convolution fit to the data, with a radiative lifetime of $\tau_{rad} = 0.38$ ns. b) The off-resonant radiative lifetime for a detuning of +0.5 nm. The convolution fit gives a radiative lifetime of $\tau_{rad} = 1.2$ ns.

TRPL data taken at resonance are shown in Figure 4.12 (a). The data are fitted with a bi-exponential convolution fit (discussed in chapter 2) and the radiative lifetime on resonance is $\tau_{rad} = 0.38$ ns. A weak secondary lifetime τ_2 was observed and its origin is likely a non-radiative mechanism, such as the dark exciton [7]. The secondary lifetime was not influenced by the cavity and has a value of $\tau_2 = 5.3$ ns. The cavity was detuned by +0.5 nm and the off-resonance radiative lifetime was measured to

be $\tau_{rad} = 1.2$ ns. Due to a much reduced PL signal from the off-resonant cavity, the integration time required to aquire high quality data was 30 times longer than the resonant case. The radiative lifetime for the exciton was measured for various spectral detunings and plotted in Figure 4.13. The radiative lifetime shows a clear reduction at resonance.

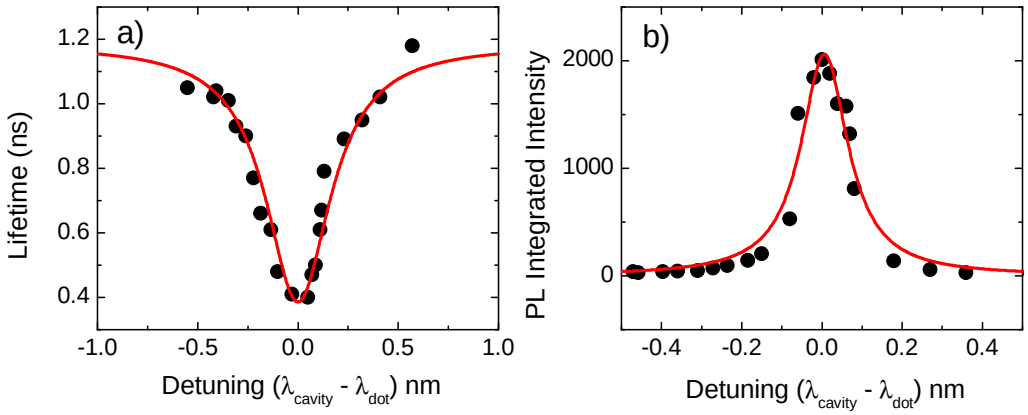

Figure 4.13: a) Measured radiative lifetime as a function of cavity mode detuning. b) Corresponding PL intensity versus cavity detuning. The data is from the same experiment as figures 4.11 and 4.12.

As discussed in chapter 1, section 1.4.2, the ratio of the free space lifetime to the cavity altered lifetime is given by,

$$\frac{\tau_{free}}{\tau_{cav}} = \frac{3Q}{4\pi^2 V_{eff}} \left(\frac{\lambda_c}{n_{eff}} \right)^3 \frac{{\Delta\lambda_c}^2}{4(\lambda_X - \lambda_c)^2 + {\Delta\lambda_c}^2} + \alpha \tag{4.2}$$

where τ_{free} is the radiative lifetime of the QD in free space, τ_{cav} is the radiative lifetime of the QD in the cavity, n_{eff} is the effective refractive index of the cavity, $\Delta\lambda_c$ is the cavity mode linewidth, λ_X is the QD emission wavelength and λ_c is the emission wavelength of the cavity. Equation 4.2 describes two decay channels. The first term gives the QD emission into the cavity mode. The second term, α, describes the QD emission into the leaky modes of the cavity [13, 77]. Re-arranging gives :

$$\tau_{cav} = \frac{\tau_{free}}{\frac{F_p \Delta\lambda_c^2}{\Delta\lambda_c^2 + 4(\lambda_X - \lambda_c)^2} + \alpha} \tag{4.3}$$

where F_p is:

$$F_p = \frac{3Q}{4\pi^2 V_{eff}} \left(\frac{\lambda_c}{n_{eff}} \right)^3 \tag{4.4}$$

In order to obtain the Purcell factor, F_p, equation 4.3 was used to fit the data in figure 4.13. A good fit was achieved by using the following parameters: $\tau_{free} = 0.85$ ns, $\Delta\lambda_c = 0.21$ nm, $F_p = 2.2$ and $\alpha = 0.71$.
The experimentally measured cavity linewidth, $\Delta\lambda_c$, was shown at the beginning of this section to be 0.15 nm (Q = 6,500). The measured linewidth is in good agreement with the value ($\Delta\lambda_c = 0.21$ nm) determined from the fit in 4.13 (a). The measured Purcell factor, $F_p = 2.2$ is the theoretical maximum value expected from the measured Q and V_{eff}.

The exciton's free space lifetime can be estimated from its emission wavelength. The exciton emits at $\lambda = 946.85$ nm (1.31 eV). According to a statistical study by Dalgarno et al. [7] of over 80 InGaAs quantum dots from a sample grown with the same MBE protocol, the statistically expected free space lifetime for an X^0 emitting at 1.31 eV is 0.8 ± 0.1 ns. In figure 4.13 when the cavity is resonant with the exciton, the radiative lifetime is much shorter than 0.8 ns, demonstrating an accelerated recombination rate. When the cavity is +0.5 nm detuned the lifetime is much longer, indicating decelerated recombination.

An interesting feature in the data in figure 4.13 is that the measured radiative lifetime is increased above the value expected in free space (≈ 0.85 ns) when the cavity is spectrally detuned by ± 0.5 nm from the exciton.

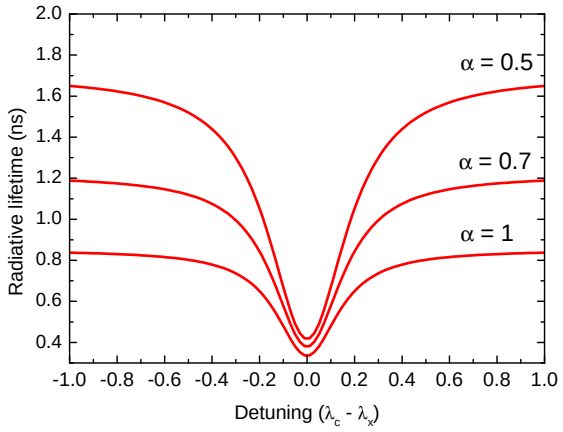

Figure 4.14: Simulated values for τ_{rad} as a function of detuning. Three different values of α are used, with a constant Purcell factor $F_p = 2.2$. The leaky modes increase the off-resonance radiative lifetime with increasing α. The free space lifetime is 0.85 ns which is the off-resonant lifetime when $\alpha = 1$.

At small detunings the majority of the emitted photons are funnelled into the fundamental cavity mode via the Purcell effect. However at larger detunings, the first term in equation 4.2 decreases and the second term, α, contributes to a greater degree. The photon density of states of the leaky modes in the tunable cavity is less than in free space (hence the suppression of the spontaneous emission rate at large detunings). However in other microcavity systems this is not always the case e.g. micropillars often show off-resonance lifetimes comparable with free space lifetimes [77] where $\alpha = 1$ due to leaky modes in the lateral direction. Bayer et al. demonstrated that they could suppress the off-resonant spontaneous emission rate of an exciton within a micropillar by coating the pillars in gold [77], suppressing the coupling to the leaky modes.

In the work described here, equation 4.3 was used to simulate the effect α has on the cavity-altered lifetime as a function of detuning. The fixed parameters used in the simulations were taken from the fit to the experimental data in 4.13 (a) ($\tau_{rad} =$ 0.85 ns, $F_p = 2.2$ and $\Delta\lambda_c = 0.21$ nm). Figure 4.14 shows the simulated effect of α on the cavity-altered lifetime from an exciton in a generic microcavity. The simulations show that the effect of reducing α is to increase the off-resonance radiative lifetime which has very little effect to the on-resonance lifetime.

In the half symmetric tunable cavity the curved mirror strongly confines the beam laterally, reducing the exciton coupling to the continuum of lateral leaky modes and thereby lowering the α parameter to ≈ 0.7 (middle curve in 4.14).

The α parameter is inherent to the cavity design. Experimentally the low α value determines the degree of off-resonant suppression. In the tunable cavity this limits the measurements that can be performed at detunings greater than $\pm$ 0.5 nm, due to lack of PL signal. At larger detunings the exciton peak PL intensity becomes too weak to be useful for correlation or time-resolved PL measurements.

4.4.2 Spatial matching

Equation 4.2 assumes that the quantum dot is located at the exact antinode of the electric field. The cavity mirrors were designed (chapter 3) to ensure that the dot layer is as close to the antinode in the vertical direction as possible. However due to the self-assembled growth process, the dots are randomly spatially positioned over the sample, rendering it challenging to find a single dot which is located at the exact antinode position in the xy plane. The tunable cavity can be used to move the dot sample relative to the curved mirror (chapter 3) to place a single quantum dot at the maximum of the electric field. This is of major benefit when studying the Purcell effect as it allows maximal coupling to the electric field to be achieved with relative ease.

The collection spot was aligned with the centre of the curved mirror using the methods discussed in chapter 3. The cavity mode was then tuned over several nanometres to search for a dot which interacts most strongly with the cavity mode. Once a dot was selected, the bottom half of the cavity was scanned in the x direction by applying 0-150 V in 1 volt steps to the x piezo. The collected PL intensity is plotted as a function of the voltage applied to the x piezo. This procedure scans the dot through the optimal electric field position within the mode in the x direction. The optimal position is the voltage (spatial location) at which the dot is at its most intense. This procedure is then repeated in the y direction. A co-ordinate system (V_x ,V_y) gives the optimum position for the selected dot in the xy plane. A complication arises in the alignment procedure due to a small degree of skew between the two mirrors. Every lateral displacement alters the cavity length and therefore it must be corrected by applying a voltage to the z piezo positioner to keep the cavity mode exactly on resonance with the quantum dot. Spectral resonance with the dot was maintained by monitoring the PL in real time on the spectrometer and every time the dot sample was moved laterally the cavity length was altered to maximise the PL signal.

The radiative lifetime of the same dot discussed in sections 4.3 and 4.4.1 was measured as a function of applied voltage to the y scanner axis. The same cavity and dot as in sections 4.3 and 4.4.1 were used. A low excitation power density (P_{exc} = 0.1 $\mu W/\mu m^2$) was used to excite the dot and data were taken with an integration time of 100 seconds. Figure 4.15 shows data for various spatial detunings in the y direction. The y displacement is calculated by converting from applied voltage to physical distance (μm) using the scanner calibration discussed in chapter 3.

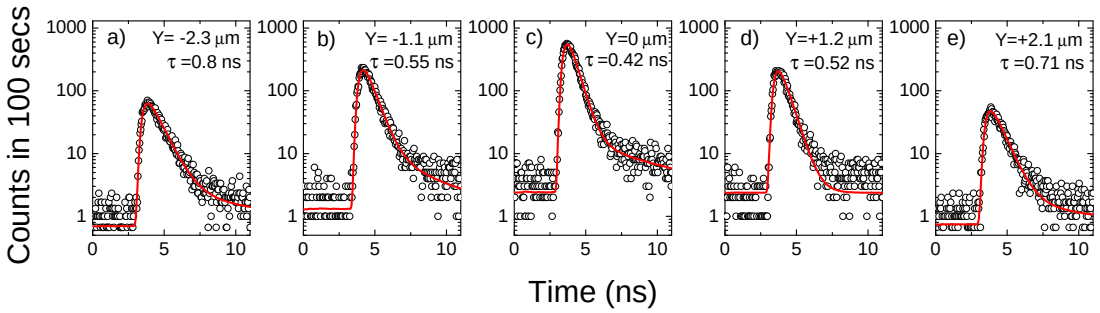

Figure 4.15: Time-resolved PL spectra at T = 4 K from the same dot in sample 61004C described in section 4.4.1. The data shows the effect on the radiative lifetime of displacing the dot laterally from the centre of the cavity mode. a) Y = -2.3 μm and the radiative lifetime is 0.8 ns. c) Y = 0 μm and the radiative lifetime is 0.42 ns.

The data in figure 4.15 are fitted with bi-exponential fits from the convolution of

the system's response as discussed in chapter 2. At large spatial detuning ((a) and (e)) the radiative lifetime is approximately 0.80 ns. The radiative lifetime decreases as the dot is moved spatially closer to the centre of the cavity mode, with the shortest radiative lifetime of 0.42 ns achieved at the centre of the cavity mode (figure 4.15 (c)). The experiment was repeated for the x axis and both the x and y data are shown in figure 4.16.

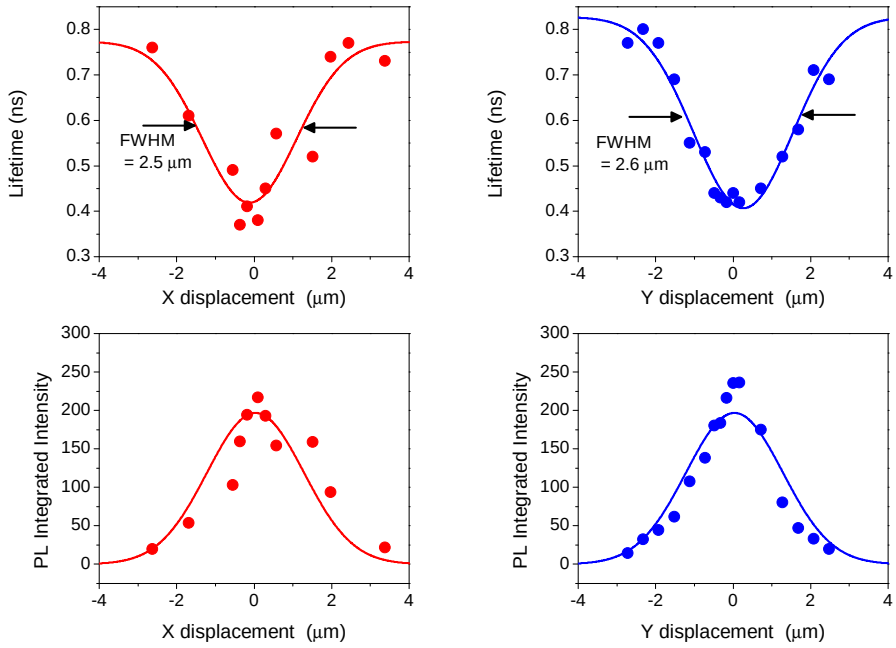

Figure 4.16: QD radiative lifetime measurements and corresponding PL intensity increase as the dot was laterally displaced from the maximum electric field in the cavity. A Gaussian fit to the data with a FWHM = 2.5 μm is shown (red and blue lines).

The measured radiative lifetime and corresponding integrated intensity from the dot on exact spectral resonance with the cavity are shown in Figure 4.16. The shortest radiative lifetime was measured to be 0.38 ns when the dot was positioned at the exact antinode of the electric field, corresponding to zero displacement in the plots in figure 4.16. The plots clearly indicate the importance of spatial matching within the microcavity, to ensure an optimal interaction with the cavity mode.

The plots include Gaussian fits with a FWHM of 2.5 μm. The 1/e value of the Gaussian fit is $\Delta X = 3.3$ μm. The experiment probes the intensity of the electric field experienced by the dot at different spatial locations within the optical mode. The measured cavity mode beam waist at the dots can be extracted from the data in figure 4.16 using,

$$\omega_0 = \frac{\Delta X}{\sqrt{2}} = 2.3\,\mu m \tag{4.5}$$

where ΔX is the 1/e value from the Gaussian fit to the data.

The calculated beam waist (using equation 3.6) at the planar mirror for a cavity length of 4.75 μm and a curved mirror with a radius of curvature R = 120 μm is ω_0 = 2.65 μm. The measured beam waist (ω_0 = 2.3 μm) is therefore in good agreement with the value predicted from equation 3.6.

4.5 Calculating the mode volume

4.5.1 Cavity length

The total optical cavity length for the cavity used in sections 4.3 and 4.4 was calculated to be L_{eff} = 9.4 μm from the measured free spectral range (FSR = 50 nm). The physical cavity length can be deduced by calculating the effective refractive index for each component within the cavity. Figure 4.17 shows a schematic of the layers within the cavity and the calculated total physical length of 4.75 μm. The physical penetration into the semiconductor and dielectric mirrors was calculated using equation 3.3 to be 1.56 μm and 0.55 μm, respectively. The total contribution to the effective cavity length by penetration into the cavity mirrors is 2.11 μm.

The limiting factor in achieving a minimum mode volume within the tunable cavity is the length of the air gap separating the two mirrors. The air gap was estimated to be ≈ 2.37 μm by subtracting the other calculated physical lengths from the total measured cavity length. Surface profile measurements (chapter 3) indicate the depth of the curved mirror is ≈ 0.5-1 μm. The remaining 1-2 micron air gap is attributed to tiny particles of dust, trapped between the two mirrors, or to a slight skew between the mirrors.

4.5.2 Cavity mode volume

In the previous section, the beam waist at the planar mirror was determined experimentally to be ω_0 = 2.3 μm. To estimate the cavity mode volume, the beam is assumed to have negligible divergence over the cavity length ($\omega_0 \approx \omega_1$), which is justifiable for a short cavity (see chapter 3 section 3.7.2).

The mode volume can be approximated by,

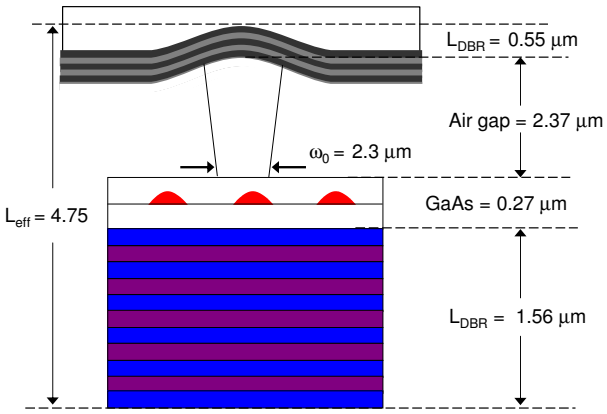

Figure 4.17: Schematic showing detailed calculated dimensions of the optical cavity. All dimensions are physical lengths. The effective cavity length is 4.75 μm and includes the cavity air gap, dot layer and penetration into both mirrors.

$$V_{eff} = \pi \left(\frac{\omega_0}{2}\right)^2 L_{eff} \tag{4.6}$$

where $L_{eff} = 4.75$ μm (physical length). The mode volume is estimated to be $V_{eff} = 19.7$ μm^3. Although 19.7 μm^3 appears to be a large mode volume for a microcavity, compared to nanophotonic crystals, it is much smaller than similar non-monolithic cavity structures used for atom/cavity experiments [78] and on a par with large diameter micropillar cavities.

With an estimate of the mode volume, the effective refractive index of the cavity can be calculated by re-arranging equation 4.4,

$$n_{eff} = \frac{\lambda}{\sqrt[3]{\frac{4\pi^2 V_{eff} F_p}{3Q}}} = 2.13, \tag{4.7}$$

using $V_{eff} = 19.7$ μm^3, Q = 6,500, $F_p = 2.2$ and $\lambda = 950$ nm. The calculated value of $n_{eff} = 2.13$ is in the expected range, between n = 1 (air) and n = 3.5 (GaAs).

The Purcell effect could be increased by using super-mirrors to obtain a much higher Q. Having an estimate of n_{eff} is useful for calculating the predicted Purcell effect from equation 4.4 for a given Q and V_{eff}.

4.6 Coupling transverse modes to a single dot

The tunable cavity also enables the transverse modes for a given fundamental mode to be coupled to the quantum dot. These modes can provide some additional insight into the electric field at the dot layer. The higher order modes within the cavity demonstrate different interactions with the dots, depending on the electric field distribution for the mode.

A curved mirror cavity was established at 4 K by aligning the collection optics to collect light from as close to the centre of a curved mirror as possible. The PL profiles of the fundamental, first and second transverse modes were recorded using the spectrometer and are shown in figure 4.18.

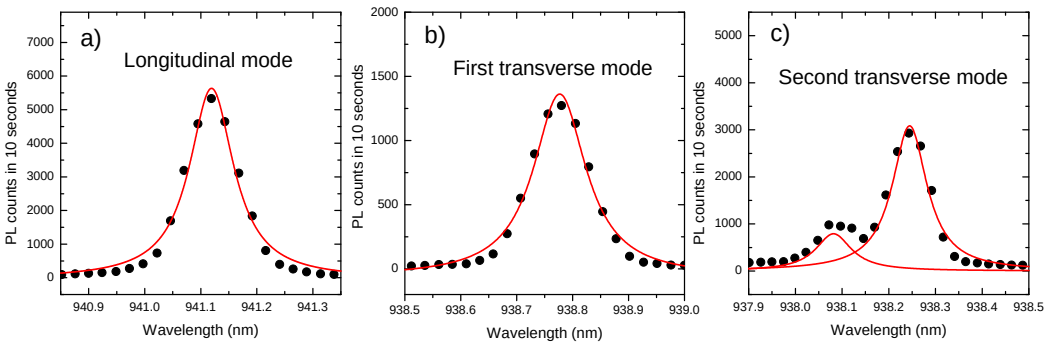

Figure 4.18: Cavity mode profiles at 4 K. The cavity was excited with a CW 830 nm laser at $P_{exc} = 10\ \mu W/\mu m^2$. a) The fundamental mode profile has a linewidth of 0.073 nm (Q = 12,600) b) The first transverse mode has a linewidth of 0.10 nm (Q = 9,380) c) The profile of the second transverse mode shows a splitting (0.18 nm).

The modes are fitted with Lorentzian lineshapes (red lines). The Q-factors of the fundamental mode and the first transverse mode are 12,600 and 9,380 respectively. The larger Q for the fundamental mode (compared to Q = 6,500 in section 4.4) was a result of a slightly longer cavity length ($L_{eff} = 9\ \mu$m). The profile of the second transverse modes shows a 0.18 nm spectral splitting, fitted with two Lorentzians both with a FWHM of 0.078 nm.

The interaction between a single exciton and the fundamental, first and second order cavity modes was investigated by tuning each mode through resonance with a single exciton. Figure 4.19 shows colour plots of these mode's tuning through the single exciton emission at 940.30 nm.

For the fully aligned cavity, collecting the emission from the dot at the centre of the curved mirror, an increase in brightness from the dot on resonance was observed, as

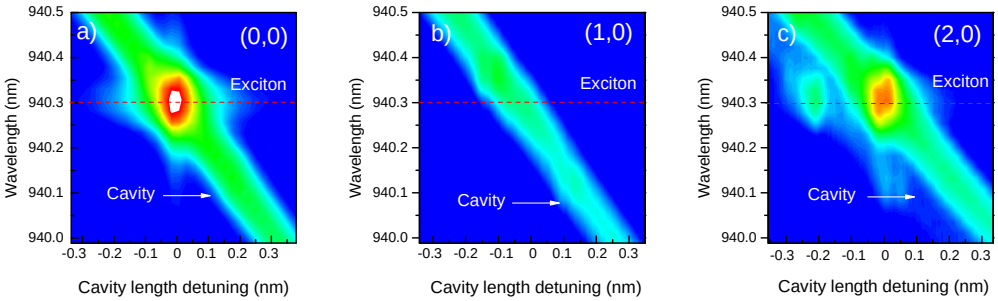

Figure 4.19: PL from an exciton in sample 61004C within the tunable cavity. The colour plots are all on the same logarithmic intensity scale, white areas are 15,000 counts and dark blue is zero counts. An integration time 0.5 seconds is kept constant for each plot. a) The interaction of (0,0) with the dot. An increase of intensity on resonance is observed due to the Purcell effect. b) The first transverse mode (1,0) shows minimal interaction with the exciton. c) The second transverse mode (2,0) is split and shows a more involved interaction with the exciton.

expected from the longitudinal mode (0,0). The plots were taken with high excitation power ($P_{exc} = 10\ \mu\text{W}/\mu m^2$) due to the PL collected from the transverse modes being weak in comparison to the longitudinal mode. Strikingly the first transverse mode (n + m = 1) showed very little interaction with the quantum dot, (b). The second transverse mode (n + m = 2) was subsequently tuned through resonance with the quantum dot and an increase in emission intensity was observed.

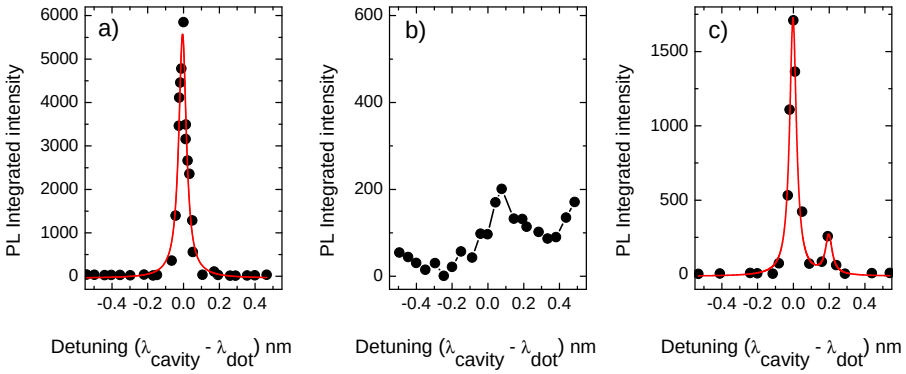

Figure 4.20: Integrated intensity for the exciton as a function of detuning with a) the fundamental mode b) the first transverse mode and c) the second transverse mode.

The integrated intensity of the exciton as a function of detuning for the three cavity modes is shown in figure 4.20. The integrated intensity of the exciton as a function of detuning of the longitudinal mode (a) shows a single Lorentzian lineshape. However

the first transverse mode (b) shows only a small increase in intensity near resonance with the exciton. When the second transverse mode was resonant with the exciton (c), the maximum integrated intensity was lower than in (a) by a factor of 3.5. Also visible in figure 4.20 (c) is the small increase in PL intensity from the exciton when the smaller peak of the second transverse mode is resonant with it.

4.6.1 Radiative lifetime alterations

The radiative lifetime of the exciton was measured with the fundamental and second transverse modes at various spectral detunings, figure 4.21. The excitation power was 0.1 μW/μm^2.

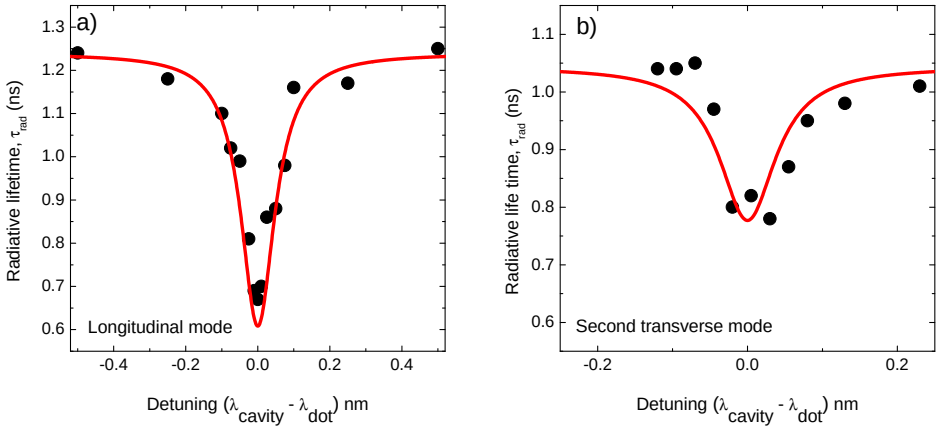

Figure 4.21: a) The lifetime alteration by the interaction of (0,0) with the exciton. b) Lifetime alteration by (2,0) with the same exciton. The interaction with (1,0) was so weak that valid lifetime measurements could not be made. The data was taken from the same experiment as the data in figure 4.19.

When the fundamental cavity mode was on resonance with the exciton, the radiative lifetime was $\tau_{rad} = 0.67$ ns. The off-resonance radiative lifetime was 1.2 ns, due to the suppression of the spontaneous emission rate as discussed in section 4.4. A good fit to the data in figure 4.21 (a) was obtained using equation 4.3 with parameters : $\tau_{free} = 0.88$ ns, $\Delta\lambda_c = 0.08$ nm, $F_p = 1.11$ and $\alpha = 0.71$. The data in figure 4.21 (b) shows a radiative lifetime of 0.77 ns when resonant with the second transverse mode. A good fit to data in (b) was obtained using equation 4.3 with parameters : $\tau_{free} = 0.88$ ns, $\Delta\lambda_c = 0.078$ nm, $F_p = 0.51$ and $\alpha = 0.84$.

The interaction between the first transverse mode (1,0) and the exciton was so weak, that only a tiny rise in intensity was observed whilst tuned to the exciton energy. The lifetime was measured for 8 hrs to get enough signal to accurately fit to

the data. The measured on-resonance lifetime was $\tau_{rad} = 0.84$ ns.
The Purcell effect obtained from the fit to the data in figure 4.21 (a) is $F_p = 1.11$, this is not as large as previously measured for a different dot ($F_p = 2.2$, section 4.4). The reduction of F_p is likely due to the increased mode volume due to the longer cavity length of $L_{eff} = 9$ μm. The calculated Purcell factor for a cavity length of 9 μm and Q = 12,600 is $F_p = 1.21$. This agrees well with the measured value in figure 4.21 of $F_p = 1.11$.

The reduction in the Purcell effect when the second transverse mode is resonant with the exciton could be due to a lesser electric field intensity associated with the second transverse mode.

4.6.2 Calculated electric field profiles

To understand why the first transverse mode shows no interaction with the exciton the electric field profile within the cavity was simulated. A set of spatial eigenmodes are associated with the cavity, either Hermite-Gaussian (HG) or Laguerre-Gaussian modes (LG) (depending on the cavity mode symmetry). Physically these eigenmodes describe electric field distributions within the cavity. Although both mode sets (HG and LG) are possible within the cavity, the results in figure 4.19 suggest that the HG modes are the predominant set. This is more clearly illustrated by calculating the HG functions, equations (4.8 - 4.10). For simplicity only the x direction is considered, as the distribution is the same in y.

$$E_0(x) = \left(\frac{2}{\pi\omega_0^2}\right)^{1/4} \exp\left[-\left(\frac{x}{\omega_0}\right)^2\right] \tag{4.8}$$

$$E_1(x) = \left(\frac{2}{\pi\omega_0^2}\right)^{1/4} \frac{2x}{\omega_0} \exp\left[-\left(\frac{x}{\omega_0}\right)^2\right] \tag{4.9}$$

$$E_2(x) = \left(\frac{2}{\pi\omega_0^2}\right)^{1/4} \left[\frac{4x^2}{\omega_0^2} - 1\right] \exp\left[-\left(\frac{x}{\omega_0}\right)^2\right] \tag{4.10}$$

where E_0, E_1, E_2 describe the electric field profile at the beam waist of the fundamental, first transverse and second transverse modes respectively. ω_0 is the mode beam waist size.

The Hermite - Gaussian functions are plotted in Figure 4.22 for the fundamental (black), first transverse (red) and second transverse modes (blue). The beam waist used in the calculation is $\omega_0 = 2.3$ μm as measured in section 4.4.2. This gives the expected Gaussian profile. It is clear from the calculated electric field profile figure

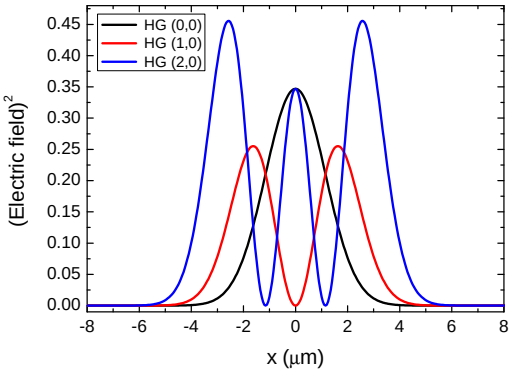

Figure 4.22: The Hermite-Gaussian functions in x for the fundamental (black), first transverse (red) and second transverse (blue) modes. The beam waist, ω_0 is 2.3 μm.

4.22 why the experimentally measured interaction between the exciton (at $x = 0$) and the first transverse mode is so weak. The calculated electric field intensity at $x = 0$ is zero for the HG(1,0) mode (red line). The fact that the first transverse mode does not interact with the dot demonstrates that the dot is located very precisely at the antinode position.

The second transverse mode has an similar electric field intensity at the dot position to the fundamental mode and therefore should show a similar dot/cavity interaction. However it was seen in figure 4.21 that the second transverse mode shows a reduced Purcell effect relative to the fundamental mode. It is not clear why this should be the case, although one possibility is that the electric field profile for the second transverse mode is a mixture of the HG and LG mode sets.

4.7 Ensemble dot strong coupling: evidence

So far this chapter has considered in detail a single quantum dot, weakly coupled to the cavity mode. At present the cavity mirrors do not have high enough reflectivity to enable the strong coupling regime to be achieved with a single dot. However in this section data is presented which suggests that large ensembles of quantum dots within the cavity may be achieving a strong coupling regime. In atomic physics strong coupling has been achieved for large ensembles of atoms within high finesse optical cavities [73]. The vacuum Rabi splitting is increased by a factor of $\sqrt{N}$ (where N is the number of atoms within the cavity mode) compared to the expected Rabi splitting with a single atom. However in solid state physics this collective effect has never been reported. This section presents experimental evidence of an ensemble of quantum dots strongly coupled to the cavity mode.

4.7.1 Curved mirror cavity

The mirrors used in the previous sections of this chapter were used to form a cavity. A curved mirror was located using the techniques discussed in chapter 2. The dots within a high density sample ($\approx$ 500 dots/μm^2) from wafer 61004C were excited at 830 nm with CW excitation at a high power density of 20 μW/μm^2. The cavity mode linewidth was 280 μeV, giving Q = 5,000 at a cavity length of 5.1 μm, which is slightly lower than that measured in section 4.3 for a similar cavity length. The cavity air gap was shortened by $\approx$ 800 nm in steps of $\approx$ 8 nm and the PL spectra recorded as a function of cavity length detuning, figure 4.23 (a).

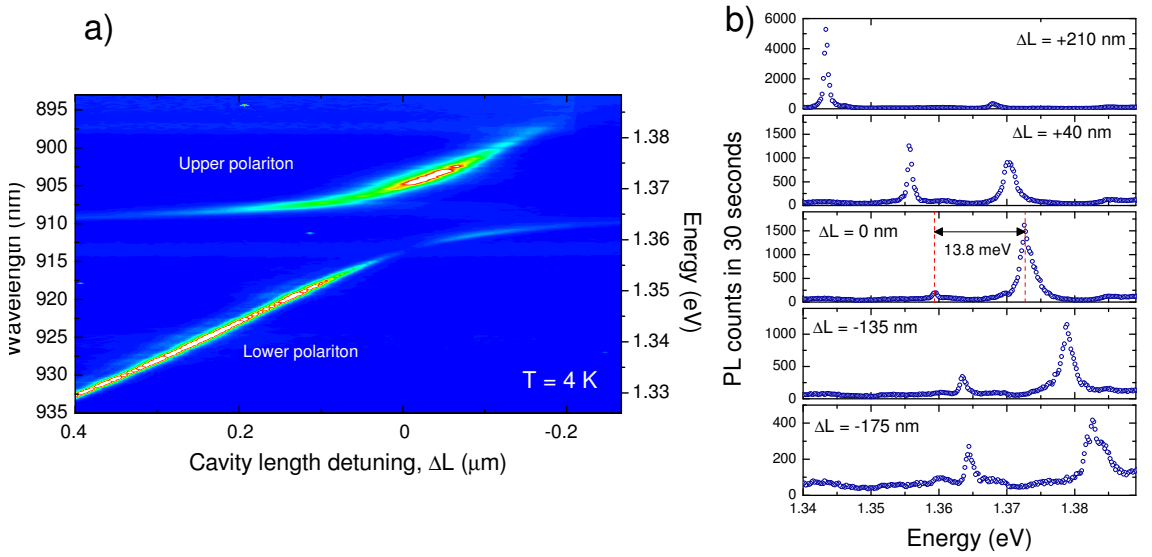

Figure 4.23: a) Colour plot showing the anti-crossing observed in the PL (P_{exc} = 20 μW/μm^2) spectrum between the cavity mode and a spectrally broad ($\approx$ 1.7 meV) spectroscopic feature at E = 1.365 eV at 4 K. White corresponds to 3,000 counts and blue, zero counts on a linear scale. b) Spectra from the contour plot at various cavity length detunings close to resonance. The low energy peak is the lower polariton and the high energy peak is the upper polariton.

The cavity mode is shown in figure 4.23 (a) interacting with a feature in the PL spectrum. Figure 4.23 (b) shows the PL spectra for various cavity length detunings. Strikingly, a distinct anti-crossing (a signature of strong photon/exciton hybridisation) is observed between the cavity mode and the PL feature at E = 1.365 eV (910.7 nm). At large detuning the emission from the feature is weak ($<$ 50 counts s^{-1}). The PL

peak at 1.365 eV (910.7 nm) is emission from the quantum dots emitting around 1.365 eV (910.7 nm), as seen in chapter 2, figure 2.8.

In order to verify that the PL feature was emission from a large ensemble of quantum dots emitting close to 1.365 eV the sample PL was measured in free space at 4 K. The sample was excited with a power density of 1 $\mu W/\mu m^2$ and recorded on the spectrometer's CCD camera using the 300 g/mm grating. A lens with NA = 0.55 (Thorlabs C230TM-B) was used to probe the sample. The lens gives a diffraction limited collection spot size of ≈900 nm. An aperture was placed at the top of the microscope to allow the beam diameters to be reduced to increase the spot size at the dot layer. The aperture diameter was reduced to 2 mm, increasing the collection area of the lens by reducing the NA to 0.2. The PL was recorded with an integration time of 30 seconds.

The collected PL from the sample in free space in both configurations is shown in figure 4.24 (a) and (b).

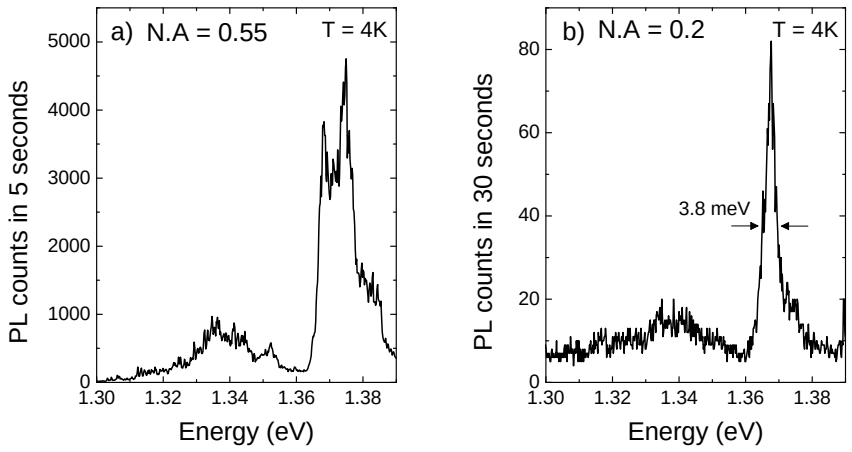

Figure 4.24: a) The collected PL from sample 61004C in free space at T = 4 K (P_{exc} = 1 $\mu W/\mu m^2$), using a lens with N.A = 0.55. b) PL collected from the same area of sample 61004C, using a pinhole aperture to reduce the effective NA = 0.2. A noticeable narrowing in the peak at 1.367 eV is observed.

The PL spectra in figure 4.24 (a) and (b) show a high concentration of quantum dots emitting at 1.367 eV. It is likely that the PL from the dots at 1.367 eV is the origin of the spectroscopic feature that demonstrates anti-crossing with the cavity mode in the PL spectra (figure 4.23).

In section 4.4.2 the cavity mode beam waist was experimentally measured to be 2.3 μm. The cavity mode's beam waist is larger than the beam waist of the light focussed by the lens (NA = 0.55), therefore a greater number of dots are excited

within the cavity than in the free space system.

A collection spot size of 2.1 μm is estimated in the configuration with effective NA = 0.2. A spot size of 2.1 μm in free space is closer to the FWHM of the beam (2.5 μm) within the cavity. Figure 4.24 (b) shows the PL spectra collected using the 2.1 μm collection spot size. The peak at 1.367 eV has a narrower linewidth (3.8 meV) and a more Gaussian profile than in figure 4.24 (a). However the FWHM of the peak in 4.24 (b) is twice the width of the peak observed in the cavity and almost 2 meV higher in energy. Despite these discrepancies it seems likely that the peak due to a high density of dots observed at 1.367 eV in free space is the feature that couples with the cavity mode. The maximum number of dots within the cavity mode with the high dot density sample is about 1000 dots (calculated using a beam waist of ω_0 = 2.3 μm).

To add further evidence that the PL feature at 1.367 eV is due to a high density of quantum dots the PL from a low dot density sample was measured in free space. The sample was excited at 830 nm at a power density of 0.5 $\mu W/\mu m^2$.

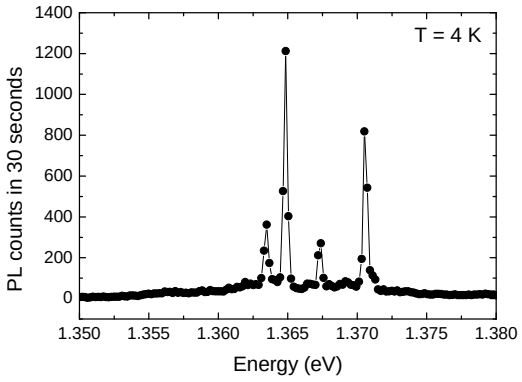

Figure 4.25: PL from a low density sample from wafer 61004C in free space at 4 K.

The collection spot size was estimated to be 900 nm using the 0.55 NA lens (C230TM-B). The PL collected is shown in figure 4.25. The PL lines from individual dots are visible in figure 4.25. The reduced dot density allows individual lines to be resolved. This confirms that the PL emission at 1.367 eV is from a high density ensemble of quantum dots.

4.7.2 Fitting to the anti-crossing

To investigate further the interaction between the cavity mode and the ensemble of quantum dots, Lorentzian lineshapes were fitted to the data presented in figure 4.23. The peak energies were obtained from the fits as a function of detuning. The peak

values in figure 4.26 (a) are fitted with the calculated values using the 2 x 2 coupling matrix method described in chapter 1. The change in cavity length is not completely linear with voltage therefore the cavity energy was deduced from the energy values using the coupling matrix. A good fit was obtained with the fit parameters $\hbar$V = 7 meV (the matrix coupling element) and E_x = 1.365 eV (the uncoupled energy of the array of dots), with the Rabi splitting, $\hbar\Omega$, given by [79],

$$\hbar\Omega = 2\sqrt{(\hbar V)^2 - \frac{1}{4}(\gamma_c - \gamma_x)^2} \tag{4.11}$$

where γ_c and γ_x are the uncoupled linewidths of the cavity and the array of dots peak respectively. A Rabi splitting of $\hbar\Omega$ = 13.9 meV, is calculated from equation 4.11, however it is well known that the observable splitting depends on the how it is probed (transmission, reflection or photoluminesence) [80]. The PL splitting, $\hbar\Omega_{PL}$, is related to the actual normal mode splitting [80],

$$\hbar\Omega_{PL} = \sqrt{2\hbar\Omega\sqrt{(\hbar\Omega)^2 + 4\Gamma^2} - (\hbar\Omega)^2 - 4\Gamma^2} \tag{4.12}$$

where $\Gamma = \frac{\gamma_c + \gamma_x}{2}$. At large detunings ($\delta$ = -50 meV) the uncoupled cavity linewidths, γ_c = 0.3 meV and γ_x = 1.7 meV are obtained from Lorentzian fits. The PL splitting is calculated from equation 4.12 to be 13.8 meV, close to the actual normal mode splitting ($\hbar\Omega$ = 13.9 meV).

The integrated intensity of the upper and lower peaks as a function of detuning was also extracted from the Lorentzian fits, Figure 4.26 (b). The cavity mode PL is most intense at large detunings. Close to resonance the ensemble of dots PL increases in intensity, with the two peaks equal in intensity at δ = -5 meV. This is very similar to the observed behaviour with a strongly coupled quantum well microcavity system [81].

It was shown in section 4.2 that emission into the cavity mode occurs, even when the cavity is significantly detuned from the dot emission. The mechanism by which this occurs is not entirely understood, but is possibly due to phonon emission. If a dot can emit a photon and a phonon so that the emission energy is tunable over a large range of energy, it is possible that a large percentage of the dots emit at almost the same emission energy (1.365 eV), each dot requiring a different phonon. Assuming that this is possible, the expected collective Rabi splitting can be calculated. The maximum number of dots within the cavity mode with the high dot density sample is about 1000 dots (calculated using a beam waist of ω_0 = 2.3 μm). A Rabi splitting of Ω = 130 μeV was observed in the PL spectra from a single InGaAs quantum dot by Hennessy et al [30]. Therefore the maximum expected splitting due to an ensemble

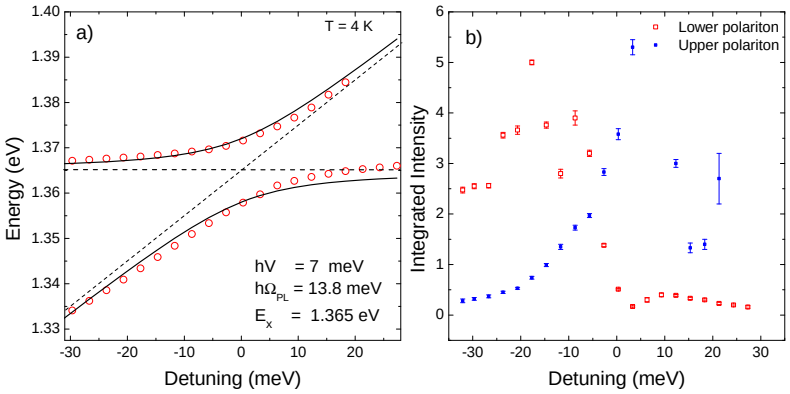

Figure 4.26: Analysed data from the spectra that constitute the colour plot in figure 4.23. a) The red dots indicate the measured spectral peak positions for the two peaks. Calculated peak positions are shown as solid black lines. The dashed black lines show calculated peak positions in the weak coupling regime. Spectral PL splitting is 13.8 meV. b) Integrated intensity of the upper (blue) and lower polariton (red) measured from the PL spectra.

effect is estimated to be $\sqrt{N}\Omega = \sqrt{1000} \times 130\ \mu\text{eV} = 4.1$ meV. This is about one third of the observed PL splitting of 13.8 meV.

4.7.3 Planar cavity

A planar mirror cavity mode was established by moving the collection spot off the curved mirror and focusing onto the planar mirror cavity region formed between adjacent curved mirrors. The planar cavity mode linewidth, $\Gamma_c = 3.5$ meV is large compared to the curved mirror cavity mode. The corresponding cavity Q is 370. Although the planar cavity linewidth is too broad to interact with a single quantum dot, it is a close match to the linewidth (3.8 meV) of the ensemble of dots.

The planar cavity mode was tuned through resonance with the ensemble of dots as described in section 4.7.1. The dots were excited using the CW laser with a power density of 20 $\mu\text{W}/\mu m^2$. The integration time for each spectra was 60 seconds. Lorentzian fits were used to obtain the peak energy values as a function of detuning.

A distinct anti-crossing between the cavity mode and the dot PL is visible in figure 4.27 (a). The peak energy values are presented in figure 4.27 (b) with the fit from the 2 x 2 transfer matrix method (black line). The best fit was achieved using the parameters Ex = 1.365 eV and $\hbar$V = 7.8 meV. The PL spectral splitting is $\hbar\Omega_{PL}$ = 15.6 meV. This 13% increase in the observed spectral splitting compared to the curved mirror cavity, is most likely due to the improved linewidth matching between the cavity mode and ensemble of dots (see chapter 1, section 1.5).

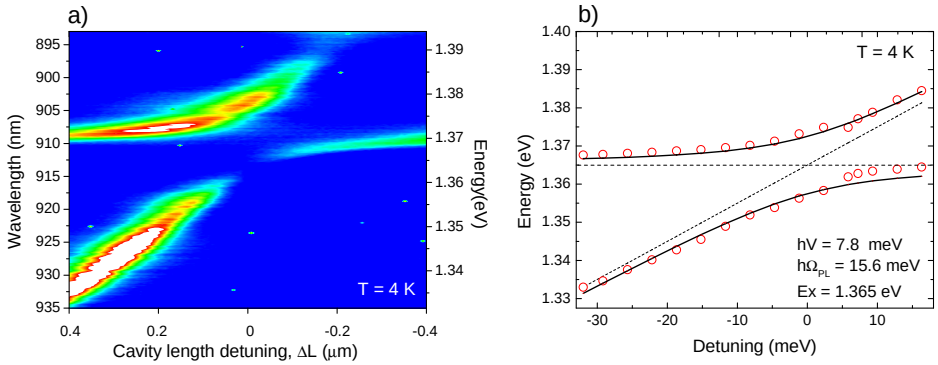

Figure 4.27: a) Colour plot showing the anti-crossing observed in the PL (P_{exc} = 20 $\mu W/\mu m^2$) spectra between the planar cavity mode and a spectrally broad ($\approx$ 1.7 meV) spectroscopic feature at E_x = 1.365 eV, at 4 K. White corresponds to 900 counts and blue to zero counts on a logarithmic intensity scale. b) Red dots indicate the measured spectral peak positions for the two peaks. Calculated peak positions are shown as solid black lines. The dashed black lines show calculated peak positions in the weak coupling regime. The calculated splitting, $\hbar\Omega_{PL}$ = 15.6 meV, is 13% greater than the splitting observed with the curved mirror cavity mode (figure 4.26).

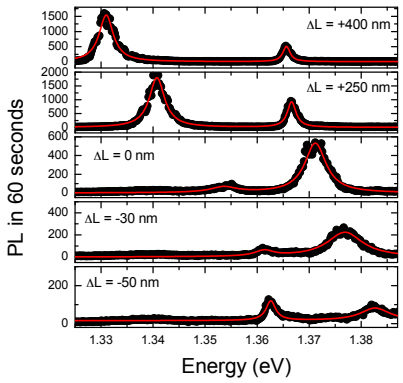

Figure 4.28: Selected spectra from the colour plot in figure 4.27 at various cavity length detunings fitted with Lorentzian lineshapes (red lines). Anti-crossing is observed in the PL spectra between the planar cavity mode and an ensemble of quantum dots with a observable splitting of 15.6 meV (middle spectrum). The data was taken at 4 K with the same experimental conditions as in figure 4.27.

Selected spectra from the colour plot in figure 4.27 at various cavity length detunings are shown in figure 4.28. The cavity mode is shown on the left in the top spectrum. The middle spectrum shows the Rabi splitting of 15.6 meV. The Lorentzian fits were used to extract the the linewidths and integrated intensities from each spectrum and are plotted as a function of detuning in figure 4.29. The integrated intensities are equal at δ = -10 meV, similar behaviour to the curved mode cavity data in figure 4.26 (b). The intensity of the lower polariton is at a maximum at δ = -25 meV, this is due

to a large number of dots emitting in this region. The linewidths of both peaks also cross over close to zero detuning (-5 meV).

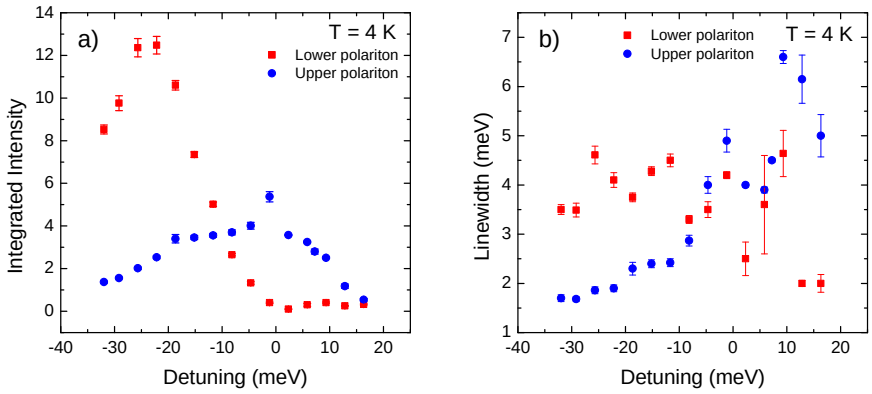

Figure 4.29: a) The integrated intensity for the upper and lower polaritons, obtained from Lorentzian fits to the raw data in figure 4.27 (a). The intensities are equal at δ = -10 meV. b) The measured linewidths for the upper and lower polaritons. The linewidths are equal at δ = -5 meV.

4.8 Summary

This chapter presented results from a single quantum dot within a fully tunable microcavity at 4 K. The presence of a broad background emission which drives the cavity mode when it is spectrally detuned from any dots was observed and found to saturate at much higher excitation power than the spectrally detuned dots.

The cavity was spectrally tuned to resonance with single quantum dots, by altering the cavity length with picometre precision. A Purcell enhancement of $F_p = 2.2$ was observed for a single dot, which was positioned at the exact antinode of the electric field in the cavity with unprecedented control. When excited non-resonantly, an exciton on resonance with the cavity displayed a multiphoton emission probability, $g^2(0) = 0.21$ for low power excitation. An interesting reduction in the correlation counts close to time zero was also observed for an exciton on resonance with the cavity. The $g^2(0)$ fully recovered within 100 ns. This effect was only visible at low excitation power.

The cavity beam waist at the dot layer was measured by translating a single dot through the cavity mode and measuring the corresponding radiative lifetime alteration. The measured lifetime distribution as a function of lateral displacement indicated that the fundamental cavity mode has a beam waist, $\omega_0 = 2.3$ μm. The

cavity Q was 6,500 and the calculated cavity mode volume was 19.7 μm^3. The first two higher order transverse modes were tuned to resonance with a single quantum dot. The first transverse mode demonstrated no interaction with a dot positioned at the exact antinode of the electric field. This was explained by a simulation of the electric field profile for the transverse modes, which indicated that the first transverse mode has a close to zero electric field at the point where the fundamental mode has a maximum electric field. Data was presented which suggests that large ensembles of quantum dots within the cavity may exhibit strong coupling with the cavity mode. Anti-crossing in the PL spectra was observed for both the curved and planar mirror cavities with a large Rabi splitting of 13.8 eV and 15.6 eV respectively.

Chapter 5

The nonlinear Fano effect

In 1961 U. Fano published the now famous paper [82] entitled 'Effects of configuration interaction on intensities and phase shifts', which rapidly became one of the most frequently cited publications in physics. Fano's paper presented a formula that applies to any discrete state which can interact with electronic continuum states to produce asymmetric lineshapes in the excitation spectra. The real beauty in this formula is that its context is vast, yet in its most simple form it describes an interference effect between two competing optical pathways. This quantum interference effect is observed in molecular spectroscopy, atomic photo-ionisation spectra [82] and condensed matter physics [83]. When the interaction with the continuum states involve only single particles, the phenomenon is known as Fano resonance. When many body effects are involved the process is known as the Kondo effect [84].

This chapter presents data which demonstrates asymmetric lineshapes observed in the absorption spectra from a single quantum dot. It is shown that these lineshapes are due to the Fano effect by fitting Fano's formula to the data taken at low power, giving a very good fit. The source of the continuum states is shown to be the beryllium doped back contact in the sample. Finally the power dependence of the lineshapes is detailed, demonstrating a dramatic increase in the degree of asymmetry with increasing excitation power. In contrast to the cavity experiments detailed in chapters 3 and 4, where a high finesse tunable cavity was used to effectively shield the quantum dot from the effect of the *photon* continuum states, the work here focuses on manipulating the *electronic* continuum within a charge-tunable semiconductor sample. Cavity QED effects demand that the quantum dot behaves as a two-level system. The Fano effect reveals subtle interactions with the continuum.

5.1 Linear regime: Fano lineshapes

In quantum dot laser spectroscopy, the linear regime describes the regime in which the absorption spectrum is independent of the excitation power. The absorption spectrum from individual quantum dots in an n-doped back contact device (the experimental techniques and device are discussed in chapter 2, section 2.7) have Lorentzian lineshapes [65], evidence of two-level behaviour. The hole spin in a quantum dot has a relaxation time approaching 1 ms [85] even without an applied magnetic field. In order to exploit the advantageous spin attributes, high fidelity control over the hole population within the dot is required. P-type doping in the back contact of a sample allows the dot to be loaded with holes. The Coulomb blockade enables deterministic charging of a single dot with individual holes.

The PL was used to identify the different charge states from the dots in a beryllium doped charge-tunable sample (chapter 2 section 2.7.1). The sample was excited by a laser at 830 nm. A voltage from -0.5 to 0.2 V was applied to the gate and the PL was collected using the techniques discussed in chapter 2.

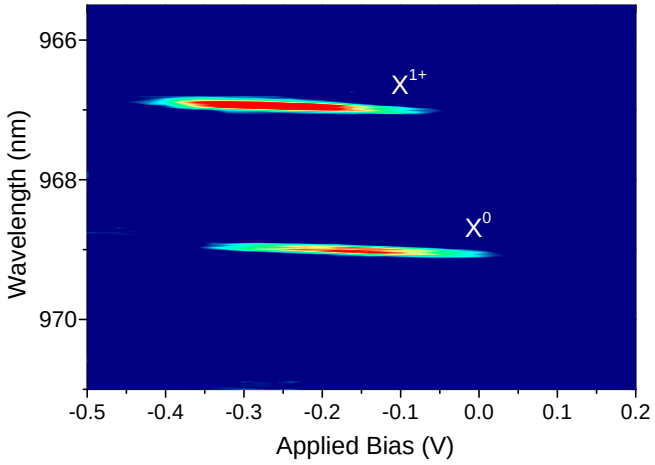

Figure 5.1: A colour plot showing the PL from the X^0 and X^{1+}. Red corresponds to 333 counts, blue to 90 counts, the read-out noise on the detector. The data was taken at 4 K from sample MVC12-2 by Brian Gerardot (HWU).

Figure 5.1 shows the colour plot of the PL taken at an excitation power density of 1 $\mu W/\mu m^2$. The plot shows the PL as a function of applied bias. The emission at 969.02 nm and 966.95 nm is from the X^0 and X^{1+} respectively. The data shows the charging from an X^0 to an X^{1+} by loading a single hole into the dot.

In an experiment using two other dots from sample MVC12-2 (p-type back contact) the lineshapes measured in the absorption spectra from X^{1+} transitions demonstrated

a high degree of asymmetry, shown in figure 5.2. Dot 1 (a) shows an asymmetric lineshape from an X^{1+} in the linear regime ($P_{exc} = 0.055$ nW), steeper on the negative detuning side than on the positive detuning side.

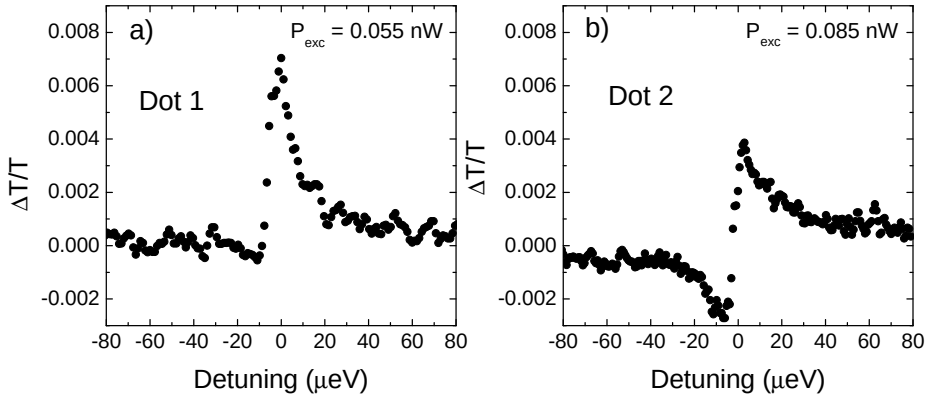

Figure 5.2: a) X^{1+} lineshape at very low excitation power ($P_{exc} = 0.055$ nW) from dot 1 ($\lambda = 935.95$ nm) within sample MVC12-2. b) An X^{1+} from dot 2 ($\lambda = 934.6$ nm) in sample MVC12-2. The data in (b) was taken using an excitation power of $P_{exc} = 0.085$ nW. Both dots were excited using the same spot size of 380 nm.

An X^{1+} from the other dot (Dot 2) in the sample showed an absorption lineshape which was dramatically asymmetric, even at low power, with a large overshoot of the collected signal at -10 μeV detuning, figure 5.2 (b). The excitation power is in the linear regime ($P_{exc} = 0.085$ nW), similar to the excitation power used in (a).

5.2 Fitting the data

The asymmetric lineshape observed in the absorption spectra (figure 5.2) are characteristic of Fano interference [82]. The situation leading to Fano interference requires three states: the ground state, an excited stated and a collection of extended states (i.e a continuum of states). Figure 5.3 shows a schematic of these states. Two optical transitions must occur, $|0\rangle$ - $|1\rangle$ and $|0\rangle$ - $|k\rangle$.

In addition to the two competing optical pathways, an interaction between the excited state and the continuum states must exist. In Fano's original scheme [82], the interaction with the continuum was an Auger process but it can also be of a different nature, tunnelling for example. Fano described this scheme mathematically [82],

$$A(E) = \frac{\alpha_0}{q^2\Delta}\frac{(\delta + q\Delta)^2}{\delta^2 + \Delta^2}, \tag{5.1}$$

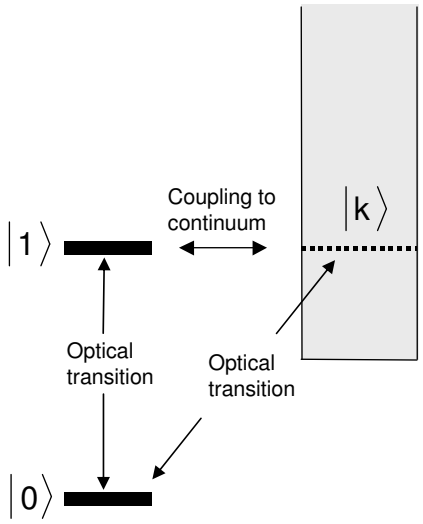

Figure 5.3: The components required for Fano interference. A continuum of states $|k\rangle$, a ground state $|0\rangle$ and an excited state $|1\rangle$ are shown. The two competing optical pathways are shown, $|0\rangle$ - $|1\rangle$ and $|0\rangle$ - $|k\rangle$.

for the quantum dot absorption experiment, A(E) is the differential contrast, δ is the detuning from resonance, Δ is the linewidth of the Fano lineshape, α_0 is the maximum contrast and q is the Fano parameter. The value q $\approx$ 1 indicates a very strong interaction with the electronic continuum states. Typically q is infinite if the interaction with the continuum is very weak as in the n-doped samples which show no Fano [65]. The mathematical definition of q is,

$$q = \frac{wV_0}{\Delta v}, \tag{5.2}$$

where w, v and V_0 are the matrix elements of the transitions $|1\rangle$-$|k\rangle$, $|0\rangle$-$|k\rangle$ and $|0\rangle$-$|1\rangle$ respectively and are assumed independent of the continuum state, $|k\rangle$. In the absorption experiment (chapter 2, section 2.7), the modulation technique measures A(E) - A(∞). From Fano's formula,

$$\frac{\Delta T}{T} = A(E) - A(\infty) = \frac{\alpha_0}{q^2\Delta}\Big[\frac{(q\Delta+\delta)^2}{\delta^2+\Delta^2} - 1\Big]. \tag{5.3}$$

This result is Fano's formula (valid at low power) for application to the absorption experiment and was used to fit to the X^{1+} absorption data in figure 5.2.

Figure 5.4 shows the low power absorption spectra of dots 1 and 2. Very good fits to the low power absorption spectra are obtained using equation 5.3. The best fit to Dot 1 (a) was obtained with q = 3.73, Δ = 5.7 μeV and α_0 = 0.009. For the

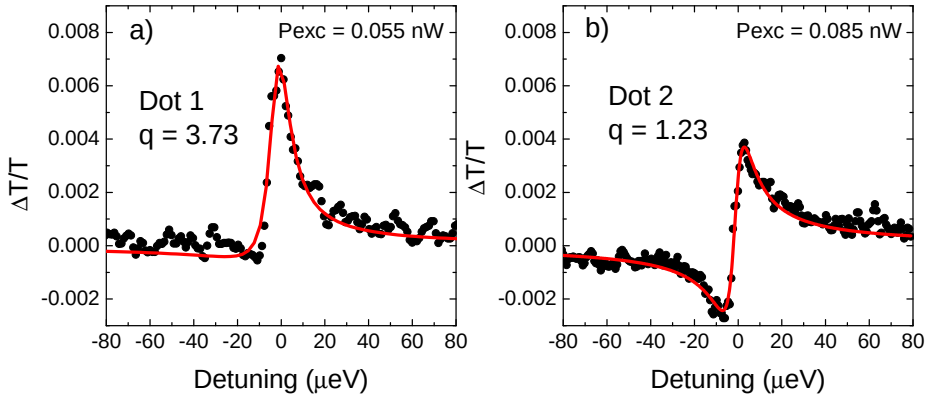

Figure 5.4: Fits (red lines) to the absorption data (the same data as in figure 5.2) using equation 5.3. a) Dot 1: q = 3.73 and $\Delta = 5.7$ μeV. b) Dot 2: q = 1.23 and $\Delta = 5$ μeV.

absorption spectra from dot 2 (figure 5.4 (b)) the best fit was obtained with, q = 1.23, $\Delta = 5$ μeV and $\alpha_0 = 0.016$. The undershoot in the absorption spectra in figure 5.4 (b) is due to destructive interference, whilst the peak is due to constructive interference.

The difference in the strength of the interaction with the continuum states between the two dots is most likely due to the dot to dot fluctuation of the local density of states.

The values of q for the two dots in the p-type sample are small compared to those measured in similar structured n-doped samples which showed Fano lineshapes with q values ranging from 10 to 15 [83]. The interaction with the continuum states in the n-doped samples has been shown to be a tunnelling interaction [83].

5.3 Nonlinear regime: lineshape evolution with power

The behaviour of the Fano resonance in the nonlinear regime has until now, not been studied experimentally. Presumably this is due to the lack of suitable high power excitation sources in the deep ultraviolet spectral region, the test-bed of Fano's theory. By utilising InGaAs quantum dots, the energy scale in the infra-red is much more convenient allowing the transitions to be excited at high powers with ease.

Absorption spectra were measured for dot 1 as a function of excitation power and are shown in figure 5.5. The spectra were measured using a laser power of 0.055, 0.2, 1, 2, 5 and 9.5 nW. The spectra are fitted using equation 5.3 (red line), with excellent fits obtained at low power and good fits obtained at high power. The free parameter q, gives a value of 3.73 and 1.5 at 0.055 nW and 9.5 nW respectively.

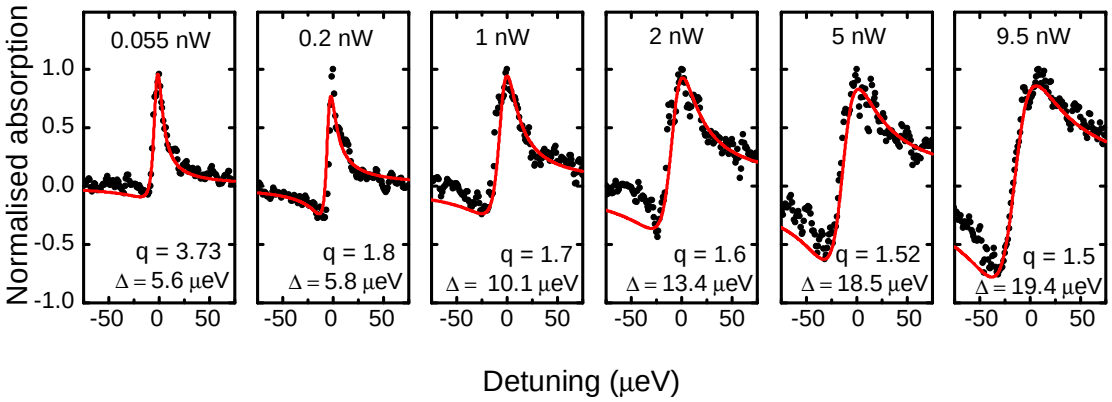

Figure 5.5: Absorption data from the X^{1+} in dot 1 (sample MVC12-2). At P = 0.055 nW the lineshape is close to Lorentzian, but as the power is increased above ≈ 1 nW the lineshape becomes increasingly asymmetric. The red lines are best fits to the data from equation 5.3, with q as a fit parameter. As the power is increased, q → 1. Each spectrum has been normalised using the following factors: 0.0072, 0.0041, 0.0014, 0.0015, 0.0006, 0.00061.

The degree of asymmetry in the absorption lineshapes also gives an indication of the visibility of the Fano effect. The ratio of the negative signal to the positive signal in the differential transmission is used to evaluate the strength of the continuum interaction, figure 5.6.

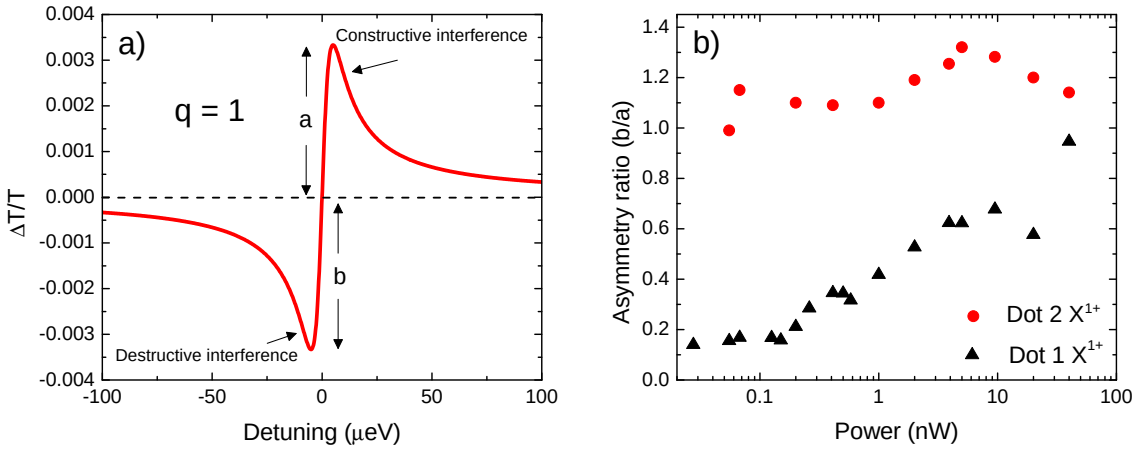

Figure 5.6: a) A simulated Fano lineshape with the undershoot, b, equal to the positive signal, a, which corresponds to q = 1. b) The ratio b/a is plotted as a function of power for dot 1 and dot 2. As the excitation power is increased, dot 1's lineshape becomes increasingly asymmetric, with b/a tending towards unity, as the visibility of the Fano effect increases.

At low powers the negative signal (destructive interference) was very small for dot 1, only 1/5 of the positive signal. As the power was increased, a strongly asymmetric lineshape with b/a = 1 was observed. Dot 2 showed a very high degree of asymmetry even at low power (< 0.1 nW), with very little change in the line shape with increasing power, 5.6 (b).

The q for both dots was recorded for each fit and plotted as a function of power, figure 5.7. The q for dot 1 (black) decreases with increasing excitation power as the exciton transition saturates. Dot 2 (red) shows q ≈ 1, independent of excitation power. The transition from the initial state to the continuum dominates even at low power for dot 2, therefore saturating the discrete state has no additonal effect on the Fano lineshape.

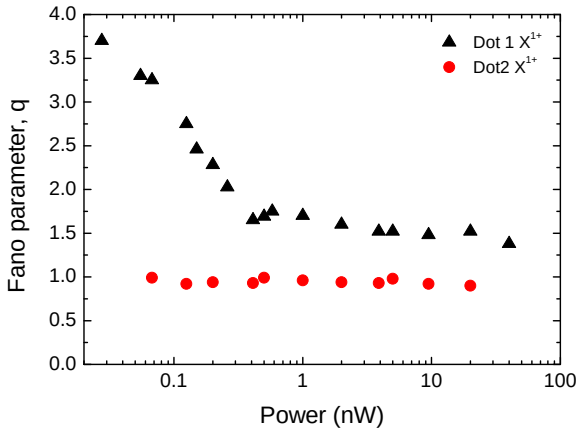

Figure 5.7: Measured q for both dots as a function of power. The value of q was determined by fitting to each spectra using equation 5.3. For dot 1 (black), q reduces with increasing excitation power as the Fano lineshape becomes more pronounced. Dot 2 (red) shows no change in q with excitation power.

5.4 Nonlinear Fano effect: model and assumptions

Thus far, the fits to the Fano resonance data have been based on Fano's original formula, valid at low excitation power. However Fano's original model does not include spontaneous emission (or any other radiative decay processes) and a more complete mathematical model was constructed by A. O. Govorov [83], to extend into the nonlinear regime. The model was devised to describe the Fano lineshapes observed by Kroner et al. [83] in the absorption spectra from n-doped samples. The model uses the density matrix for the system and additional details of the model can be found in reference [83].

An energy level diagram of the model is shown in figure 5.8. The concept is that a discrete optical transition, $|0\rangle$ - $|1\rangle$, weakly interacts with some continuum of states via tunnelling at a rate, γ_{tun}. The tunnelling process hybridises the final discrete state with the continuum states, $|k\rangle$. A relaxation process also exists between the lower continuum state, $|k\rangle$ and the ground state of the discrete transition, $|0\rangle$, with rate γ_{20}. Crucially an optical transition is possible between the initial discrete state and the continuum, Ω_{0k}. This transition provides an alternative optical pathway. The two conditions required for the Fano effect therefore exist : two competing optical pathways and a hybridised excited state. Also shown in figure 5.8 is the Rabi frequency Ω_{01}, the spontaneous emission rate γ_{10} and the relaxation rate within the continuum, γ_{k2}.

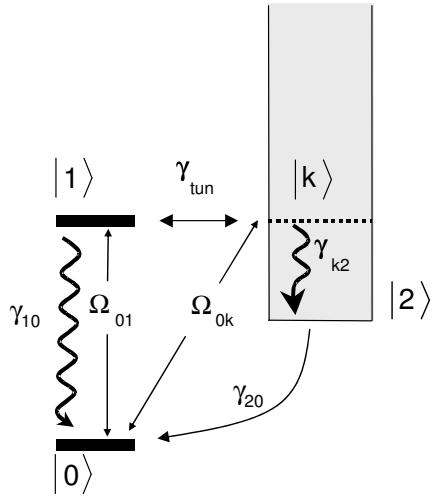

Figure 5.8: The energy level diagram for the quantum interference scheme, showing the levels, transitions and rates for the continuum and discrete state [83]. An explanation of each term is included in the text.

Govorov's mathematical model describes the processes in figure 5.8. It uses the fixed parameters : γ_{10}, q and Δ. The model allows the lineshape to be calculated by fixing these parameters and altering the value for the Rabi energy, which is proportional to the square root of the resonant laser power [9].

This model was used to calculate the expected lineshapes from the p-type sample as a function of excitation power. Firstly, γ_{10} was set to 1 μeV, corresponding to a radiative decay time of 0.65 ns [7]. q and Δ were obtained by fitting to the dot 1 data

at low power using equation 5.3 to obtain q = 3.73 and $\Delta = 5$. The q value used in Govorov's model was reduced to q = 3.0 to give the best fit to both the high and low power data. By adjusting a scaling factor in the model (R4) to 0.005, a very good agreement to the experimentally measured lineshape was obtained for the spectrum taken at 0.055 nW. The model was used to calculate the lineshape at each of the other laser powers (0.2, 1, 2, 5 and 9.5 nW).

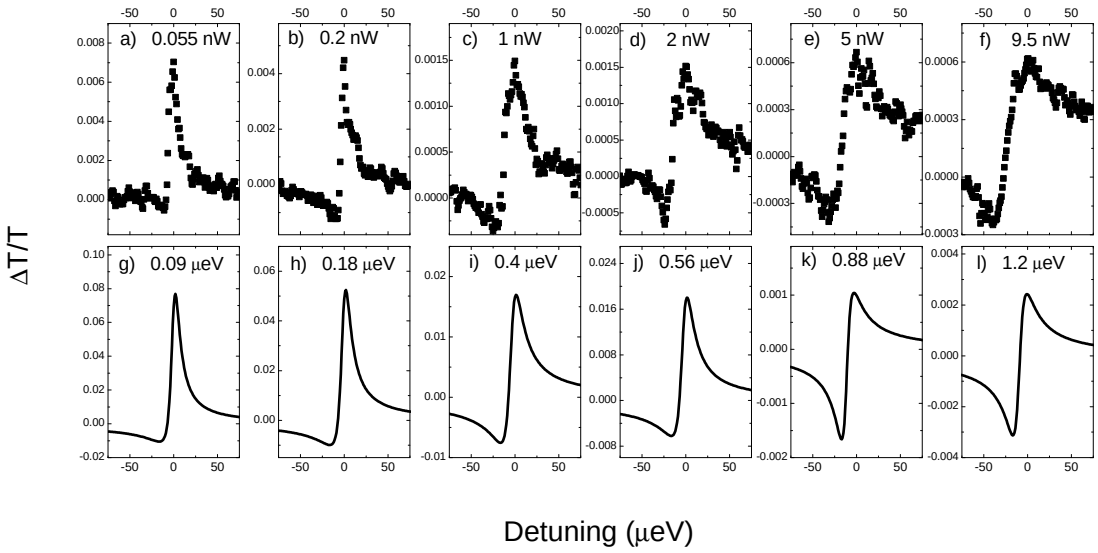

Figure 5.9: Plots a) to f): X^{1+} absorption data from dot 1 in sample MVC12-2.
g) to l): calculated absorption spectra with parameters $\hbar\gamma_{10} = 1$ μeV, q = 3, $\Delta = 5$ μeV. The Rabi energies are indicated at the top of the panels (g - l) and correspond to the laser powers used in the experiment.

Figure 5.9 (a) to (f) show the absorption spectra from dot 1 for increasing excitation power. Figure 5.9 (g) to (l) show the predicted lineshape of the absorption spectra, calculated from Govorov's nonlinear Fano model. By setting the other parameters as fixed ($\hbar\gamma_{10} = 1$ μeV, q = 3, $\Delta = 5$ μeV) and adjusting only the Rabi energy in the model, the lineshapes at various excitation powers are accurately reproduced. However, although the model reproduced the lineshapes extremely well, it did not predict the absorption intensities accurately. Although both the data and the model showed a decrease of the signal contrast with increasing excitation power, the model predicts a contrast 11.7 times larger than the data at low power (0.055 nW) and 6.5 times larger than the data at high power (9.5 nW).

To determine the Rabi energy of each of the spectra from the laser power, data was taken from a sample which showed no Fano resonance, but with identical experimental

conditions. The absorption spectra were measured as a function of excitation power over 5 orders of magnitude. Lorentzian lineshapes were fitted to the absorption spectra and the FWHM of the absorption peak is plotted as a function of power in figure 5.10.

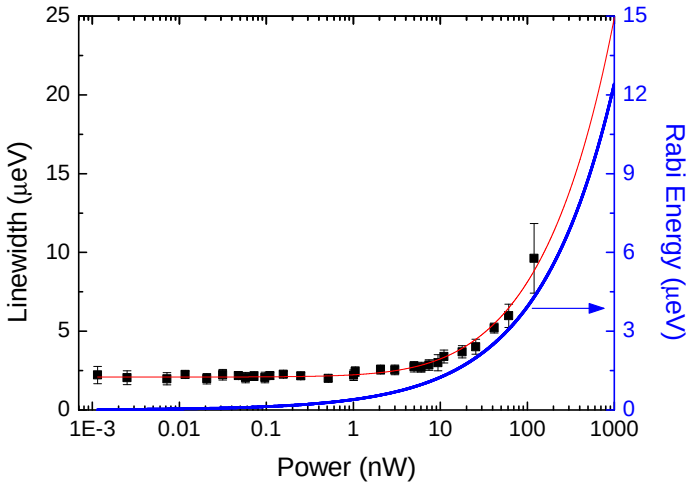

Figure 5.10: Absorption linewidth versus power, measured for a single X^{1+} from a sample showing no Fano effect. The Rabi energy is calculated (blue curve) using $0.5(\Gamma^2 - \Gamma_0^2)^{1/2}$ [86] for each excitation power. The data was taken by Brian Gerardot, (HWU).

Figure 5.10 shows the power broadening as the transition saturates at about 10 nW [87]. The Rabi energy for each laser power was calculated from figure 5.10 (blue line), each value was then entered into Govorov's model to calculate the lineshape for the dots showing Fano effects.

The evolution of the absorption lineshape with excitation power for dot 2 was also calculated using Govorov's model. The fixed parameters which gave the best fit were: $\hbar\gamma_{10} = 1$ μeV, q = 1.1, $\Delta = 5.5$ μeV. The Fano parameter, q was set to 1.1 (close to the low power value of q = 1.23 obtained in figure 5.4 (b)). The absorption data and predicted lineshapes for dot 2 are shown in figure 5.11. The calculated lineshapes match the absorption data for dot 2 very well at low power and are in reasonable agreement at high power. However, the signal contrast for the calculated spectra does not match the data very well, similar to the calculated spectra for dot 1.

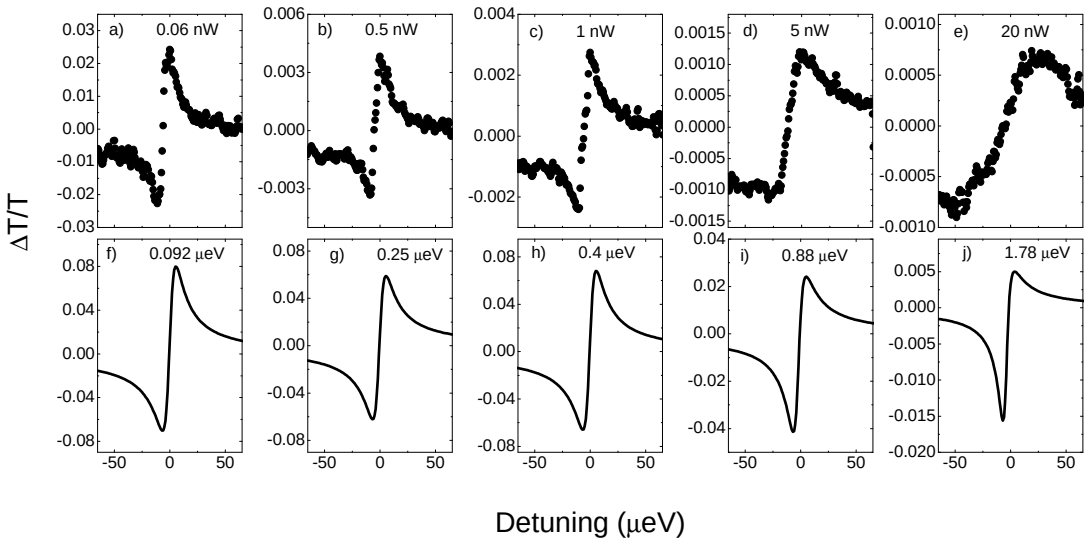

Figure 5.11: Plots a) to e): X^{1+} absorption data from dot 2 in sample MVC12-2.
f) to j): calculated absorption spectra with parameters $\hbar\gamma_{10} = 1$ μeV, q = 1.1, $\Delta = 5.5$ μeV. The Rabi energies are indicated at the top of the panels (f - j) and correspond to the laser powers used in the experiment.

5.5 Carbon doping

The electronic continuum is thought to be related to the beryllium atoms in the back contact of the sample. An interaction is possible between the continuum and discrete states due to close proximity of the defect states to the dots, as a result of the diffusion of beryllium atoms through the GaAs material during the growth process [88, 89, 90]. It has been proposed that a process known as interstitial-substitutional diffusion is the mechanism responsible for the transport of the Be atoms [89]. It is also well known that the beryllium atom diffusion in III - V semiconductors in the growth direction can be as much as 100 nm [89, 90]. Sample MVC12-2 has a tunnel barrier of 25 nm (chapter 2) separating the dots from the Be-doped back contact, therefore it is very likely that some beryllium atoms diffuse to the dot layer, forming an electronic continuum. However it is not clear how the beryllium forms a continuum of states at energies close to the GaAs band gap. It is also possible to obtain p-type doping using carbon doping [91]. It is well known that carbon atoms have much lower diffusitivity than beryllium atoms, therefore they remain within the back contact region during the growth process [91]. To test if the continuum states arise from the Be doping in sample MVC12-2, a carbon doped sample was studied (wafer 060726B). The sample is identical in structure to the Be doped sample, except for the dopant species in the back contact.

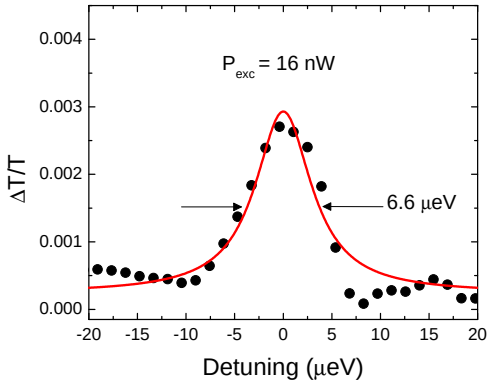

Figure 5.12: Absorption data from a carbon doped back contacted sample (wafer 060726B). At an excitation power of 16 nW, the absorption lineshape is Lorentzian (red line) with a linewidth of 6.6 μeV. The data was taken by Daniel Brunner (HWU).

The absorption lineshape of a single X^{1+} was measured using exactly the same experimental set-up used to take the data in figure 5.5. Figure 5.12 shows the absorption spectra from a single X^{1+} from wafer 060726B. At an excitation power of 16 nW, the absorption spectra has a Lorentzian lineshape with a linewidth of 6.6 μeV, indicative of two-level behaviour. Unmistakable Fano resonances were measured in the absorption lineshapes measured from the beryllium doped sample (figure 5.5) at an excitation power of 9.5 nW.

5.6 Summary

A dot dependent nonlinear Fano effect was observed for X^{1+} transitions in a Be doped back contacted sample. The Fano effect was found to become more pronounced as the X^{1+} transition saturates. The source of the continuum states was attributed to the Be doping. Carbon doped samples showed Lorentzian lineshapes, demonstrating that the use of carbon dopants eliminate the source of the continuum states and hence eliminate the Fano effect. The Fano effect observed at high power is a useful tool to detect the presence of even very weak coupling to the continuum states.

Chapter 6

Conclusions and future work

A unique feature of the new solid-state cavity technology presented in this work is the use of a miniature concave mirror (dielectric coating on silica), separated from a semiconductor DBR by an air gap of about a one micron to form a microscopic optical cavity. This has allowed the realisation of a fully tunable, generic microcavity platform with all the desirable qualities listed in chapter 3, section 3.1. The concave mirror reduces diffraction losses, allowing a much higher Q-factor than that obtainable with planar cavities. The concave mirror templates were fabricated using laser ablation, and have radii of curvature 50 -150 μm with sub-nm surface roughness. The ultra-smooth surface allows a high quality dielectric coating to be deposited. The reflectivity of the curved mirror is 99.9%. A radius of curvature of 120 μm has been measured using a surface profiler. This has been confirmed by analysing the separation of the higher-order transverse modes.

By changing the cavity length, the wavelength can be tuned with picometre resolution, over a broad tuning range of several hundred nanometres. The cavity housing has been designed to prevent mechanical noise reducing the cavity Q, whilst allowing easy integration into the existing confocal microscope apparatus. The stability required in the vertical direction is on par with that of scanning tunneling microscope systems. No Q-spoiling was observed due to vibrational noise. The cavity spectrum was characterised at 300 K by coupling a 950 nm laser through the top mirror and recording the transmission as a function of the voltage applied to the z piezo. The room temperature finesse from the half-symmetric cavity was measured to be F = 1,500. This is two orders of magnitude greater than the finesse measured from the planar-planar geometry cavity (F = 15).

The cavity was also shown to be fully operational at cryogenic temperatures and is in fact better behaved at low temperature as creep and hysteresis of the piezo are eliminated at 4 K.

Quantum dots inside the cavity have been utilised to characterise it at low temperature. At 77 K each dot's linewidth is sufficiently broad that the emission is a continuous spectrum (high dot density sample). Therefore the PL from the ensemble of dots was used as an internal light source, with light emerging from the cavity at a wavelength determined by the cavity resonance. It was found that the Q varied from 6,500 at the shortest cavity length (4.75 μm) to 55,000 at the longest cavity length (50 μm). At a cavity length of 4.75 μm, the tunable cavity has a Q-factor (Q = 6,500) and a mode volume (19.7 μm^3) on a par with large semiconductor micropillar cavities.

Single quantum dots inside the cavity have been studied at 4 K. At 4 K a broad band emission exciting the cavity mode is always present even for large spectral detuning from all the dots. However, at certain wavelengths the PL intensity increases significantly, corresponding to an interaction with a single quantum dot. The broadband emission into the detuned cavity mode has been reported before by others in semiconductor micropillars and photonic crystal cavities. However this is the first observation of the effect in a device which involves no significant etching processes during fabrication. This is important as it rules out the possibility of the effect originating from the additional free surfaces introduced by etching. The most likely origin is the exciton-acoustic phonon interaction.

Correlation measurements using a Hanbury Brown-Twiss interferometer indicated that when the cavity was on resonance with a single quantum dot, the emission from the dot was anti-bunched. Under non-resonant pulsed excitation, the measured $g^2(0) = 0.21$. This is more than a four-fold reduction in the multiphoton probability compared to that of a classical source.

A single quantum dot's radiative lifetime was studied as a function of its spectral detuning and position in the lateral plane relative to the cavity mode. This was necessary in order to measure the degree of dot/cavity coupling. A Purcell effect of 2.2 was measured for the dot when it was positioned at the exact antinode of the cavity's electric field using the xy and z piezo positioners. The exact anti-node was obtained by recording the radiative lifetime as a function of applied voltage to the xy positioners, whilst maintaining the spectral resonance. The radiative decay time was smallest at x,y = 0, increasing as the dot was displaced with respect to the cavity anti-node. This provided a lateral diameter of the fundamental cavity mode by fitting a Gaussian (FWHM = 2.5 μm) to the data. This corresponded well with value FWHM = 2.3 μm expected from Gaussian optics. The mode volume was determined to be 19.7 μm^3 from the cavity length (4.75 μm) and the measured beam diameter (FWHM = 2.5 μm). A cavity length of 4.75 μm indicates an airgap of 1-3 μm, with the rest of the cavity field within the mirrors and semiconductor layer. It is possible that this

gap could be reduced to less than 1 micron, with very thorough cleaning of the cavity mirrors.

When the dot was positioned at the antinode, the measured lifetime enhancement was shown to be close to the theoretical maximum for the cavity Q and mode volume. Further confirmation that the dot was at the exact anti-node of the electric field was obtained by studying the interaction between the quantum dot and the first transverse mode. Only a very weak interaction between the first transverse mode and the dot was observed. This would be expected if the dot was at the exact anti-node of the electric field.

The in situ positioning of a single dot with respect to the cavity mode described here, successfully resolves a long standing experimental challenge in solid-state cavity experiments. The traditional approach requires both a high dot density and some degree of luck to ensure an optimal match between the dot and the cavity mode. The approach described in this work removes the element of chance, allowing the Purcell effect to be determined solely by the cavity Q and V.

The PL from a large ensemble of dots was observed to show anti-crossing with the cavity mode. The effect was observed for both planar-planar and concave-planar cavity geometries. This tantalising effect is attributed to the collective effect of hundreds of dots, giving rise to a large Rabi splitting (13.8 meV) analogous to that observed with ensembles of atoms in a cavity in atomic physics, but has never been reported before for quantum dots. It is thought that a particularly homogenous dot sample combined with a very high dot density gives rise to a super-radiance effect. For the planar cavity geometry the anti-crossing data is supported by the exchange of linewidths and intensities of the two peaks at resonance.

A dot-dependent Fano resonance was demonstrated in the absorption spectra from single quantum dots in a charge-tunable sample. For some dots, the visibility of the Fano resonance increased with increasing excitation power. However for other dots the Fano lineshape was very pronounced even at low power. These dots lineshape exhibited no power dependence. The likely origin of the Fano resonance is defect states associated with the beryllium atoms in the back contact of the sample. The effect was not observed in the spectra from an identical sample structure which had a carbon doped back contact. The tunable cavity could be used in conjunction with the charge tunable samples, utilising the Purcell effect to dramatically increase the weak absorption signal. However this will involve redesigning the charge tunable samples to incorporate a semiconductor DBR.

Future work

Although the development of the fully tunable cavity offers a satisfactory solution to the tuning challenges in semiconductor microcavities, strong coupling with a single quantum dot has not been achieved in this work. This is may be due to the quality of the top dielectric mirror and the relatively large mode volume (compared to photonic crsytal cavities).

The Rabi splitting in the strong coupling regime depends on $Q/\sqrt{V}$. Therefore it is more effective to increase Q than to decrease V. Increasing the cavity Q could be achieved by coating the ablated substrate with a 'super mirror' coating which can achieve a reflectivity of 99.9999% [92]. This increase in reflectivity could result in a substantially larger Q. With this increase in Q, a much larger Purcell effect could be realised, or the strong coupling regime achieved for a single quantum dot. The tunable cavity could also be operated at a much longer cavity length. It was shown in chapter 4 of this work that at a cavity length of 50 μm the Q factor is nearly one order of magnitude greater than that of a 5 μm long cavity. It is conceivable that $Q = 10^6$ could be achieved for a long cavity of 50 μm and very high quality mirrors. Thus lengthening the cavity to exploit the $Q/\sqrt{V}$ dependence of the Rabi splitting could enable single dot strong coupling.

In order to increase the Purcell effect, a decrease in the cavity mode volume is also desirable. One potential solution to reduce the mode volume would involve a lift-off process, whereby a layer of dots is transferred onto a dielectric mirror. This would shorten the effective cavity length (by decreasing the penetration into the mirrors), reducing the mode volume. However it is not clear at present if the surface scattering from the lift-off layer/DBR interface would detrimentally reduce Q. Other possible solutions to reduce the mode volume could involve reducing the radius of curvature of the concave mirror and reducing the depth of the curved mirror to shorten the minimum possible air gap.

One area which would be extremely interesting to pursue is the ensemble dot strong coupling effect. A study of the magnitude of the Rabi splitting as a function of dot density (using samples of different dot densities) could add further evidence to the experimental data in this work. In particular if a very low dot density sample was used, weak coupling might be observed in the PL spectra from the ensemble of dots. Several other experiments would be beneficial, such as measuring the radiative lifetime of the two PL peaks as a function of cavity detuning. If the peaks are indeed polaritons, it would be expected that the measured lifetime from each peak would be very short. Another approach would be to design and grow a very homogenous dot sample, such that most of the dots are of similar size and the spread of emission

energies is small. This could lead to an even larger Rabi splitting from an ensemble of quantum dots.

The cavity developed here forms a generic platform easily applied to other areas of cavity QED such as coupling single diamond NV centers to a high Q cavity mode. Diamond colour centers are particularly promising candidates for quantum information processing as they exhibit exceptional optical and spin properties. At low temperature, the electron spin decoherence time is nearly as long as a millisecond. It is this property that makes a cavity QED based system of NV centers very attractive to pursue applications such as quantum internet. The tunable cavity presented in this work would provide an ideal platform for precisely coupling diamond NV centers to a high Q factor mode.

The real beauty of the tunable cavity is that the strength of the coupling to the NV center would depend entirely on the cavity parameters, Q and V. This eliminates the element of luck involved in achieving the strong coupling regime in existing technology. The ability to achieve strong coupling on demand would enable experiments such as the transfer of the spin coherence of a NV center to a superposition of photons via a cavity QED process. This spin-photon interface could play a crucial role in a quantum network.

References

[1] S. Haroche and D. Kleppner. Cavity quantum electrodynamics. *Physics Today* **42**, 24 (1989).

[2] R. J. Warburton. Self-assembled semiconductor quantum dots. *Contemporary Physics* **43**, 351 (2002).

[3] J. M. Garcia, G. Medeiros-Ribeiro, K. Schmidt, T. Ngo, J. L. Feng, A. Lorke, J. Kotthaus, and P. M. Petroff. Intermixing and shape changes during the formation of InAs self-assembled quantum dots. *Appl. Phys. Lett.* **71**, 2014 (1997).

[4] D. Leonard, K. Pond, and P. M. Petroff. Critical layer thickness for self-assembled InAs islands on GaAs. *Phys. Rev. B* **50**, 11687 (1994).

[5] J. H. Davies. *The Physics of Low Dimensional Semiconductors: An Introduction.* Cambridge University Press. 1998.

[6] A. Högele, S. Seidl, M. Kroner, K. Karrai, R. J. Warburton, B. D. Gerardot, and P. M. Petroff. Voltage-controlled optics of a quantum dot. *Phys. Rev. Lett.* **93**, 217401 (2004).

[7] P. A. Dalgarno, J. M. Smith, J. McFarlane, B. D. Gerardot, K. Karrai, A. Badolato, P. M. Petroff, and R. J. Warburton. Coulomb interactions in single charged self-assembled quantum dots: Radiative lifetime and recombination energy. *Phys. Rev. B* **77**, 245311 (2008).

[8] C. Santori, D. Fattal, J. Vučković, G. S. Solomon, E. Waks, and Y. Yamamoto. Submicrosecond correlations in photoluminescence from InAs quantum dots. *Phys. Rev. B* **69**, 205324 (2004).

[9] K. Karrai and R. J. Warburton. Optical transmission and reflection spectroscopy of single quantum dots. *Superlattices and Microstructures* **33**, 311 (2003).

[10] R. J. Warburton, C. S. Dürr, K. Karrai, J. P. Kotthaus, G. Medeiros-Ribeiro, and P. M. Petroff. Charged excitons in self-assembled semiconductor quantum dots. *Phys. Rev. Lett.* **79**, 5282 (1997).

[11] A. W. Weiss. Series perturbations and atomic oscillator strengths: The ^2D series of Al I. *Phys. Rev.* **178**, 82 (1969).

[12] E. M. Purcell. Spontaneous emission probabilities at radio frequencies. *Phys. Rev.* **69**, 681 (1946).

[13] J. M. Gérard, B. Sermage, B. Gayral, B. Legrand, E. Costard, and V. Thierry-Mieg. Enhanced spontaneous emission by quantum boxes in a monolithic optical microcavity. *Phys. Rev. Lett.* **81**, 1110 (1998).

[14] P. Michler, A. Kiraz, C. Becher, W. V. Schoenfeld, P. M. Petroff, L. Zhang, E. Hu, and A. Imamoglu. A quantum dot single-photon turnstile device. *Science* **290**, 2282 (2000).

[15] B. Gayral, J. M. Gérard, B. Sermage, A. Lemaître, and C. Dupuis. Time-resolved probing of the purcell effect for InAs quantum boxes in GaAs microdisks quantum boxes in GaAs microdisks. *Appl. Phys. Lett.* **78**, 2828 (2001).

[16] L. A. Graham, D. L. Huffaker, and D. G. Deppe. Spontaneous lifetime control in a native-oxide-apertured microcavity. *Appl. Phys. Lett.* **74**, 2408 (1999).

[17] G. S. Solomon, M. Pelton, and Y. Yamamoto. Single-mode spontaneous emission from a single quantum dot in a three-dimensional microcavity. *Phys. Rev. Lett.* **86**, 3903 (2001).

[18] A. Kiraz, P. Michler, C. Becher, B. Gayral, A. Imamoğlu, L. Zhang, E. Hu, W. V. Schoenfeld, and P. M. Petroff. Cavity-quantum electrodynamics using a single InAs quantum dot in a microdisk structure. *Appl. Phys. Lett.* **78**, 3932 (2001).

[19] C. Santori, D. Fattal, J. Vučković, G. S. Solomon, and Y. Yamamoto. Indistinguishable photons from a single-photon device. *Nature* **419**, 594 (2002).

[20] J. Vučković, D. Fattal, C. Santori, G. S. Solomon, and Y. Yamamoto. Enhanced single-photon emission from a quantum dot in a micropost microcavity. *Appl. Phys. Lett.* **82**, 3596 (2003).

[21] E. Moreau, I. Robert, J. M. Gérard, I. Abram, L. Manin, and V. Thierry-Mieg. Single-mode solid-state single photon source based on isolated quantum dots in pillar microcavities. *Appl. Phys. Lett.* **79**, 2865 (2001).

[22] D. C. Unitt, A. J. Bennett, P. Atkinson, D. A. Ritchie, and A. J. Shields. Polarization control of quantum dot single-photon sources via a dipole-dependent Purcell effect. *Phys. Rev. B* **72**, 033318 (2005).

[23] B. Min, S. Kim, K. Okamoto, L. Yang, A. Scherer, H. Atwater, and K. Vahala. Ultralow threshold on-chip microcavity nanocrystal quantum dot lasers. *Appl. Phys. Lett.* **89**, 191124 (2006).

[24] P. Michler, A. Kiraz, L. Zhang, C. Becher, E. Hu, and A. Imamoğlu. Laser emission from quantum dots in microdisk structures. *Appl. Phys. Lett.* **77**, 184 (2000).

[25] A. M. Fox. *Quantum Optics: An Introduction.* Oxford University Press. 2006.

[26] C. Weisbuch and B. Vinter. *Quantum Semiconductor Structures: Fundamentals and Applications.* Elsevier, third edition. 1991.

[27] C. Ciuti, P. Schwendimann, and A. Quattropani. Theory of polariton parametric interactions in semiconductor microcavities. *Semicond. Sci. Technol.* **18**, S279 (2003).

[28] C. Weisbuch, M. Nishioka, A. Ishikawa, and Y. Arakawa. Observation of the coupled exciton-photon mode splitting in a semiconductor quantum microcavity. *Phys. Rev. Lett.* **69**, 3314 (1992).

[29] J. P. Reithmaier, G. Sek, A. Loffler, C. Hofmann, S. Kuhn, S. Reitzenstein, L. V. Keldysh, V. D. Kulakovskii, T. L. Reinecke, and A. Forchel. Strong coupling in a single quantum dot-semiconductor microcavity system. *Nature* **432**, 197 (2004).

[30] K. Hennessy, A. Badolato, M. Winger, D. Gerace, M. Atatüre, S. Gulde, S. Falt, E. L. Hu, and A. Imamoğlu. Quantum nature of a strongly coupled single quantum dot-cavity system. *Nature* **445**, 896 (2007).

[31] A. Boca, R. Miller, K. M. Birnbaum, A. D. Boozer, J. McKeever, and H. J. Kimble. Observation of the vacuum rabi spectrum for one trapped atom. *Phys. Rev. Lett.* **93**, 233603 (2004).

[32] A. D. Boozer, A. Boca, R. Miller, T. E. Northup, and H. J. Kimble. Cooling to the ground state of axial motion for one atom strongly coupled to an optical cavity. *Phys. Rev. Lett.* **97**, 083602 (2006).

[33] Y. Colombe, T. Steinmetz, G. Dubois, F. Linke, D. Hunger, and J. Reichel. Strong atom-field coupling for Bose-Einstein condensates in an optical cavity on a chip. *Nature* **450**, 272 (2007).

[34] T. Aoki, B. Dayan, E. Wilcut, W. P. Bowen, A. S. Parkins, T. J. Kippenberg, K. J. Vahala, and H. J. Kimble. Observation of strong coupling between one atom and a monolithic microresonator. *Nature* **443**, 671 (2006).

[35] I. Abram, I. Robert, and R. Kuszelewicz. Spontaneous emission control in semiconductor microcavities withmetallic or Bragg mirrors. *IEEE Journal of Quantum Electronics* **34**, 71 (1998).

[36] M. Born and E. Wolf. *Principles of Optics: Electromagnetic Theory of Propagation, Interference and Diffraction of Light.* Cambridge University Press, seventh edition. 1999.

[37] T. Rivera, J.-P. Debray, J. M. Gérard, B. Legrand, L. Manin-Ferlazzo, and J. L. Oudar. Optical losses in plasma-etched AlGaAs microresonators using reflection spectroscopy. *Appl. Phys. Lett.* **74**, 911 (1999).

[38] M. Fox. Sheffield University department of Physics, LDSD group, Photonic Structures page. Online, cited July 2009, available at: http://www.ldsd.group.shef.ac.uk/photonics/.

[39] D. Press, S. Gotzinger, S. Reitzenstein, C. Hofmann, A. Loffler, M. Kamp, A. Forchel, and Y. Yamamoto. Photon antibunching from a single quantum-dot-microcavity system in the strong coupling regime. *Phys. Rev. Lett.* **98**, 117402 (2007).

[40] C. Kistner, S. Reitzenstein, C. Böckler, R. Debusmann, J. Claudon, L. Grenouillet, S. Höfling, J. M. Gérard, and A. Forchel. Weak coupling effects in high-Q electrically driven micropillars. *Physica Status Solidi (c)* **6**, 381 (2008).

[41] B. Urbaszek, E. J. McGhee, M. Krüger, R. J. Warburton, K. Karrai, T. Amand, B. D. Gerardot, P. M. Petroff, and J. M. Garcia. Temperature-dependent linewidth of charged excitons in semiconductor quantum dots: Strongly broadened ground state transitions due to acoustic phonon scattering. *Phys. Rev. B* **69**, 035304 (2004).

[42] C. Kistner, T. Heindel, C. Schneider, A. Rahimi-Iman, S. Reitzenstein, S. Höfling, and A. Forchel. Demonstration of strong coupling via electro-optical tuning in high-quality QD-micropillar systems. *Opt. Express* **16**, 15006 (2008).

[43] D. Englund, I. Fushman, and J. Vučković. General recipe for designing photonic crystal cavities. *Opt. Express* **13**, 5961 (2005).

[44] R. J. P. Engelen. FOM Institute for Atomic and Molecular Physics, NanoOptics Group, Photonics Crystals page. Online, cited July 2009, available at: http://naphot.amolf.nl/photcrys.htm.

[45] K. Hennessy, A. Badolato, A. Tamboli, P. M. Petroff, E. Hu, M. Atatüre, J. Dreiser, and A. Imamoğlu. Tuning photonic crystal nanocavity modes by wet chemical digital etching. *Appl. Phys. Lett.* **87**, 021108 (2005).

[46] A. Badolato, K. Hennessy, M. Atatüre, J. Dreiser, E. Hu, P. M. Petroff, and A. Imamoğlu. Deterministic coupling of single quantum dots to single nanocavity modes. *Science* **308**, 1158 (2005).

[47] M. Kaniber, A. Laucht, A. Neumann, J. M. Villas-Boas, M. Bichler, M.-C. Amann, and J. J. Finley. Investigation of the nonresonant dot-cavity coupling in two-dimensional photonic crystal nanocavities. *Phys. Rev. B* **77**, 161303 (2008).

[48] B. Gayral, J. M. Gérard, A. Lemaitre, C. Dupuis, L. Manin, and J. L. Pelouard. High-Q wet-etched GaAs microdisks containing InAs quantum boxes. *Appl. Phys. Lett.* **75**, 1908 (1999).

[49] E. Peter, P. Senellart, D. Martrou, A. Lemaitre, J. Hours, J. M. Gérard, and J. Bloch. Exciton-photon strong-coupling regime for a single quantum dot embedded in a microcavity. *Phys. Rev. Lett.* **95**, 067401 (2005).

[50] J. Verbert, F. Mazen, T. Charvolin, E. Picard, V. Calvo, and P. Noé. Efficient coupling of Er-doped silicon-rich oxide to microdisk whispering gallery modes. *Appl. Phys. Lett.* **86**, 111117 (2005).

[51] R. Miller, T. E. Northup, K. M. Birnbaum, A. Boca, A. D. Boozer, and H. J. Kimble. Trapped atoms in cavity QED: coupling quantized light and matter. *Journal of Physics B: Atomic, Molecular and Optical Physics* **38**, S551 (2005).

[52] G. Cui, J. M. Hannigan, R. Loeckenhoff, F. M. Matinaga, M. G. Raymer, S. Bhongale, M. Holland, S. Mosor, S. Chatterjee, H. M. Gibbs, and G. Khitrova. A hemispherical, high-solid-angle optical micro-cavity for cavity-QED studies. *Opt. Express* **14**, 2289 (2006).

[53] G. V. Prakash, L. Besombes, T. Kelf, J. J. Baumberg, P. N. Bartlett, and M. E. Abdelsalam. Tunable resonant optical microcavities by self-assembled templating. *Opt. Lett.* **29**, 1500 (2004).

[54] R. J. Warburton, C. Schaflein, D. Haft, F. Bickel, A. Lorke, K. Karrai, J. M. Garcia, W. Schoenfeld, and P. M. Petroff. Optical emission from a charge-tunable quantum ring. *Nature* **405**, 926 (2000).

[55] G. Wang, S. Fafard, D. Leonard, J. E. Bowers, J. L. Merz, and P. M. Petroff. Time-resolved optical characterization of InGaAs/GaAs quantum dots. *Appl. Phys. Lett.* **64**, 2815 (1994).

[56] D. V. O'Connor and D. Phillips. *Time Correlated Single Photon Counting*. Academic Press. 1984.

[57] I. Rech, G. Luo, M. Ghioni, Y. Haw, X. S. Xie, and S. Cova. Photon-timing detector module for single-molecule spectroscopy with 60 ps resolution. *IEEE Journal of Selected Topics in Quantum Electronics* **10**, 788 (2004).

[58] E. Dekel, D. V. Regelman, D. Gershoni, E. Ehrenfreund, W. V. Schoenfeld, and P. M. Petroff. Cascade evolution and radiative recombination of quantum dot multiexcitons studied by time-resolved spectroscopy. *Phys. Rev. B* **62**, 11038 (2000).

[59] G. Bacher, R. Weigand, J. Seufert, V. D. Kulakovskii, N. A. Gippius, A. Forchel, K. Leonardi, and D. Hommel. Biexciton versus exciton lifetime in a single semiconductor quantum dot. *Phys. Rev. Lett.* **83**, 4417 (1999).

[60] R. Hanbury Brown and R. Q. Twiss. A test of a new type of stellar interferometer on Sirius. *Nature* **178**, 1046 (1956).

[61] H. J. Kimble, M. Dagenais, and L. Mandel. Photon antibunching in resonance fluorescence. *Phys. Rev. Lett.* **39**, 691 (1977).

[62] O. Madelung, editor. *Semiconductors – Basic data*. Springer, second edition. 1996.

[63] D. C. Unitt. *Enhanced single photon emission from a quantum dot in a semiconductor microcavity*. PhD thesis, University of Cambridge. 2005.

[64] B. Alén, F. Bickel, K. Karrai, R. J. Warburton, and P. M. Petroff. Stark-shift modulation absorption spectroscopy of single quantum dots. *Appl. Phys. Lett.* **83**, 2235 (2003).

[65] B. D. Gerardot, S. Seidl, P. A. Dalgarno, R. J. Warburton, M. Kroner, K. Karrai, A. Badolato, and P. M. Petroff. Contrast in transmission spectroscopy of a single quantum dot. *Appl. Phys. Lett.* **90**, 221106 (2007).

[66] H. Drexler, D. Leonard, W. Hansen, J. P. Kotthaus, and P. M. Petroff. Spectroscopy of quantum levels in charge-tunable InGaAs quantum dots. *Phys. Rev. Lett.* **73**, 2252 (1994).

[67] H. A. Macleod. *Thin Film Optical Filters*. CRC Press, third edition. 2001.

[68] R. H. Hadfield, P. A. Dalgarno, J. A. O'Connor, E. Ramsay, R. J. Warburton, E. J. Gansen, B. Baek, M. J. Stevens, R. P. Mirin, and S. W. Nam. Submicrometer photoresponse mapping of nanowire superconducting single-photon detectors. *Appl. Phys. Lett.* **91**, 241108 (2007).

[69] K. M. Nowak, H. J. Baker, and D. R. Hall. Efficient laser polishing of silica micro-optic components. *Appl. Optics* **45**, 162 (2006).

[70] G. A. J. Markillie, H. J. Baker, F. J. Villarreal, and D. R. Hall. Effect of vaporization and melt ejection on laser machining of silica glass micro-optical components. *Appl. Optics* **41**, 5660 (2002).

[71] P. Klocek, editor. *Handbook of infrared optical materials.* CRC Press. 1991.

[72] Y. Zhu, D. J. Gauthier, S. E. Morin, Q. Wu, H. J. Carmichael, and T. W. Mossberg. Vacuum Rabi splitting as a feature of linear-dispersion theory: Analysis and experimental observations. *Phys. Rev. Lett.* **64**, 2499 (1990).

[73] J. McKeever, J. R. Buck, A. D. Boozer, and H. J. Kimble. Determination of the number of atoms trapped in an optical cavity. *Phys. Rev. Lett.* **93**, 143601 (2004).

[74] P. Maunz, T. Puppe, I. Schuster, N. Syassen, P. W. H. Pinkse, and G. Rempe. Normal-mode spectroscopy of a single-bound-atom–cavity system. *Phys. Rev. Lett.* **94**, 033002 (2005).

[75] T. D. Happ, I. I. Tartakovskii, V. D. Kulakovskii, J.-P. Reithmaier, M. Kamp, and A. Forchel. Enhanced light emission of $In_xGa_{1-x}As$ quantum dots in a two-dimensional photonic-crystal defect microcavity. *Phys. Rev. B* **66**, 041303 (2002).

[76] H. Gotoh, H. Kamada, H. Nakano, T. Saitoh, H. Ando, and J. Temmyo. Optical nonlinearity induced by exciton-biexciton coherent effects in InGaAs quantum dots. *Appl. Phys. Lett.* **87**, 102101 (2005).

[77] M. Bayer, T. L. Reinecke, F. Weidner, A. Larionov, A. McDonald, and A. Forchel. Inhibition and enhancement of the spontaneous emission of quantum dots in structured microresonators. *Phys. Rev. Lett.* **86**, 3168 (2001).

[78] T. Steinmetz, Y. Colombe, D. Hunger, T. W. Hansch, A. Balocchi, R. J. Warburton, and J. Reichel. Stable fiber-based Fabry-Pérot cavity. *Appl. Phys. Lett.* **89**, 111110 (2006).

[79] V. Savona. Strong coupling of exciton-polaritons in semiconductor microcavities. *Journal of Crystal Growth* **185**, 737 (1998).

[80] V. Savona. Unified treatment of weak and strong coupling regimes. *Solid State Comm* **93**, 733 (1995).

[81] M. Skolnick, T. A. Fisher, and D. M. Whittaker. Strong coupling phenomena in quantum microcavity structures. *Semicond. Sci. Technol.* **13**, 645 (1998).

[82] U. Fano. Effects of configuration interaction on intensities and phase shifts. *Phys. Rev.* **124**, 1866 (1961).

[83] M. Kroner, A. O. Govorov, S. Remi, B. Biedermann, S. Seidl, A. Badolato, P. M. Petroff, W. Zhang, R. Barbour, B. D. Gerardot, R. J. Warburton, and K. Karrai. The nonlinear Fano effect. *Nature* **451**, 1022 (2008).

[84] J. Kondo. Resistance minimum in dilute magnetic alloys. *Progress of Theoretical Physics* **32**, 37 (1964).

[85] B. D. Gerardot, D. Brunner, P. A. Dalgarno, P. Öhberg, S. Seidl, M. Kroner, K. Karrai, N. G. Stoltz, P. M. Petroff, and R. J. Warburton. Optical pumping of a single hole spin in a quantum dot. *Nature* **451**, 441 (2008).

[86] R. Loudon. *The Quantum Theory of Light*. Oxford University Press, third edition. 2000.

[87] M. Kroner, S. Rémi, A. Högele, S. Seidl, A. W. Holleitner, R. J. Warburton, B. D. Gerardot, P. M. Petroff, and K. Karrai. Resonant saturation laser spectroscopy of a single self-assembled quantum dot. *Physica E Low-Dimensional Systems and Nanostructures* **40**, 1994 (2008).

[88] H.-P. Komsa, E. Arola, J. Pakarinen, C. S. Peng, and T. T. Rantala. Beryllium doping of GaAs and GaAsN studied from first principles. *Phys. Rev. B* **79**, 115208 (2009).

[89] D. L. Miller and P. M. Asbeck. Be redistribution during growth of GaAs and AlGaAs by molecular beam epitaxy. *J. Appl. Phys.* **57**, 1816 (1985).

[90] P. Enquist, G. W. Wicks, and L. F. Eastman. Anomalous redistribution of beryllium in GaAs grown by molecular beam epitaxy. *J. Appl. Phys.* **58**, 4130 (1985).

[91] B. T. Cunningham, L. J. Guido, J. E. Baker, J. J. S. Major, J. N. Holonyak, and G. E. Stillman. Carbon diffusion in undoped, n-type, and p-type GaAs. *Appl. Phys. Lett.* **55**, 687 (1989).

[92] R. Paschotta. *Encyclopedia of Laser Physics and Technology*. Wiley–VCH. 2008.